Utrecht University

The Petrology and Inorganic Geochemistry of Glendonites:

Insights into the enigmatic ikaite-to-glendonite transformation using a detailed combinative approach

Master's thesis

by Matthijs Bloem
Student number: 5771749
Email address: M.Bloem@students.uu.nl

Under supervision of dr. Chloé Morales, dr. Bas van de Schootbrugge, and dr. Martin Schobben.

Marine Palynology and Paleoceanography,
Department of Earth Sciences, Faculty of Geosciences, Utrecht University,
Princetonlaan 8a, 3584 CB Utrecht, Netherlands

Table of Contents

Abstract

The presence of glendonites, calcite pseudomorphs after marine sedimentary ikaite ($CaCO_3 \cdot 6H_2O$), has been used as evidence for cold-water depositional settings or methane seepage. These predictions are based upon increasing stability at lower temperatures and elevated alkalinity, pH, $[PO_4^{3-}]$ typically associated with the precipitation of ikaite. As much uncertainty still accompanies the ikaite-to-glendonite transformation and existing models do not readily explain all observations, this study set out to determine whether a distinct link between internal structure and bulk isotopic composition could be established in glendonites from adjoining locations on Spitsbergen formed during coeval time periods. This study reports that none of the 5 identified groups (some with subgroups) exhibited a clear relationship with their respective bulk carbon and oxygen isotopic compositions. Instead, these groups correlate best with their respective sedimentological environment or period of formation. Undiagnostic $\delta^{13}C_{carb}$ values that apparently remained mostly unaltered indicate that ikaite or glendonites were most likely formed using a mixture of carbon sources. It is therefore concluded that glendonites with more negative $\delta^{13}C_{carb}$ values and $\delta^{18}O_{carb}$ values closest to ambient seawater are not necessarily best-preserved. Instead, the combination of carbon sources, the timing of mineral formation, and preservation can yield well-preserved glendonites with different bulk isotopic compositions. The large degree of variety or similarity in the expression of certain paragenetic phases underlines the importance of separating the conditions that govern ikaite formation from its subsequent transformation into glendonites as well as the necessity of phase-specific sampling for successful utilization of glendonites as paleoenvironmental proxies.

1. Introduction

Glendonites, named after the specimens found in the Permian deposits of Glendon in New South Wales (Dana, 1849; David, 1905), are calcite pseudomorphs after the marine form of ikaite (i.e., type 3), a rare and metastable form of calcium carbonate ($CaCO_3 \cdot 6H_2O$). The origin of glendonites has long been enigmatic after its first description in 1827 by the German mineralogist Johann Carl Freiesleben (1774-1846) primarily because its precursor ikaite, named after the type location Ikka Fjord in southern Greenland, was only discovered and identified as a mineral by Pauly (1963) until much later (Huggett et al., 2005). Consequently, glendonites that were found within the geological record have been identified under many different names, including *thinolite* (King, 1878; Shearman et al., 1989), *gennoishi* (Hiki, 1915; Ito, 2004),*White-Sea hornlets* (Kaplan, 1979; Geptner et al., 2014)*, Gersternkörner* (Geptner et al., 2014), *fundylite* (Steacy and Grant, 1974; Brookes et al., 1982), *jarrowite* (Browell, 1860; Shearman and Smith, 1985), *cementsen* (Pedersen and Buchardt, 1996), *pseudogaylussite* (Freiesleben, 1827; van Calker, 1897; Trechmann, 1901), *hedgehogs* and *polar euhedrons* (Kemper and Schmitz, 1975).

The precursor ikaite becomes increasingly stable when temperature decreases and pressure rises (Figure 1.1), in contras to other $CaCO_3$ polymorphs (Marland, 1975; Bischoff et al., 1993a; De Lurio and Frakes, 1999), and at atmospheric conditions ikaite usually breaks down above a threshold of 8°C (Shearman and Smith, 1985; Bischoff et al., 1993a; Boch et al., 2015). Based up these thermodynamic characteristics, the occurrence of ikaite and glendonites within the sedimentary record has repeatedly been used as evidence for cold-water and even near-freezing conditions in the past (James et al., 2005; Selleck et al., 2007; Spielhagen and Tripati, 2009; Price and Nunn, 2010; Herrle et al., 2015; Grasby et al., 2017). Although glendonites are commonly found within the presence of boulders and conglomerates that are interpreted as dropstones and tillite deposits (Price, 1999; James et al., 2005; Selleck et al., 2007; Lu et al., 2012), their link with short episodes of glaciation remains questionable. This is related to fact that glendonites are also found within deposits from greenhouse periods such as the Lower Cretaceous and Paleocene-Eocene (Kemper, 1987; De Lurio and Frakes, 1999; Price, 1999; Spielhagen and Tripati, 2009) as well as in deposits that were deposited at lower paleolatitudes during the Early Jurassic (Teichert and Luppold, 2013).
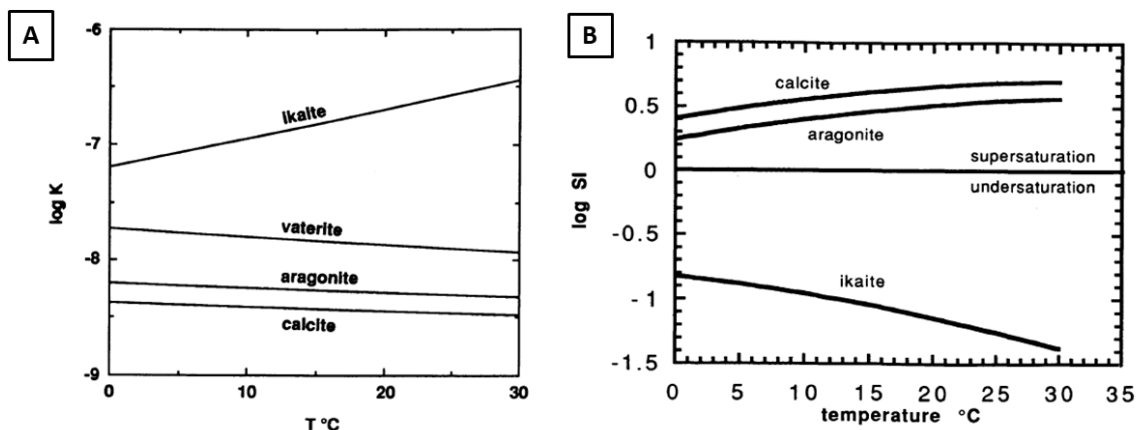
Figure 1.1 *- Diagrams adapted from Bischoff et al. (1993a) indicating the stability of ikaite compared to vaterite, aragonite, and calcite as a function of temperature.* ***(A)*** *Plot of solubility constants (K) showing the increased stability of ikaite at lower temperatures contrary to the trends shown by other CaCO$_3$ polymorphs.* ***(B)*** *Saturation state as a function of the temperature for seawater, where the saturation index (SI) is the ion activity product (IAP) for each mineral divided by its solubility constants (K).*

Apart from temperature and pressure, many studies have shown that other geochemical conditions such as high alkalinity, elevated $[PO_4^{3-}]$ (inhibition of calcite and aragonite growth), organic matter (OM) degradation, and anaerobic oxidation of methane regulate the precipitation of ikaite (Bischoff et al., 1993a; Greinert and Derkachev, 2004; Zhou et al., 2015; Qu et al., 2017). Recent laboratory experiments by Hu et al. (2014b) and Hu et al. (2015) found that salinity and pH may also be important factors for creating an environment in which ikaite is metastable. While it might be tempting to think that the factors which govern ikaite precipitation are also responsible for its transformation to glendonite, this does not necessarily have to be the case as cold water, organic-rich settings have been shown not to automatically trigger ikaite precipitation and glendonite formation (Peckmann, 2017; Morales et al., 2017b). Based upon this observation, the uncertainty in the relative importance of the parameters mentioned above, and the lack of a uniform mechanistic model for their formation impedes the usefulness of glendonites as paleoenvironmental proxies.

Authigenic carbonates such as ikaite formed during deposition at the sediment-water interface, within sediment porewaters soon after deposition, or within their parent rock have proven to be meaningful tools for investigating the global carbon cycle, the distribution of oceanic methane seepage, climate change, and the oxidation state of the planet (Peckmann et al., 1999; Schrag et al., 2013; Sun and Turchyn, 2014; Morales et al., 2017a). The study of these phenomena is based upon differences in isotopic composition of these carbonates compared to that of organic carbon, where a large kinetic isotope fractionation is associated with organic matter production (Hayes et a. 1999). For ikaite/glendonites this means that the $\delta^{13}C_{carb}$ value reflects the state of the porewater carbon pool from which it grew (Lu et al., 2012; Teichert and Luppold, 2013) and the $\delta^{18}O_{carb}$ composition can be used to approximate the isotopic composition of ancient ambient seawater when recrystallization is absent (Price and Nunn, 2010; Qu et al., 2017). Therefore, investigating how isotopic composition relates to the internal structures might shed some light on the formation and usefulness of glendonite as paleoclimatic proxies.

This study sets out to: (1) investigate whether a relationship between internal structure and bulk isotopic composition can be established, (2) if the existing models for ikaite-to-glendonite transformation can explain these differences, and (3) to test the hypothesis that glendonites with increasingly negative $\delta^{13}C_{carb}$ values together with $\delta^{18}O_{carb}$ values closest to that of ambient seawater are best preserved. The abundance of glendonites within several stratigraphic horizons of the Rurikfjellet Formation and Carolinefjellet Formation from Svalbard as well as the occurrence of these horizons at multiple locations provides an ideal scenario to investigate the differences between contemporary samples. This may elucidate how different early diagenetic processes relate to local, regional, or even global geochemical and environmental trends during the Early Cretaceous.

Although it would have been ideal to focus on the replacive calcite, rather than the entire paragenetic sequence, interfingering impeded this phase-specific sampling approach. Additionally, the sampling procedure used to collect powdered subsamples for carbon and oxygen stable isotope analysis, inherited from the earlier stages of this project that contained a different scope, is not optimal for answering the aforementioned research questions and therefore the general utility of the relationships established within this study are reduced. However, some of the conclusions related to underlying drivers for certain compositional differences might still prove to be relevant for future investigations into these enigmatic glendonites.

2. Background information

2.1. Ikaite

Ikaite, the precursor of glendonites, is a carbonate hexahydrate ($CaCO_3.6H_2O$) and one of the polymorphs (i.e., minerals with identical chemical compositions that contain a different crystal structure or atomic arrangement) of $CaCO_3$. Aside from ikaite, these polymorphs also include various amorphous forms, amorphous calcium carbonate (ACC); 2 hydrated forms, calcium carbonate monohydrate (MCC); and 3 anhydrous polymorphs: vaterite, aragonite, and calcite (Hu et al., 2014; Hu et al., 2015). Ikaite has a monoclinic crystal structure in which Ca is bonded more closely to the 6 H_2O molecules than to the CO_3^{2-} ion and shows minor substitution of Mg, Fe, Sr, and Mn (Dickens and Brown, 1970; Hesse et al., 1983; Bischoff et al., 1993a; Huggett et al., 2005; Purgstaller et al., 2017). In nature, ikaite was first observed growing in tufa towers in the Ikka Fjord (Greenland) by Pauly (1963), long after its initial synthesis under controlled conditions (Pelouze, 1865). In later attempts, synthetic ikaite has been precipitated at temperatures as high as 27˚C (Brooks et al., 1950; Huggett et al., 2005). Hereafter, ikaite has been recognized in many other environments while occurring exhibiting different forms (Figure 2.1). Based upon the characteristics of these environments and their specific processes of formation 3 main categories of ikaite have been recognized (Morales et al., 2017b): (1) tufa and travertines (Figure 2.1A-D) that can grow up to tens of meters high which are found in shallow or deep-marine (e.g., Ikka Fjord), lacustrine (e.g., certain lakes in California, Nevada, and Patagonia), or riverine environments that are associated with high alkaline spring waters and potentially a direct microbial control on its formation (Pauly, 1963; Shearman et al., 1989; Bischoff et al., 1991; Bischoff et al., 1993b; Buchardt et al., 1997; Whiticar and Suess, 1998; Omelon et al., 2001; Ito, 2004; Hansen et al., 2011; Oehlerich et al., 2013; Boch et al., 2015; Trampe et al., 2016; Purgstaller et al., 2017); (2) single microscopic crystals (Figure 2.1E), either euhedral or mimicking the shape of brine pockets, that are found within Arctic and Antarctic ice and are associated with low pH, brines highly concentrated in seawater ions due to ice formation, and sympagic autotrophs (Dieckmann et al., 2008; Dieckmann et al., 2010; Rysgaard et al., 2012); and (3) macroscopic single euhedral to stellate crystals clusters (Figure 2.1F-H) found in shallow to deep marine sediments with sizes ranges from 1-20 cm, but in favorable conditions they can reach sizes of up to at least 80 cm (Kaplan, 1979; Morales et al., 2017b). Although ikaite in the form of tufa/travertines (referred to as thinolites or pseudogaylussite after pseudomorphism) and single microscopic crystals are known to form pseudomorphs (Shearman et al., 1989; Bischoff et al., 1991), it is the macroscopic single euhedral to stellate crystals clusters formed within marine environments (i.e., type 3) that transforms into glendonites.

With $\delta^{13}C_{carb}$ ranging from -57 to 3‰ VPDB, the composition of this ikaite type 3 can be remarkably variable, but in most cases, the values are reported to hover around -10 to -25‰ (Lu et al., 2012; Peckmann, 2017; Morales et al., 2017b). Based upon average $\delta^{13}C$ values of carbon sources such as terrestrial organic matter (±30‰), marine organic matter ±20‰), and methane (-30 to -110‰), these typical $\delta^{13}C_{carb}$ values for ikaite prevent the identification of the specific biogeochemical process(es) responsible for its formation (Peckmann, 2017). Correspondingly, it has been suggested that the carbon needed for mineral formation of ikaite type 3 consists of a mixture of seawater, decomposition of OM (Equation 1), and anaerobic oxidation of methane (AOM, Equation 2) (Suess et al., 1982; Stein and Smith, 1986; Schubert et al., 1997; Greinert and Derkachev, 2004; Lu et al., 2012).

$$CH_4 + SO_4^{2-} \rightarrow HS + HCO_3^- + H_2O \qquad\qquad (1)$$
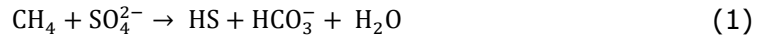
During early diagenesis, biogenic degradation of OM in sediments through sulfate reduction and subsequently both fermentation processes (potentially related to CO_2 reduction) and AOM generate HCO_3^-, which increases alkalinity. These anaerobic processes, combined with the availability of Ca^{2+} from seawater, are thought to responsible for supersaturation with respect to ikaite and thus its precipitation around the sulfate-methane transition (SMT) (Figure 1.1B; Figure 2.2) (Lu et al., 2012; Morales et al., 2017b). The depth of the SMT and the sulfate reduction and AOM zones varies strongly as it may occur at depth in the sediment column or can be located only a few centimers below the sediment-water interface based upon factors such as water depth, sedimentation rate, organic flux/degradation rate, and advective seepage or flux of methane as well as sulfate (Campbell, 2006; Jørgensen and Kasten, 2006; Lu et al., 2012). Additionally, shifts in SMT depth may also occur as the balance or stability of the mentioned factors changes over time.

Crystallization of any mineral involves both nucleation and crystal growth, which are both processes that are regulated by thermodynamics and kinetic factors. Thermodynamics are not only governed by pressure and temperature but also involve the solubility product (K_{sp}) of the carbonate mineral as well as the activities of Ca^{2+} and CO_3^{2-} (i.e., the ion activity product or IAP), which depends on their respective concentrations and activity coefficients (Hu et al., 2014b; Morales et al., 2017b). The values of these specific activity coefficients are determined by temperature and the ionic strength of the solution (Hu et al., 2014b). Together the K_{sp} and IAP determine the solution supersaturation with respect to ikaite (Ω = IAP/K_{sp}) that can subsequently be used as a measurement for the nucleation rate (Boistelle and Astier, 1988; Hu et al., 2014a). Ikaite is generally more soluble than other common $CaCO_3$ polymorphs (e.g., calcite, aragonite, and vaterite) in marine environments/near-surface conditions and therefore alkalinity needs to increase dramatically (e.g., a 10-fold increase for seawater at $0°C$) or other factors are required to prevent the precipitation of the other polymorphs in order for ikaite to gain precedence during the competition for porewater Ca^{2+} and CO_3^{2-} (Figure 1.1) (Bischoff et al., 1993a; Selleck et al., 2007; Hu et al., 2014b; Zhou et al., 2015). As mentioned before, based upon the type of ikaite this increase in alkalinity occurs either due to the presence of springs (type 1), the formation of ice brines (type 2), or the decomposition of OM and AOM (type 3). After the initial nucleation, crystals growth converts the nuclei into macroscopic crystals. This stage of the crystallization process is not only governed by the aforementioned external factors (e.g., temperature and supersaturation), but also by internal factors such as the crystal structure, crystal defects, and the intermolecular interactions of the crystal surfaces with the solution (Boistelle and Astier, 1988; Burton, 1993; Hu et al., 2015).
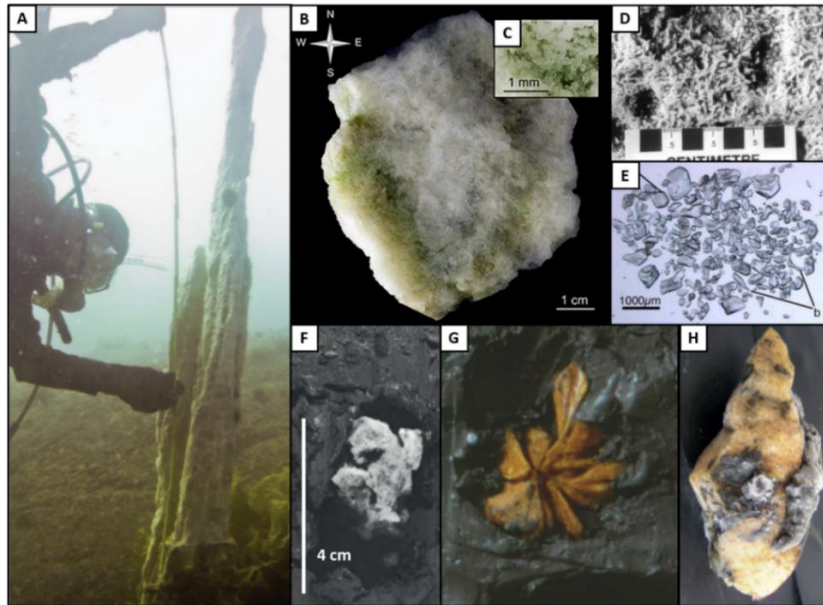
Figure 2.1 - *Pictures of the different expressions of ikaite that have been grouped into 3 categories based primarily upon their distinct environment and specific processes of formation (Morales et al., 2017b), but other independent factors such as morphological differences may provide additional constraints . (A-D) show the tufa and travertines (type 1), (E) the single microscopic crystals (type 2), and (FG) the macroscopic single euhedral to stellate crystals. **(A)** Ikaite tufa column from the Ikka Fjord in Greenland (Hansen et al., 2011); **(B)** Cross-section of an ikaite column also from the Ikka Fjord with dense yellowish green bands of various thicknesses together with **(C)** a close-up of a biofilm produced by cyanobacteria (Trampe et al., 2016); **(D)** Tavertine ikaite from the Axel Heiberg Fjord in Canada (Omelon et al., 2001); **(E)** Euhedral microscopic ikaite crystals from Antarctic sea ice taking on the shape of brine pockets (Dieckmann et al., 2008); **(F)** Aggregate of crystals from the Nankai Through (Stein and Smith, 1986); **(G)** Stellate cluster of crystals from the Congo Fan (Morales et al., 2017b); **(H)** Single crystals from the Disko Bugt area offshore West Greenland (Nielsen et al., 2014).*
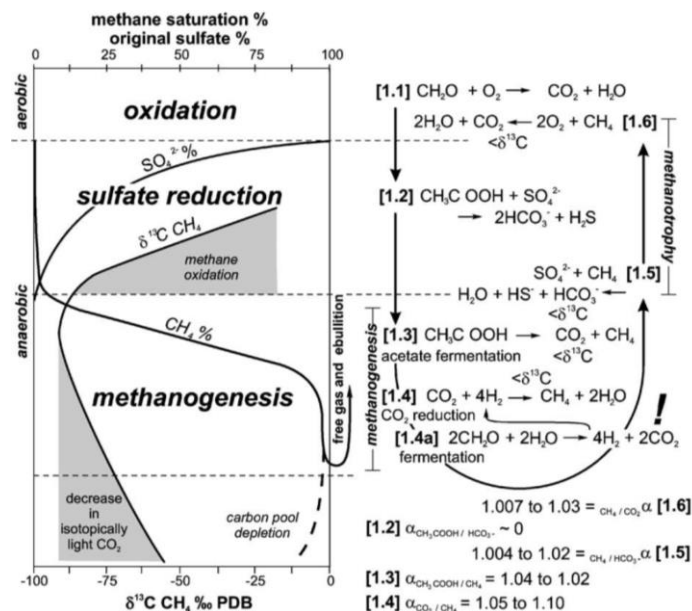
Figure 2.2 – *Schematic diagram of the oxidation, sulfate reduction, and methanogenic zones together with their related methane-carbon isotope signatures. The right side shows important geochemical reactions for organic matter degradation (1.1, 1.2), methane formation (methanogenesis; 1.3 and 1.4, 1.4a), and methane consumption (methanotrophy; 1.5 and 1.6), as well as the types of carbon species that are formed and where enhancement of carbonate precipitation occurs due to release of HCO_3^- (1.2 and 1.5). Figure adapted from Campbell (2006).*

Aside from the factors mentioned above, kinetics also play an essential role in determining the crystallization rate of each specific carbonate polymorph (Morales et al., 2017b). These kinetic factors are affected by the presence of catalysts or inhibitors (e.g., PO_4^{3-}, Mg^{2+}, SO_4^{2-}) that have been shown to either block sites of crystal growth or even absorb carbonates (Greinert and Derkachev, 2004; Lin and Singer, 2005, 2006; Hu et al., 2014b; Morales et al., 2017b). Many studies have suggested that PO_4^{3-} constitutes the primary or mandatory inhibitor for the formation of ikaite as it has a stronger impeding effect on calcite/aragonite by decreasing the rate of dehydration in the solvation shell (i.e., the interface of interaction between a chemical compound and the respective solvent) of Ca^{2+}, making the formation of hydrated polymorphs more favorable (Hu et al., 2014b; Hu et al., 2015; Zhou et al., 2015; Purgstaller et al., 2017). This effect is increasingly pronounced at lower temperatures, but can be counteracted by the presence of dissolved SO_4^{2-} as it can reduce the inhibitory effect of PO_4^{3-} (Burton, 1993; Greinert and Derkachev, 2004; Hu et al., 2014b; Purgstaller et al., 2017). While the notion that PO_4^{3-} is crucial for the preferential growth of ikaite seems to be true for most environments, there are also studies that have reported that in environments which are saturated or have very low temperatures, PO_4^{3-} is not always mandatory (Omelon et al., 2001; Dieckmann et al., 2010; Hu et al., 2014a; Hu et al., 2015; Morales et al., 2017b). Although this appears to be contradictory, it does fits with the recent observation that PO_4^{3-} coprecipitates of during the initial stages of ikaite growth (Hu et al., 2014a).

Some natural occurrences of ikaite (e.g., type 2 and brines that are the result of sea ice formation) are associated with saline environments (Bischoff et al., 1991; Omelon et al., 2001; Oehlerich et al., 2013), but the relationship between the precipitation of ikaite and salinity is not clear-cut as it can have opposite effects (Hu et al., 2014b; Morales et al., 2017b). The positive effect of increased salinity involves an increase in the CO_3^{2-} fraction and thus pH (affects $CaCO_3$ and phosphate speciation), but it also negatively affects ikaite precipitation by reducing the activities of Ca^{2+} and CO_3^{2-}, which favors the precipitation of anhydrous $CaCO_3$ polymorphs rather than ikaite (Burton and Walter, 1990; Bischoff et al., 1993a; Hu et al., 2014b; Morales et al., 2017b).

Based upon these principles, a monitoring program studied the precipitation of ikaite type 1 in a partially man-made environmental setting (i.e., construction and concrete lining of a river bed), which yielded growth rates of up to 2 kg d^{-1} m^{-2} without the presence of nucleation inhibitors, strongly elevated ionic strength (i.e., brines), or water-mixing (Boch et al., 2015). Additionally, Boch et al. (2015) also noticed that some of the crystal aggregates already disintegrated into calcite powder at ambient temperature within only a few days. Growth rates for ikaite type 1 (within tufa columns) in natural environments tend to be lower with estimations of 4-5 cm vertical height per month or 50-60 cm per year (Buchardt et al., 2001; Hansen et al., 2011). Although it is very likely that each type of ikaite grows at different rates and that these estimated therefore cannot be translated to type 3, these findings still support the idea that within the right conditions, ikaite can both grow and potentially even transform rapidly.

Microbiological studies of ikaite columns (i.e., type 1) have shown that organisms such as certain bacteria and coralline algae (e.g., *Clathromorphum* spp., *Lithothamnion* spp., *Chroomonas ikaitensis*) form pigmented patched inside the columns and stabilize their otherwise fragile structures (Hansen et al., 2011; Trampe et al., 2016). As these types of patches have not been readily identified in the other ikaite categories, it is still unclear whether this kind of stabilization and symbiotic growth is only required for larger ikaite

structures. However, as one of the main characteristics of the first paragenetic phase of glendonites includes black impurities, of which some are strongly luminescent under UV light (indication of OM preservation), it cannot be ruled out that the formation of chemical zonations and microhabitats in the ikaite matrix may also support or control the growth of the other ikaite categories such as type 3 (Trampe et al., 2016; Morales et al., 2017b). Also, the presence lipid biomarkers associated with sulfate-reducing bacteria recently found within glendonites (Qu et al., 2017), together with their known ability to promote mineral precipitation (Han et al., 2016) seems to point in a similar direction. Despite these connections, certain laboratory experiments have clearly indicated that it is also possible to form inorganic ikaite at elevated temperatures of up to at least 12˚C when ikaite is sufficiently supersaturated (Purgstaller et al., 2017) and some authors even stress that a distinct association between ikaite/glendonites and particular biota is lacking (De Lurio and Frakes, 1999; Teichert and Luppold, 2013; Morales et al., 2017b).

2.2. Pseudomorphism (ikaite-to-glendonite transformation)

To constrain the formation of ikaite (and its subsequent transformation to glendonites), several studies have used either porewater [Ca^{2+}], [DIC], alkalinity, and $\delta^{13}C_{carb}$ of ikaite (Suess et al., 1982; Lu et al., 2012; Zhou et al., 2015), or lipid biomarkers combined with the isotopic composition of carbonate-associated sulfate ($\delta^{34}S_{CAS}$) and chromium-reducible sulfate ($\delta^{34}S_{CRS}$) (Qu et al., 2017) to estimate the depth and location of ikaite type 3 formation zones below the sediment-water interface and around the SMT. While these parameters appear to be well constrained, the actual timing and how the ikaite-to-glendonite transformation takes place remains enigmatic. Nonetheless, there are some sedimentological and geochemical observations which indicate that the ikaite-to-glendonite transformation occurs during early diagenesis and before any considerable sediment compaction. One of these observations is the displacement/draping of sediment surrounding ikaite and glendonites and fluid depletion features (Morales et al., 2017a; Morales et al., 2017b). In some samples, dissolution of carbonate phases associated with fluid depletion features also result in collapse or partial destruction of the sample (Morales et al., 2017a). Other observations include: the presence of reworked/broken glendonites within intraformational conglomerate beds (Kaplan, 1978; Morales et al., 2017a), the fact that glendonites are frequently found to be surrounded by concretions (Huggett et al., 2005; Selleck et al., 2007; Teichert and Luppold, 2013; Qu et al., 2017; Vickers et al., 2018), or occurrence of intermediate samples, referred to as *transformed ikaite*, that show a joint presence of hydrated and diagenetic anhydrous carbonate phases (Selleck et al., 2007; Morales et al., 2017b). When hydrated (e.g., monohydrocalcite) and anhydrous carbonate phase occur in this fashion, the anhydrous phases are the ones that resemble the first 2 paragenetic phases found within glendonites (i.e., rosettes and botryoids) (Stein and Smith, 1986; Morales et al., 2017b). The lack of alternative intermediate phases (e.g., aragonite and the rare mineral vaterite), that have been recognized in laboratory studies (Selleck et al., 2007; Hu et al., 2014b; Purgstaller et al., 2017), in natural specimens may be related to differences in geochemical conditions or a discrepancy in relevant time scales of observation.

The documentation of short-chain hydrocarbons, trapped as gas inclusions within glendonites, by Morales et al. (2017a) using compound-specific isotope analyses provided additional insights into the rate of ikaite-to-glendonite transformation. The composition of these gases (i.e., especially the presence of propane, a thermogenic hydrocarbon gas, that typically rapidly degrades) and the low fractionation of their $\delta^{13}C_{gas}$ values suggests that pseudomorphosis occurs rapid, potentially even at a seasonal time scale, and that AOM might be vital for the preservation of ikaite (Peckmann, 2017; Morales et al., 2017b). Unfortunately, due to the small size and interfingering of the carbonate phases, it was impossible to perform this compound-specific isotope analysis on solely the *first phase*. As a result, this could mean that the presence of short-chain hydrocarbons does not reflect the environment during the initial ikaite-to-glendonite transformation, but rather is indicative of the conditions that occurred during precipitation of later paragenetic phases. While these short-chain hydrocarbons seems to provide reliable information about the local environment, data interpretation appears to require great care as a recent study looking at similarities between seep carbonate entrapped-gas fractions and seep gas geochemistry of their source found that valuable information on the composition and $\delta^{13}C_{gas}$ of ethane and propane were either modified or lost (Blumenberg et al., 2017).

2.3. Proposed mechanistic models for glendonite formation

2.3.1. Methane-dominated cold vent model

Greinert and Derkachev (2004) were the first who attempted to create a systematic model (Figure 2.3) for the formation of glendonites in an area of active methane venting on the slope of the Sakhalin Peninsula, located in the Sea of Okhotsk. In their model, advection of methane towards shallower sediment depths enhances the anaerobic decomposition of OM through sulfate reduction (above the SO_4/H_2S boundary), resulting in an increased release of HCO_3^- and PO_4^{3-} from OM (Greinert and Derkachev, 2004). When the upward-migrating fluids succeed in pushing the zone of anaerobic OM decomposition towards the sediment-water interface, ikaite can form (stage 1) as calcite, Mg-calcite, and aragonite are inhibited by SO_4^{2-} and PO_4^{3-} (Greinert and Derkachev, 2004). The continued migration of fluids will result in leakage of SO_4^{2-}, which conjointly reduces the amount of OM decomposition and thus $[PO_4^{3-}]$ (Greinert and Derkachev, 2004). If the $[PO_4^{3-}]$ and alkalinity (as a result of crystallization of ikaite and other carbonate phases) become too low ikaite will break-down and transform (stage 2) (Greinert and Derkachev, 2004). On-going transport of H_2S and CH_4 from deeper sediment horizons and in-situ formation of H_2S during AOM result in the formation of pyrite within the pore space (stage 3) at the SO_4^{2-}/H_2S boundary (Greinert and Derkachev, 2004). During the final stage (stage 4), AOM provides a secondary increase in alkalinity that enables the precipitation of Mg-calcite in the sediment and porous fabric of the glendonites (Greinert and Derkachev, 2004).
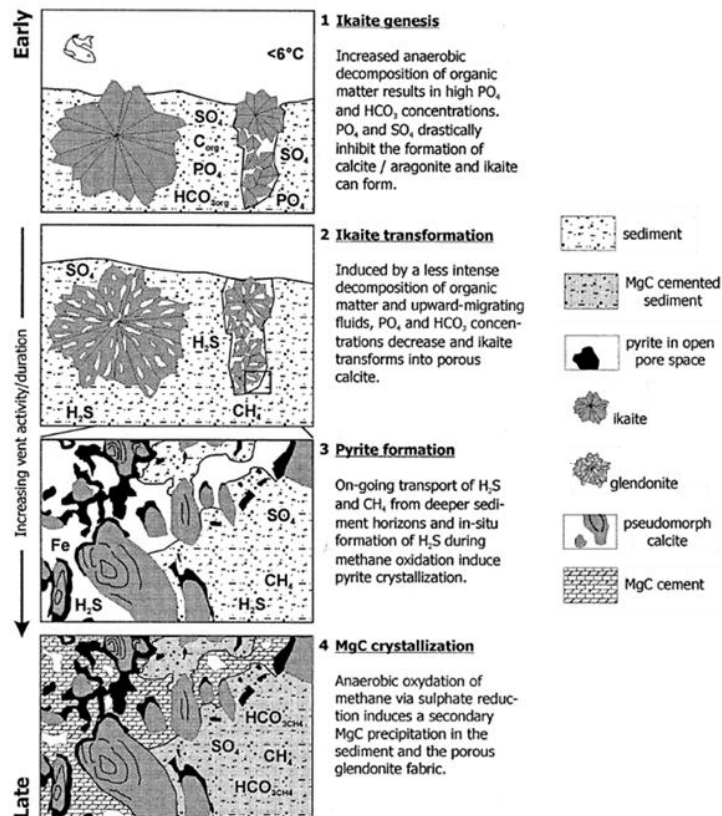
Figure 2.3 – *Scheme of ikaite to glendonite transformation within a methane vent-induced environment as proposed by Greinert and Derkachev (2004) with secondary methane-derived Mg-calcite crystallization as suggested by glendonite and amber-colored calcite concretions found at a cold vent area at the Sakhalin slope.*

2.3.2. Allochthonous hydrocarbon gas model

A more recent model that shows similarities with that of Greinert and Derkachev (2004) is the general scheme for glendonite formation (Figure 2.4) proposed by Morales et al. (2017b). These authors propose that the location of ikaite precipitation within the sedimentary column is controlled by the migration pathway of allochthonous hydrocarbon gases towards the sediment-water interface and Ca^{2+} availability at relatively cold temperatures and high pressures within saline environments. This hypothesis is primarily based upon similarities in the occurrence of ikaite type 3/Quaternary glendonites and the distribution of areas with vents/seepage or areas in the vicinity of locations known to contain methane hydrates/gas fields. Additionally, their previous discovery of short-chain hydrocarbons in widely distributed glendonites from the Early Jurassic to Early Cretaceous strata of Siberia (Russia) as well as similarities between the general isotopic trends/carbonate mineral phases of glendonites and seep limestones also form an important argument (Morales et al., 2017a; Morales et al., 2017b). In their model, ikaite formed beneath the sediment-water interface transforms around the SMT in areas that contain upward migrating hydrocarbons (stage 1). During this stage, both the first (rosettes) and the second phase (botryoidal carbonate) precipitate. Precipitation of later carbonate phases and/or either total or partial recrystallization of previous phases (a) or infilling of pore space by yellow clotted to anhedral calcite (b) (stage 2) will occur somewhere during continued burial (Morales et al., 2017b).
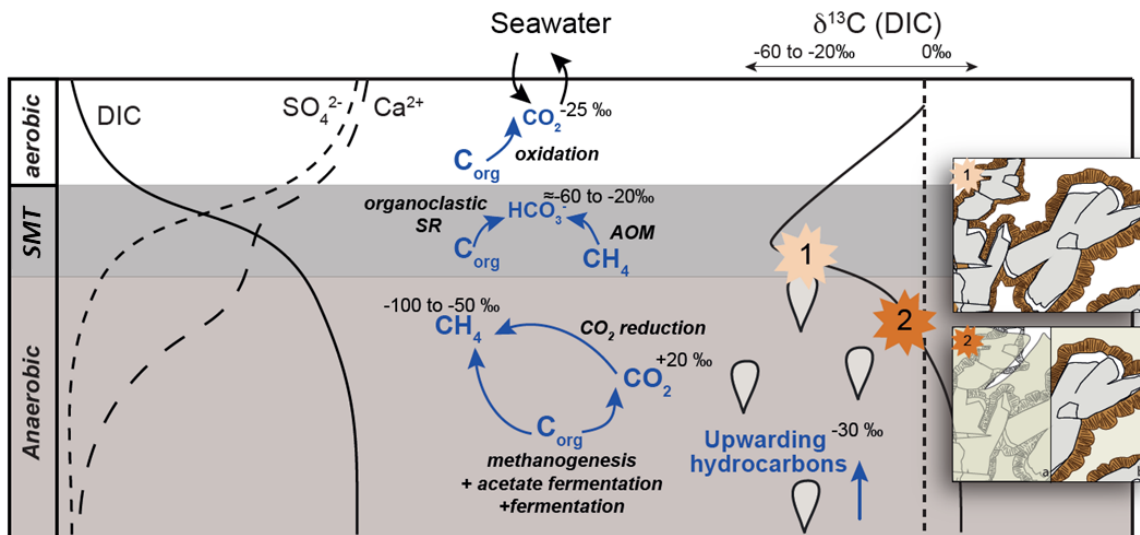
Figure 2.4 - *General scheme of glendonite formation as proposed by Morales et al. (2017b) with a simplified geochemical profile for uppermost marine sediments and early diagenetic processes affecting autochthonous and allochthonous organic material. (1) Transformation of ikaite to glendonite within the sulphate-methane transition (SMT) with the formation of rosettes and botryoidal carbonate phases. (2) Precipitation of later carbonate phases with total or partial recrystallization of previous precipitates (a) or infilling of void spaces by yellow clotted to anhedral calcite (b).*

2.3.3. Margin-to-center transformation model

Teichert and Luppold (2013) describe a different model, that does not rely on the presence of either hydrocarbons or methane, for the formation of glendonites. Their model, which is based upon specimen from methane seep deposits from a Late Pliensbachian section, suggests that during the ikaite-to-glendonite transformation destabilization occurs preferentially at the margins, while the center of the ikaite crystal initially remains stable (Teichert and Luppold, 2013). After margin is transformed, the center will also break-down and thereby form a new generation of rim cement. It is important to note that this differentiation between margin and center introduces a noncontemporary relationship between the similar carbonate phases. While this makes interpreting the paragenetic sequence rather complex and potentially results in problems concerning the order of formation of different carbonate phases, Teichert and Luppold (2013) rightfully point out that does provide an elegant explanation for the mechanism responsible for the pseudomorphosis. Furthermore, Teichert and Luppold (2013) believe that varying porewater conditions during the destabilization of ikaite are not only responsible for the variable composition, but also the number of rim cements. Similar to the other models, the final stages involve the infilling of the remaining open pore space by carbonate cement by either trapped or diffusing fluids that could potentially seal off the margins, leaving the center free of these cements (Teichert and Luppold, 2013).

2.3.4. Unzoned vs. zoned glendonite model

The latest and most comprehensive model for glendonite formation was proposed by Vickers et al. (2018) who build upon the ideas from Frank et al. (2008) and aspects of the methane-dominated cold vent model (Teichert and Luppold, 2013) to explain the prominent petrological differences between glendonites from the Rurikfjellet and Carolinefjellet Formation from Spitsbergen. Aside from the 3 prevalent and widely recognized carbonate phases, these glendonites also exhibited etched boundaries on the secondary carbonate phase (i.e., Type II), distinctive cores and rims, and macro-zoning (Vickers et al., 2018). As some of these features were not readily explained using the parameters from the existing models Vickers et al. (2018) proposed separate scenarios for the unzoned glendonites (Figure 2.5A) and macro-zoned glendonites (Figure 2.5B) and concluded that differences in sedimentation rate were the conclusive factor (Vickers et al., 2018).
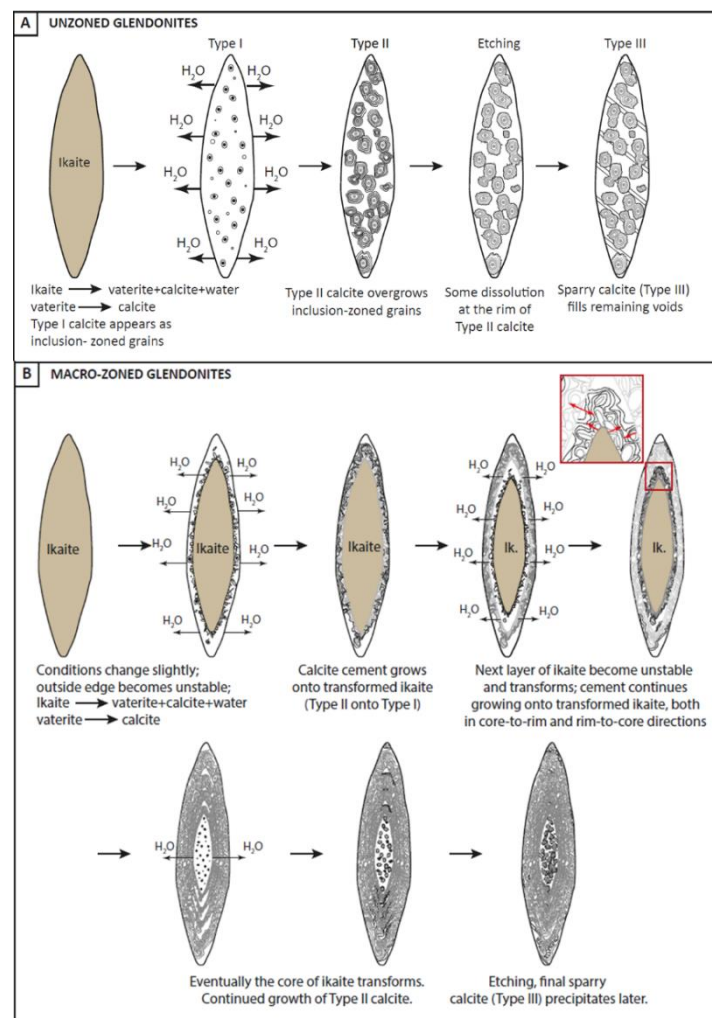

Figure 2.5 – *Models for ikaite-to-glendonite transformation as proposed by Vickers et al. (2018) based upon the ideas from Frank et al. (2008) and Teichert and Luppold (2013). (A) Model for ikaite-to-glendonite transformation for unzoned glendonites, where ikaite breaks down into a mix of vaterite, calcite, and water, and the vaterite rapidly transforms to calcite within the sulphate reduction zone. This ikaite-calcite experiences rapid diagenetic calcite overgrowth that ceases as it and its host sediment move out of the sulphate reduction zone. Subsequently, as conditions become unfavorable for calcite precipitation partial dissolution may occur at the edges of the diagenetic calcite and an unkown amount of time later, late-stage sparry calcite infills any remaining voids. (B) Model for ikaite-to-glendonite transformation of macro-zoned glendonites, whereby oscillation in conditions result in slow and progressive break-down of the ikaite crystal, from the outside in.*

Within their model for unzoned glendonites (Figure 2.5A), Vickers et al. (2018) envision that entire ikaite crystal breaks down into a mix of vaterite, calcite, and water. During this stage, inclusion-zoned grains that consist of calcite and represent the first phase (Type I) are formed directly from ikaite and through the subsequent transformation of the intermediate vaterite (Vickers et al., 2018). Following this transformation, rapid diagenetic calcite growth in the sulfate reduction zone is believed to be responsible for the formation of the second phase (Vickers et al., 2018). When the glendonites become increasingly buried and move out of the sulfate reduction zone this growth ceases and dissolution/etching may occur at the rims of the second phase (Vickers et al., 2018). Finally, during later unspecified diagenetic stages, the remaining pore space is filled with sparry calcite cement (Vickers et al., 2018)

For the glendonites that exhibit macro-zoning, Vickers et al. (2018) propose a model (Figure 2.5B) in which slower sedimentation rates result in oscillations of physiochemical conditions around the ikaite stability field, resulting progressive destabilization of the ikaite crystal from the outside in. Glendonites with distinctive cores and rims are believed to form via a similar process, albeit with a sedimentation rate closer to that of the unzoned glendonite (Vickers et al., 2018). Although progressive growth could also have occurred from the inside out, Vickers et al. (2018) argue that this seems very unlikely as it would prevent the distinct zoning from being preserved. Other arguments that support this notion include: a lack of blebs of original ikaite crystals within the center, similar structural elements in the center and rims, and the apparent observation of larger *first phase* crystal within the center (Teichert and Luppold, 2013; Vickers et al., 2018).

3. Methodology

3.1. Geological setting and study area

The studied sections of Festningen and Grumantbyen are located on Spitsbergen (Figure 3.1A), the largest island of the Svalbard archipelago. The Svalbard archipelago is situated between latitudes 74-81°N and longitudes 10-35°E on the northwestern corner of the Barents Shelf that subsequently forms the northwestern edge the Eurasian plate (Figure 3.2). While the Svalbard archipelago covers only about 5% of the surface area of the entire Barents Shelf (approximately 1.3 million km^2), it represents a comprehensive and subaerially exposed overview of the geology for the entire region as its contains deposits from the Archean all to way to the Quaternary (Harland et al., 1997; Elvevold, 2007; Worsley, 2008; Smerlor, 2009; Koevoets et al., 2018).
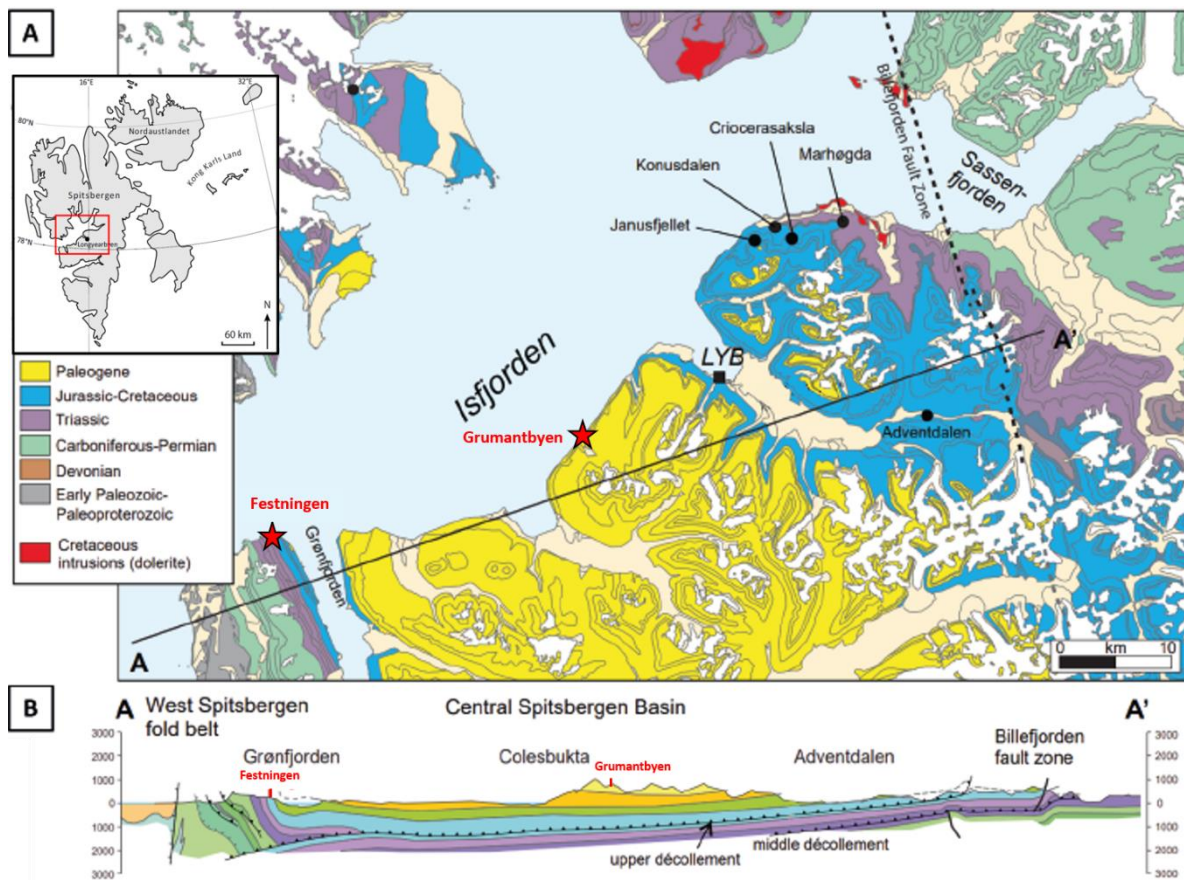

Figure 3.1 *- Geological overview of the study area. **(A)** Small inset map of Spitsbergen together with a geological map illustrating the location of both the Festningen and Grumantbyen successions. **(B)** Regional cross-section across the Central Spitsbergen Basin along the profile indicated in A. Note that the blue Jurassic-Cretaceous sediments in Grumantbyen are located close to sea level around the marked position and further north near Bjørndalen (situated south of Adventdalen). Map based upon Dallmann (2001) and modified after Koevoets et al. (2018).*

The Barents Shelf has an average depth of around 200-300 m and forms one of the largest continental shelves on Earth. On its western side, the Barents Shelf is bounded by a sheared margin and the Norwegian-Greenland Sea, to the north by a now passive rifted continental margin and the polar Euramerican basin, to the east by Novaya Zemlya (which separates it from the adjacent Kara Shelf), and to the south by the Baltic Shield (Worsley, 2008; Smerlor, 2009; Grundvåg et al., 2017). Based upon the large-scale structure shown

in the E-W orientated regional profile (Figure 3.2) it is possible to roughly divide the present-day Barents Shelf into two major geological provinces that are separated by a generally monoclinal structure with a north-south trend (Worsley, 2008; Smerlor, 2009). The western province constitutes a tessellation of structural highs, platforms, and rift basins that predominantly reflect the post-Caledonian rifting phases as well as the later continental break-up that occurred along the northwestern margin of the Eurasian plate and the effects of the Eurekan Orogeny (Doré et al., 1999; Worsley, 2008; Smerlor, 2009; Grundvåg et al., 2017). In contrast, the development of the eastern province, which contains the most profound sedimentary basins (i.e., the North and South Barents basins) of the Barents Shelf, had a much closer relationship with the tectonic history of Novaya Zemlya, the Timan-Pechora Basin, and the Uralian Orogeny (Worsley, 2008; Smerlor, 2009). As a result, the tectonic history, basement development and sedimentological regimes of both provinces show similarities as well as remarkable differences.
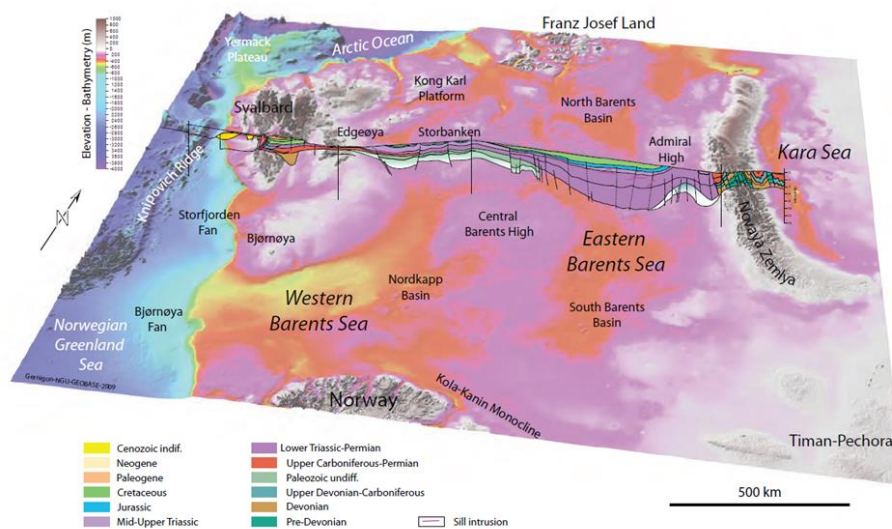

Figure 3.2 *- Elevation and bathymetry of the Barents Sea continental shelf together with an E-W orientated regional profile that highlights the distinct differences between the western and eastern geological provinces that are separated by a generally monoclinal structure with a north-south trend. Figure adapted from Smerlor (2009).*

While the basement evolution of the entire Barents Sea is very complex, and locally not fully resolved, it was most likely formed by the continent-continent collision of the Paleoproterozoic Svecofennian orogeny as part of the Baltic (or Fennoscandian) Shield and the accreted, superimposed fold-and-thrust belt of the Neo-Proterozoic Timanide Orogen (Smerlor, 2009). The final tectonic event that significantly influenced the basement was the Caledonian Orogeny, which followed the eastward subduction of the Iapetus Ocean that resulted in a continent-continent collision and consolidated the Laurentian and Baltican plates into the Laurasian continent. This event occurred around 400-500 million years ago and the resulting Scandinavian Caledonides (Figure 3.3) is regarded as the most important contributor in the formation of the basement of the Svalbard and the West Barents Sea (Smerlor, 2009; Stange, 2009). On Svalbard, the broad array of rocks that constitute the basement include sediments (e.g., shale, sandstone, conglomerate, limestone, dolostone, tillite), metasediments (e.g., marble, quartzite, phyllite, schist, gneiss), and igneous rocks (e.g., granite, volcanic rocks), and metamorphic rocks (e.g., eclogite, blueschist, migmatite) (Elvevold, 2007; Worsley, 2008). Collectively, these rocks

are referred to as "Heckla Hoek" and can be found on Prins Karls Forland, along the entire west coast and some of the northern parts of Spitsbergen, in the northern Hinlopen Strait, Nordaustlandet, and a small area of Bjørnøya where they tend to be well-exposed as N-S striking bedrock with sharp, ragged peaks (Elvevold, 2007; Worsley, 2008; Stange, 2009).

Following the Caledonian orogeny, the Eastern Barents Sea remained tectonically active as the progressive closure of the Uralian Ocean initiated a continental-continental collision between Baltica and Kazakhstan (Figure 3.3) during the Carboniferous that resulted in the formation of the Ural Mountains (Smerlor, 2009). Contrastingly, during Devonian to Early Carboniferous times, the Western Barents Sea was characterized by exhumation and extensive erosion that lead to the deposition of the first sediment on top of the basement. These sediments consist of a series of fine-grained siltstones, sandstones, and coarse conglomerates that are collectively called *Old Red* as their high hematite content gives them a distinctive reddish color (Smerlor, 2009; Stange, 2009). As Svalbard slowly and continuously drifted northward towards the tropical latitudes during the late Paleozoic, the depositional environment of the Western Barents Sea gradually transformed from continental and lacustrine to shallow lagoons and finally marine carbonate shelf conditions. As the sea level continued to rise, deeper basins developed and the climate went from humid to arid. These conditions created a variety of sedimentological successions consisting of sandstone, limestone, and coal, occasionally with abundant fossils (e.g., brachiopods, bryozoans, corals), that nowadays are well exposed in the Billefjord-Tempelfjord area of central Spitsbergen (Worsley, 2008; Smerlor, 2009; Stange, 2009).

As Svalbard continued to move to the north during the Mesozoic era, the climate seemed to be mostly temperate/damp, and the Western Barents Sea remained tectonically relatively calm as the rifting episodes associated with the opening of the North Atlantic had yet become an important factor for the region and post-rift thermal subsidence was still dominant (Elvevold, 2007; Smerlor, 2009; Stange, 2009). As the Triassic progressed, shallow-water siliciclastic shelves turned into restricted anoxic basins and to coastal plains/near-shore shallow-marine conditions as progressive uplift occurred and the Middle Jurassic regression reached its maximum (Smerlor, 2009; Koevoets et al., 2018). The predominant fine-grained, dark and uniform shales deposited during this period have a high organic carbon content and contain numerous fossils (e.g., ammonites, shells, and even dinosaurs) (Worsley, 2008; Smerlor, 2009; Stange, 2009). Together with coarse sandstones that are considered to be the most prolific petroleum reservoirs in the southwestern Barents Sea, these shales are well-preserved and exposed in central and southeastern parts of Spitsbergen and the islands of Edgeøya, Barentsøya, Wilhelmøya, Kong Karls Land, Hopen, and Bjørnøya (Worsley, 2008; Stange, 2009; Henriksen et al., 2011; Grundvåg et al., 2017). Towards the end of the Jurassic, the regression was followed by a maximum transgression that flooded the entire Barents Shelf (Smerlor, 2009). The North Atlantic rifting predominantly influenced the western margin of the Barents Shelf and its continued northern progradation lead to the development of a marine connection across this shelf (Figure 3.3) (Smerlor, 2009). North Atlantic rifting climaxed in the Hauterivian and was accompanied by uplift and volcanic activity, which peaked in the Barremian to early Aptian on Svalbard, Frans Josef Land, and nearby shelf areas and formed basaltic/dolerite dyke swarms at shallow depths below the surface (Elvevold, 2007; Smerlor, 2009; Stange, 2009; Corfu et al., 2013; Grundvåg et al., 2017).

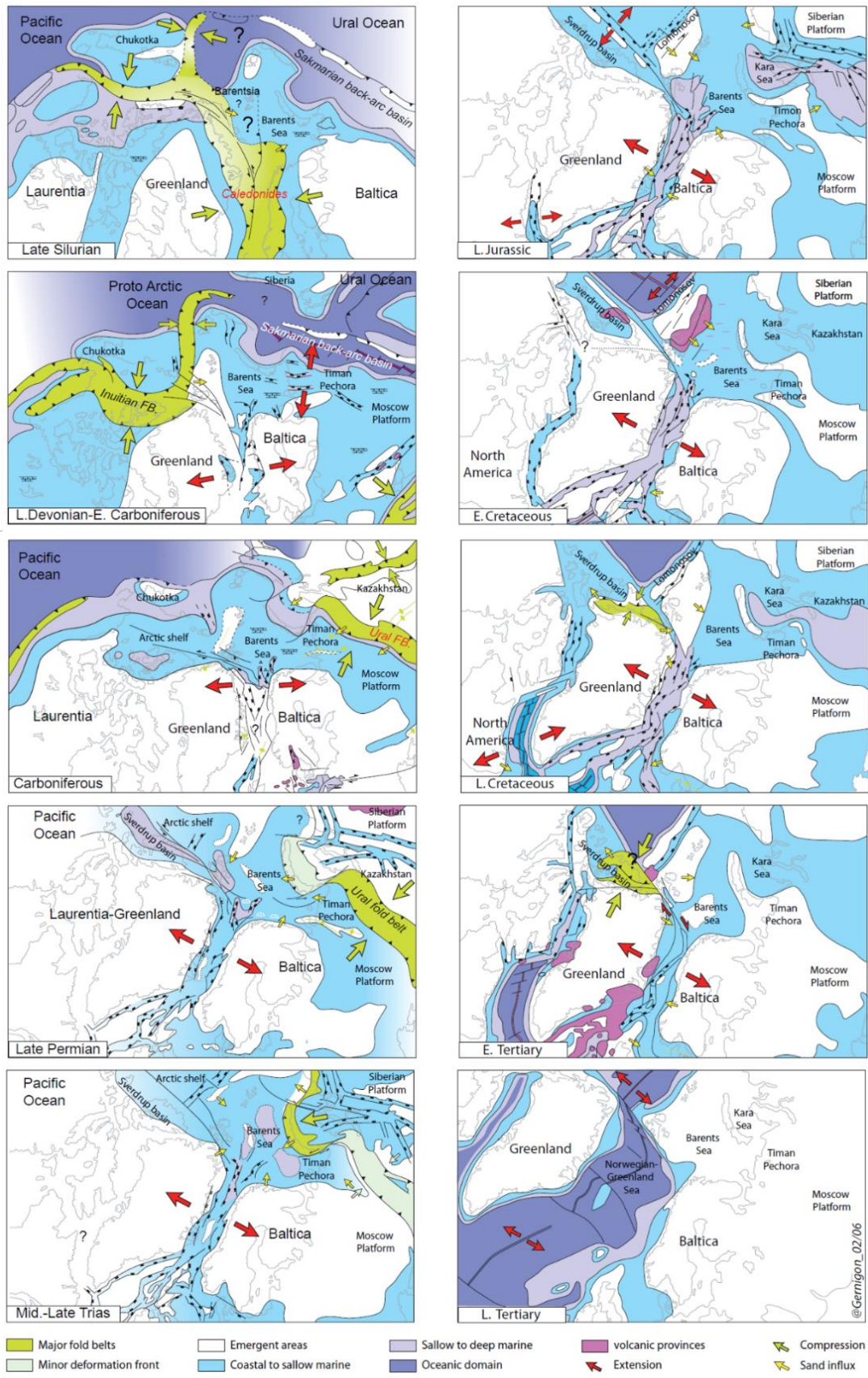**Figure 3.3** - *Schematic overview of the tectonic history and evolution of the North Atlantic and Artic regions from the Late Silurian (top left) to the Late Tertiary (bottom right). Please note that, although the term Tertiary is still used, it is no longer recognized as a formal unit by the International Commission on Stratigraphy and is now subdivided into the Paleogene and Neogene. Figure adapted from Smerlor (2009).*
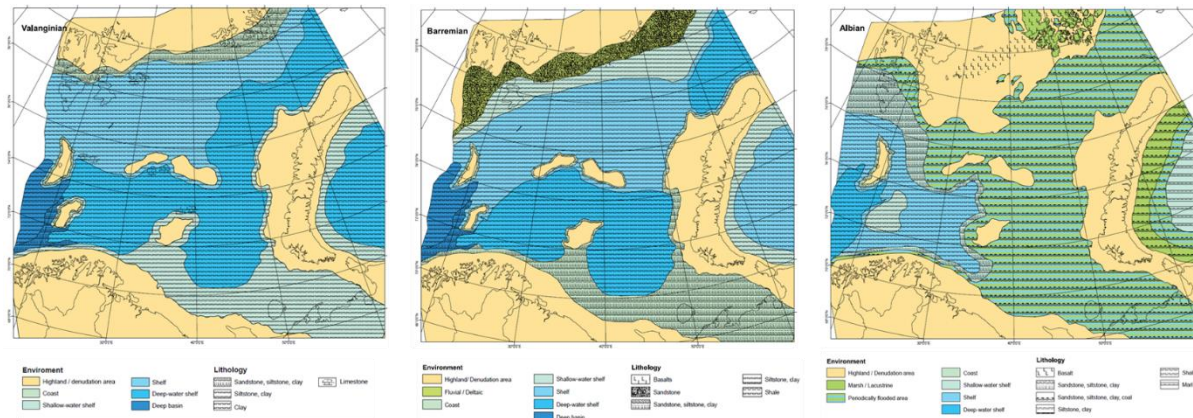
19

Figure 3.4 - *Paleogeographic reconstructions of the depositional environment and associated lithology of the sedimentary basins in Svalbard and the Barents Shelf during different time intervals in the Cretaceous (left: Valanginian, middle: Barremian; right: Albian). Figure modified after Smerlor (2009).*

During the Early Cretaceous, the southern part of Svalbard was part of an epicontinental sea and shallow-shelf to deep-marine clastic sediments were prevalent over large areas of the Barents Shelf (Figure 3.4), while deposition of carbonate sequences continued in the platform areas (Worsley, 2008; Koevoets et al., 2018; Vickers et al., 2018). The sedimentary successions from the Lower Cretaceous on Svalbard are part of the Adventdalen group and are divided into the Berriasian-Barremain Rurikfljellet Formation, the Barremian Helvetiafjellet Formation, and the Aptian-Albian Carolinefjellet Formation. Together, these formations form a regressive-transgressive megacycle that resulted in a depositional environment that transformed from a marine shelf towards a shallower delta/flood-plain that is subsequently flooded again (Dypvik et al., 1991; Grundvåg et al., 2017; Koevoets et al., 2018). While the Lower Cretaceous deposits are quite abundant on Svalbard, sediments from the Upper Cretaceous are absent in the geological record of the archipelago due to complete subaerial exposure of the archipelago during these times (Harland et al., 1997; Vickers et al., 2016).

The Rurikfjellet Formation is subdivided into the basal Myklegardfjellet Bed, the Wimanfjellet Member, and the uppermost Kikutodden Member. The Myklegardfjellet Bed is a unit of clay that was deposited after a significant hiatus with the strata immediately below in starved shelf conditions that accompanied maximum flooding during the Valanginian (Figure 3.4) and potentially the uppermost Ryazanian (Wierzbowski et al., 2011; Koevoets et al., 2016; Grundvåg et al., 2017). The sedimentary successions of the offshore Wimanfjellet Member are shale-dominated and contain mudstones which gradually grade upwards into the packages of shales, siltstones, and very-fine sandstones of the Kikutodden Member (Dypvik et al., 1991; Grundvåg et al., 2017; Vickers et al., 2018). The Kikutodden Member was deposited in a lower shoreface setting during the late Hauterivian and in Festningen it has distinct intervals that contain hummocky cross-stratification, belemnites/bivalves, pyrite concretions, and/or wood pieces (Dypvik et al., 1991; Grundvåg et al., 2017; Vickers et al., 2018). Contact with the overlying Helvetiafjellet Formation is generally abrupt and has been suggested to be a result of thermal doming and a pulse of igneous activity associated with the emplacement of the High Arctic Large Igneous Province (HALIP) (Maher, 2001; Petersen et al., 2016; Vickers et al., 2016). The Helvetiafjellet Formation is subdivided into the lower Festningen Member and the upper Glitrefjellet Member. Although the boundary of this formation with the overlying Carolinefjellet Formation is believed to be conformable, the abrupt deepening of

facies prompts authors to suggest that at certain locations both formations are separated by a major subaerial unconformity (Gjelberg and Steel, 1995; Midtkandal et al., 2008; Vickers et al., 2016; Grundvåg et al., 2017). While the Festningen Member consists of fine- to very coarse-grained pebbly sandstones and conglomerates with abundant cross-stratification indicative of fluvial settings on a braid-plain during the early Barremian, the Giltrefjellet exhibits alternations with variable amounts of mudstones, sandstones, and thin coal layers deposited in continental to paralic settings up to around the early Aptian (Worsley, 2008; Smerlor, 2009; Grundvåg et al., 2017). Estimations of paleocurrent directions indicate a predominant southeastward direction (Grundvåg et al., 2017), which fits quite well with the paleogeographic reconstruction for the Barremian (Figure 3.4).

The Carolinefjellet Formation is subdivided into the Dalkjegla Member, the Innkjegla Member, the Langstakken Member, Zillerberget Member, and the Schönrockfjellet Member based upon the predominance of sandstone or shales (Vickers et al., 2016; Grundvåg et al., 2017). Of these 5 members, only the Dalkjegla and Innkjegla Member are formally defined and together with the Langstakken Member also the members that are predominantly exposed (Vickers et al., 2016). The lowermost Dalkjegla Member consists of a thick package of shale or siltstone that contains thin intervals of fine sandstone and pyrite concretions with current ripples and hummocky cross-stratification deposited in a restricted to open marine shelf setting (Vickers et al., 2016; Grundvåg et al., 2017). Both the general coarsening upward trend in the lower part of the Dalkjegla Member and the predominance of hummocky cross-stratification are indicative of a transition from an offshore towards lower shoreface depositional setting on a shallow open-marine shelf that is strongly influenced by storms (Smerlor, 2009; Grundvåg et al., 2017). Towards the transition to overlying Innkjegla Member, sandstone layers become less prominent and are replaced by thin layers of pyrite concretions. A trend that suggests sediment starvation and an overall retrogradational trend towards a slightly deeper shelf setting, in which the shale-dominated Innkjegla Member is deposited (Worsley, 2008; Grundvåg et al., 2017).

After deposition of the Lower Cretaceous deposits, a complex phase of deformation that took place during the Late Paleocene and Eocene lead to the formation of the Eurekan Fold-Belt (Figure 3.3), which had some important tectonic implications for both Svalbard and the Barents Shelf region (Leever et al., 2011; Petersen et al., 2016). The northward drift of Greenland together with seafloor spreading west (i.e., Baffin Bay), east (i.e., Eurasia), and south (i.e., Labrador Sea and North Atlantic) of the now separate Greenland plate resulted in transpression and/or compression that resulted in the formation of the West Spitsbergen Fold and Thrust Belt (WSFTB) (Figure 3.1B; Figure 3.5), which is about 500 km long and 100-200 km wide and is estimated to have imposed a crustal shortening of around 20-40 km (Worsley, 2008; Leever et al., 2011; Piepjohn et al., 2013; Petersen et al., 2016). Deposition of the Paleocene-Eocene successions of Svalbard occurred in the Central Tertiary Basin, which is the foreland basin that evolved as a response to the WSFTB around 61-62 Ma (Leever et al., 2011; Petersen et al., 2016; Jones et al., 2017). After the termination of rifting in the Labrador Sea and Baffin Bay, Svalbard moved along the transform De Geer Fault Zone until it reached its present-day location (Piepjohn et al., 2000; Tessensohn and Piepjohn, 2000; Piepjohn et al., 2013).
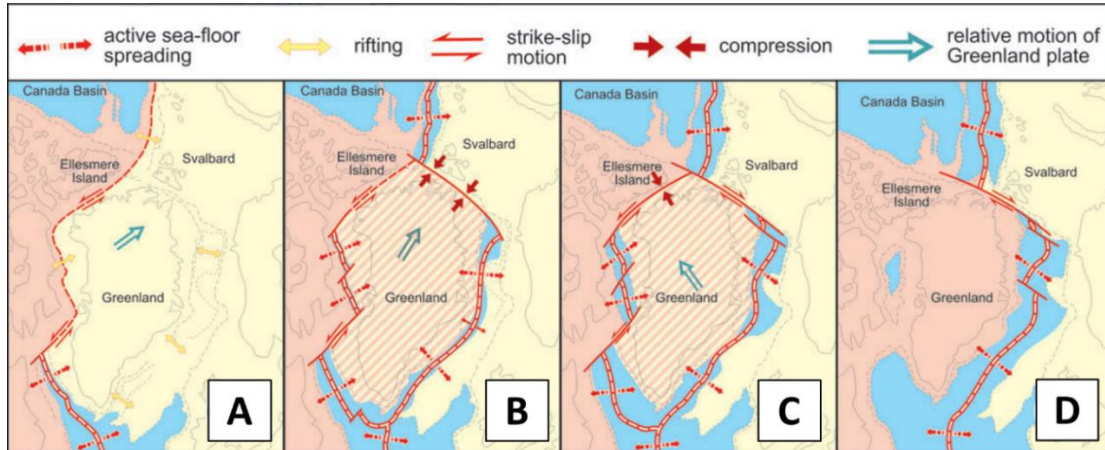
Figure 3.5 *- Plate tectonic reconstruction of different stages during the final break-up of Laurasia with an emphasis on the role of Greenland. (A) Pre-Eurekan situation during the Late Cretaceous (68 Ma) where Greenland is still part of the European plate. Seafloor spreading in the North Atlantic and Labrador Sea and rifting in the Eurasian basin and Baffin Bay. (B) First stage of the Eurekan deformation during the Early Eocene (55 Ma) with Greenland as a separate plate surrounded by seafloor spreading and compression along the continental margin off Norway and the Barents Sea. (C) Second stage of the Eurekan deformation during the Late Eocene (49 Ma), in which Greenland is still a separate plate, but started to move in a different direction that results in strike-slip motion along the continental margin off Norway and the Barents Sea and compression at Ellesmere Island. (D) Post-Eurekan situation, Late Eocene (36 Ma), that is followed by the opening of a deep-water connection between the North Atlantic and Eurasian Basin along the Fram Strait in the Miocene. Figure modified after Tessensohn and Piepjohn (2000) and Piepjohn et al. (2013).*

3.2. Analytical methods

During the fieldwork campaign that was realized in June 2017, a careful bed-by-bed investigation for glendonites was undertaken in the outcrops of the studied sections at Festningen (Figure 3.1A; 78.09910°N, 13.94257°E) and Grumantbyen (Figure 3.1A; 78.17498°N, 15.10689°E). The location of glendonite horizons and associated other types of authigenic carbonates, including nodules, concretions, infillings of burrows, or discontinuous layers were recorded using high-resolution conventional lithostratigraphic logging, paying close attention to the types of sediment, grain-sizes, sedimentary structures, and body/trace fossils. Macro-plant material and fossilized wood together with bivalves and belemnites were also collected and recorded. Wherever possible, additional care was put into sampling bulk rock samples of the sediment and associated authigenic carbonates as close as possible to each of the glendonite horizons to increase the fidelity of in-depth comparisons.

Using a diamond rock saw, all samples were ideally cut into 2 or 3 separate pieces while the leftover material was saved. One of these pieces was selected for the fabrication of thin-sections, while the others were cut on all sides (to remove weathered surface layers and prevent contamination) and used for subsequent analysis.

A total of 35 polished, uncovered thin-sections of approximately 30 µm thickness from glendonites and 41 thin-sections from the associated authigenic carbonates, conglomerates, belemnites, and sediments were created and studied with optical microscopy using a LEICA DM2500 and Leica DM6000 B microscope together with the Leica Application Suite software at Utrecht University. UV fluorescence was used in conjunction with a Leica DM6000 B microscope and a FLUO-Filtertube I3 to identify preserved organic content within carbonate phases (i.e., highly fluorescent), in similar fashion to Qu et al. (2017) and Morales et al. (2017b), and to provide additional support for distinguishing between the different growth phases within the glendonites. Although helpful, it is important to note that there are also other phenomena (e.g., manganese-rich carbonate phases) that can produce fluorescence, which means that this technique thus only provides a qualitative guideline. Estimations for size, volume %, and other quantifications of the different carbonate phases were performed on microphotographs from parts of the specimen that were deemed to be representative of the entire glendonite.

Using a Böhler Monster Regel-Netzteil II handheld micro-drill, powdered subsamples from each of the pieces designated for analysis were collected for carbon and oxygen stable isotope analysis. While this approach is not ideal for answering the aforementioned research questions, it was inherited from the earlier stages of the project, which had a different scope, and could not be adapted anymore based primarily upon time constraints. Following this drilling procedure, each subsample was analyzed together with IAEA-CO-1 (No. 221) and Naxos standards using a Thermo Fisher Scientific GasBench II at the isotope lab of the Utrecht Castel center. As this bulk isotope method is typically only used for samples that contain 100% carbonate, the amount of subsample used for the analysis of each sample was higher than the conventional amount and varied based upon their respective estimated carbonate percentages. The $\delta^{13}C_{carb}$ and $\delta^{18}O_{carb}$ values of the samples are reported in the δ-notation relative to the Vienna Peedee Belemnite (VPDB) standard.

3.3. Macro- and microscopic reference frame

To enable proper recognition of the internal structure of glendonites, the existing research was compared and used to construct a framework that will be used as a reference frame during the remainder of this report. The following section will provide an overview of the most important macro- and microscopic characteristics of glendonites that have been reported to date and will simultaneously also serve as a guideline for the terminology that is used in the remainder of this report.

Glendonites, the pseudomorphs after ikaite type 3, are typically found within shallow to deep marine sediments, where they form macroscopic single euhedral to stellate crystals clusters (Figure 2.1F-H). While they are inclined to form stellate concretions or clusters of up to hundreds of crystals with either a circular or slightly asymmetric shape, similar to the shape of ikaite, they can take on other shapes (Figure 3.6) (Kaplan, 1978; Selleck et al., 2007; Morales et al., 2017b). The size of glendonites generally ranges from a diameter of less than 10 cm for the *stellate concretions* (Figure 3.6A-D) up to 30 cm lengths for *single acinaciform* crystals (Figure 3.6E) (Morales et al., 2017b), also referred to as *triangular* (Qu et al., 2017). By convention, this size is always less than that of the original ikaite crystal as recrystallization to anhydrous $CaCO_3$ polymorphs is accompanied by a reduction in volume of approximately two-thirds and consequently the creation of pore space (De Lurio and Frakes, 1999; Huggett et al., 2005; Selleck et al., 2007; Peckmann, 2017; Qu et al., 2017). Aside from these *stellate concretions* and *single acinaciform*, glendonites have also been shown to form *small aggregates of crystals* (anhedral) or *aggregates of acinaciform crystals* (usually 2 or 3) that exhibit bi- and tri-pyramidal shapes or twining (Figure 3.6F-G) (Teichert and Luppold, 2013; Morales et al., 2017b). In exceptional cases, these aggregates are able to build very large glendonites structures of up to 60 m, such as in those found in the Eocene deposits of Denmark and the Bajocian deposits of northeast Siberia, of which there is no known ikaite precursor today (Pedersen and Buchardt, 1996; Morales et al., 2017a; Morales et al., 2017b). Additionally, glendonites are commonly found within carbonate concretions (Selleck et al., 2007; Qu et al., 2017; Morales et al., 2017a; Vickers et al., 2018) or intraformational conglomerate beds (Figure 3.6H) (Morales et al., 2017a) and can be widespread during specific time intervals (Morales et al., 2017b). Although glendonite-bearing horizons tend to contain glendonites with similar morphologies (Grasby et al., 2017), some successions have also been shown to harbor glendonites with different morphologies (Kaplan, 1978; Teichert and Luppold, 2013; Morales et al., 2017a). This discrepancy is one of the reasons that a distinct link between environmental conditions, morphology, and internal structure has yet to be found (Grasby et al., 2017; Morales et al., 2017b). However, some authors suggested that supersaturation with respect to ikaite, the porosity of the host sediment, and the growth rate of ikaite could be some of the governing factors (Morales et al., 2017b). Aside from their various shapes, glendonites also display a variety of colors (Figure 3.6). These colors range from grey to yellowish, light and dark amber, to brownish and are thought to be solely related to the type of carbonate infillings that occupy the pore space (Morales et al., 2017b).

While Boggs and Hull (1975) and Kaplan (1978) were the first to use petrological observations to create detailed descriptions of glendonites, many other authors (Greinert and Derkachev, 2004; Huggett et al., 2005; Teichert and Luppold, 2013; Geptner et al., 2014; Grasby et al., 2017; Qu et al., 2017; Rogov et al., 2017; Morales et al., 2017a) have tried to describe and compare the complex paragenetic sequences within glendonites in order to find patterns that are independent of size, morphology, location, and age. Based upon these efforts Morales et al. (2017b) established that glendonites contain 3 prevailing phases of calcite growth that can be recognized in all glendonites. Beside these 3 prevailing phases of calcite growth, certain specimens also contain an additional phase related to recrystallization and occasionally harbor clays and quartz grains, shell fragments, and fossils that were part of the host sediment. Furthermore, dark micritic mud is often found around a part or the totality of glendonite rims (Morales et al., 2017b). The characteristics of each of these calcite phases will be discussed below:
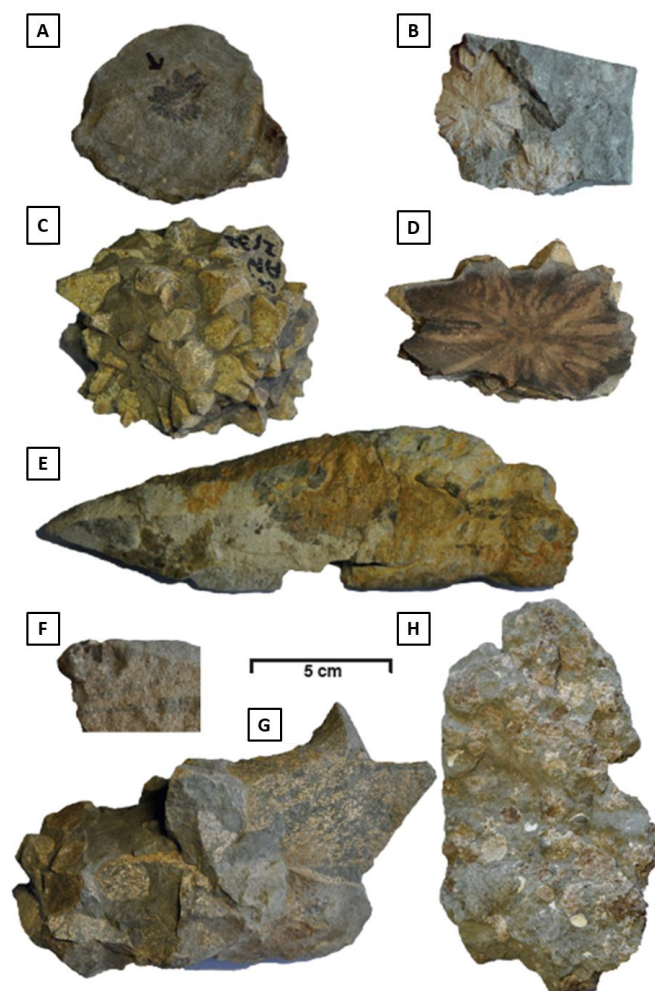
*Figure 3.6 – Picture overview of macroscopic glendonite types based upon samples found in Jurassic sedimentary deposits in Siberia (Morales et al., 2017a). **(A)** Small stellate glendonite in a calcitic nodule, section of Chekurovka, uppermost lower-middle Bathonian; **(B)** Small stellate pseudomorphs, section of Cape Khorongkho, lowermost upper Bajocian; **(C)** and **(D)** Medium-size stellate specimen, section of Anabar bay, upper Pliensbachian; **(E)** Large single acinaciform glendonite, section of Anabar Bay, upper Pliensbachian; **(F)** Specimen composed of small aggregates of crystals, section of Chucha, Bathonian; **(G)** Pseudomorph composed of large aggregates of crystals, section of Anabar Bay, uppermost Pliensbachian; **(H)** Sandy glauconitic conglomerate bearing reworked pebbles and glendonites, section of Cape Kystatym, lowermost upper Bajocian. Figure adapted after Morales et al. (2017b).*

The first phase in the paragenetic sequence of glendonites that has been found in all of the petrographic studies constitutes typically white/transparent calcite crystals, often organized in bipyramidal shapes that are inclined to form a network of *rosettes* (Figure 3.7A-H) or contain elongated/oval and irregular shapes. Especially the shape of these *rosettes* strongly reflect the original crystal aggregates of ikaite (Qu et al., 2017; Morales et al., 2017b). The size of this first phase generally ranges from 100 μm to 1.5 mm, with conflicting evidence suggesting that in certain cases smaller crystals and in other larger crystals are preferentially found within the center of the glendonites (Teichert and Luppold, 2013; Morales et al., 2017b). This phase typically does not contain any particular structure or twinning (common within calcite), but can also be heterogeneous and reveal concentric zonations with increasing $MgCO_3$ content (Qu et al., 2017; Morales et al., 2017b). Compositionally, the first phase consists of almost pure low-Mg calcite as shown by its dark color under UV light (Qu et al., 2017; Morales et al., 2017a), cathodoluminescence (Teichert and Luppold, 2013; Qu et al., 2017; Vickers et al., 2018), and scanning electron microscope analyses (Greinert and Derkachev, 2004; Teichert and Luppold, 2013; Qu et al., 2017). Another distinct characteristic of this phase is the presence of circular to elongated dark impurities that tend to be very luminescent under UV light, suggested to indicate the preservation of OM (Figure 3.7B-F) (Qu et al., 2017; Morales et al., 2017b). Within the literature, this phase has been dubbed as *Ros* (Boggs and Hull, 1975) or *rosettes* (Morales et al., 2017a), *type 1* (Huggett et al., 2005; Vickers et al., 2018), *primary calcite* (Greinert and Derkachev, 2004), *replacive calcite* (Qu et al., 2017), as well as *inclusion-zoned calcite (IZC)* (Grasby et al., 2017). It is commonly believed that this first phase is very likely to be the result of a direct ikaite-to-calcite transformation (Teichert and Luppold, 2013; Qu et al., 2017; Morales et al., 2017b). In the remainder of this report, this phase will be referred to as the *Ros*.

The borders of many of these first phase crystals are frequently flattened or truncated, indicative of dissolution, and overgrown by fibrous calcite along the axis of the initial crystals (Morales et al., 2017b). These stepwise overgrowths, referred to as *Rov* (Figure 3.7C-E) by Morales et al. (2017b) and *type 1b* by Huggett et al. (2005), incorporate various amounts of Ca-replacing elements (e.g., Mg or Mn) and organic impurities giving them a color that consists of different shades of amber in normal light as well as a bright luminescence under UV light and cathodoluminescence (Teichert and Luppold, 2013; Qu et al., 2017; Morales et al., 2017b). Despite that the first phase and their overgrowths have often been subjected to dissolution or recrystallization, their contours are usually still recognizable due to the insoluble nature of the organic impurities (Figure 3.7G-H) (Morales et al., 2017b). Within the context of this report, these overgrowths will subsequently be referred to as *Rov*.

The second phase is characterized by carbonates that form anisopachous to isopachous rims around *the first phase* and their stepwise overgrowths (Morales et al., 2017b). These rims are likely to encompass multiple generations of growth that can be formed early after crystallization of the first phase as well as relatively late and thereby constituting the final phase within of the paragenetic sequence (Morales et al., 2017b; Vickers et al., 2018). Based upon the precipitation conditions (e.g., porewater chemistry) and the preservation of the glendonites, these rims can be more or less developed and have consequently been described in many different ways: fibrous (Fib, Figure 3.7B) (Boggs and Hull, 1975), spherulitic (Huggett et al., 2005), radiaxial-fibrous (Frank et al., 2008), fibrous spherulitic and forming syntaxial rims (Huggett et al., 2005), columnar infilling calcite (Teichert and Luppold, 2013), microsparitic to spiritic and euhedral rims (Greinert and Derkachev,

2004), isopachous Fe- or Mg-bearing calcite rim cements (Qu et al., 2017), botryoidal calcite (Vickers et al., 2018), or fibrous to botryoidal (Figure 3.7C-D, F) (Morales et al., 2017a). All these various expressions are typically referred to as *type 2* or *Type II calcite* (Huggett et al., 2005; Vickers et al., 2018), *second carbonate phase* (Greinert and Derkachev, 2004), *Mg- and Fe-rich carbonates* (Teichert and Luppold, 2013). The color of this phase ranges from different shades of yellowish-amber across a spectrum of light yellow to dark amber-brown and usually remains dark under UV light and cathodoluminescence (Teichert and Luppold, 2013; Rogov et al., 2017; Morales et al., 2017b). Other characteristics include: the presence of minor amounts of Sr and Mn (Teichert and Luppold, 2013), etched boundaries suggesting alternations between dissolution and precipitation (Vickers et al., 2018), and an association with glauconite grains (50-100 µm) whose undamaged shape suggests authigenic formation (Light, 1952; Morales et al., 2017b). During this research, this particular phase will be referred to as the *Bot*.
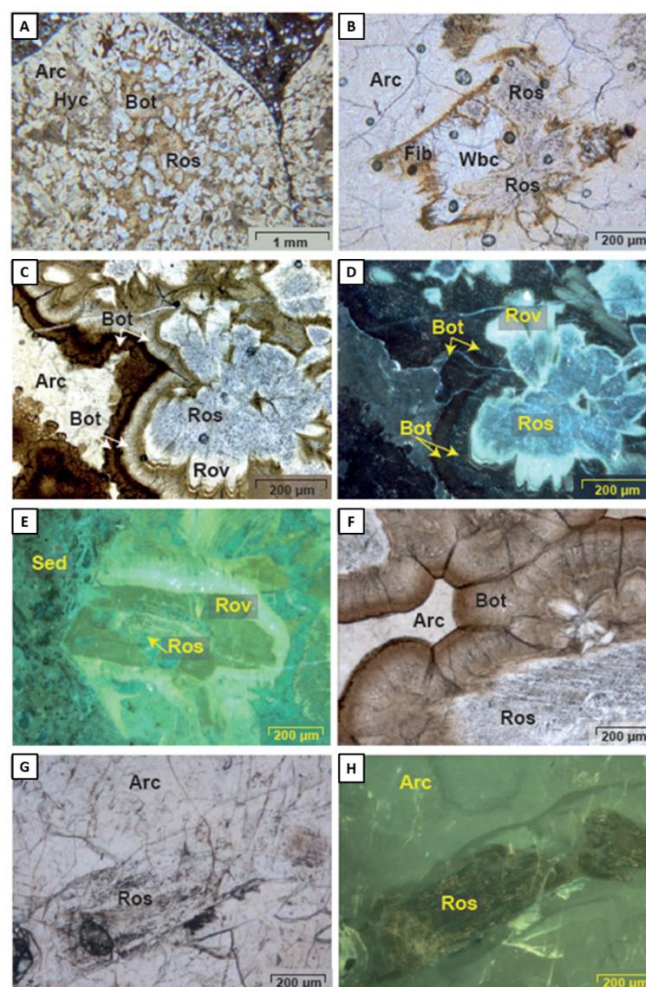

Figure 3.7 – *Microphotographs of glendonites adapted from Morales et al. (2017b). (A) Overview of the general phases present in glendonites with crystals from the first phase forming a network of rosettes (Ros), followed by the precipitation of the second phase as botryoids (Bot) around the rosettes, and recrystallization of part of the sample by anhedral yellow calcite (Arc) containing hydrocarbons (Hyc); lower-middle Bathonian sample from the Chekurovka section. (B) Preservation of rosette crystals (Roc) in a sample that is strongly recrystallized by anhedral yellow calcite (Arc), and surrounded by brown fibrous carbonates (Fib). Empty pores are filled by white blocky calcite (Wbc); upper Pliensbachian sample from the Anabar Bay section. (C-D) Close-up of rosette network and stepwise overgrowths of fibrous calcite (Rov) as well as the distinct stages of the botryoidal overgrowths (Bot) in transmitted and UV light respectively; upper Bajocian-Bathonian samples from the Chekurovka. (B-F) Organic impurities present within rosette crystals that are luminescent under UV light.*

The third phase consists of white blocky calcite (Wbc, Figure 3.7B) (Morales et al., 2017b) or clear calcite spar (Vickers et al., 2018) that is typically considered to be the final generation of diagenetic calcite growth as it is often observed to fill the remaining pore space (Huggett et al., 2005; Frank et al., 2008; Teichert and Luppold, 2013). However, this does not always seem to be the case as these cements are occasionally overgrown by fibrous calcites (Morales et al., 2017b) and are also found to be substituted by quartz or more uncommonly silica and dolomite (Peckmann, 2017; Qu et al., 2017; Morales et al., 2017b). While both the calcite and quartz cements show a similar dull fluorescence under UV light, the zoned rhombohedral dolomite crystals are remarkably fluorescent (Qu et al., 2017; Morales et al., 2017b). Within the remainder of this report, this phase will be referred to as *Cc* (i.e., calcite cement).

Aside from these 3 distinct phases, some glendonites also show partial or total recrystallization, that results in the precipitation of an anhedral amber colored or yellow calcite (*Arc*, Figure 3.7A-D, G-H) (Grasby et al., 2017; Morales et al., 2017b). This calcite has a clotted fabric, often shows a poikilotopic nature, fills the pyramidal points of the original ikaite crystal, and can form botryoidal to needle-like sparry overgrowths (Grasby et al., 2017; Morales et al., 2017b). It has also been found to contain organic inclusions and pyrite in minor quantities (Grasby et al., 2017; Morales et al., 2017b). As this anhedral calcite appeared to be affected by dissolution, Morales et al. (2017b) suggested that its formation could be linked to fluid exhaustion. In this report, this uncommon yellow calcite will be referred to as *YC*.

Using these macro- and microscopic guidelines, the external/internal structure, the expression and size of the prevailing carbonate phases, the nature of the border between the carbonate phases, and other characteristics (e.g., recrystallization, dissolution events, the presence of quartz grains) will be noted and used to categorize each glendonite. After each glendonite has been placed into a specific group based on external and internal structure, these groups will be analyzed for similarities in isotopic composition as well as their locality. By using this approach, it should hopefully become clear if external and internal structure is governed by these factors or not.

4. Results

4.1. Lithostratigraphic logs and glendonite horizons

An overview of the lithostratigraphic logs for the Festningen section (Figure 3.1; 78.09910˚N, 13.94257˚E) and the Grumantbyen section (Figure 3.1; 78.17498˚N, 15.10689˚E), together with their proposed correlation and relevant sample place markers, can be found in Figure 4.1 and Appendix A. It is important to note that the correlation between both sections is based upon the general stratigraphy and lithological trends, such as the distinct conglomerate beds (i.e., FA89 and GRUT cgmt), the pyrite concretions, and the predominance of siltstone as well as similarities between the glendonites from both sections. A more robust correlation was unfortunately impossible during this study as the Grumantbyen section lacks specific age constraints. The Festningen section (Figure 4.1) has a total thickness of around 940 m and is comprised of the lower Valanginian-Hauterivian Rurikfjellet Formation, the intermediate Aptian Helvetiafjellet Formation, and the uppermost Aptian-Albian Carolinefjellet Formation. Although a distinct thin bed of clay can be found at the bottom of the section, it is unclear if this bed represents the basal Myklegardfjellet Bed and therefore this unit has been left out.

The Rurikfjellet Formation itself constitutes about 620 m of this total thickness and can be subdivided into the lower Wimanfjellet Member (±530 m tick) and the upper Kikutodden Member (±90 m thick). The predominate lithology of the Wimanfjellet Member is siltstone which is alternated throughout the entire sequence by both continuous and discontinuous carbonate layers with a thickness of up to around 1 m. Within the bottom part of the member, the siltstone is also interspersed by 2 distinct 7-10 m beds consisting of organic-rich clays. Intervals with carbonate concretions and nodules can be found around 315 m, 335 m, 374 m, 472-480 m, 512-516 m, and 526-528 m. Other features include a bivalve found at 15 m, a wood piece in a coarser bed at 44 m, and the occurrence of a belemnite around 527,5 m. The 2 glendonite horizons that were identified are located at 463 m and 471 m. In contrast to the Wimanfjellet Member, the Kikutodden Member is less uniform and consists of slightly coarser siltstone that is interspersed by 1 to 1.5 m thick pyrite concretions with hummocky cross-stratification that are especially prominent in the upper part of the sequence. Carbonate concretions and nodules are represented especially well in the lower part of the sequence around 542-560 m, but they can also be found at 532-534 m, 571-576 m, 580-589 m, 596 m, 607-610 m, and 614-618 m. Occasionally, these carbonate concretions and nodules are accompanied by tubes and burrows. Belemnites and bivalves are more numerous in the Kikutodden Member than the Wimanfjellet Member and were found around 555-557 m, 563 m, and 598 m. Wood pieces were found at 544 m, 598 m, and 612 m and at certain intervals ichnofabrics were observed. Finally, glendonite horizons were identified at 542.5 m, 554 m, 557 m, 561-562 m, 563.5 m, and 600-601 m.
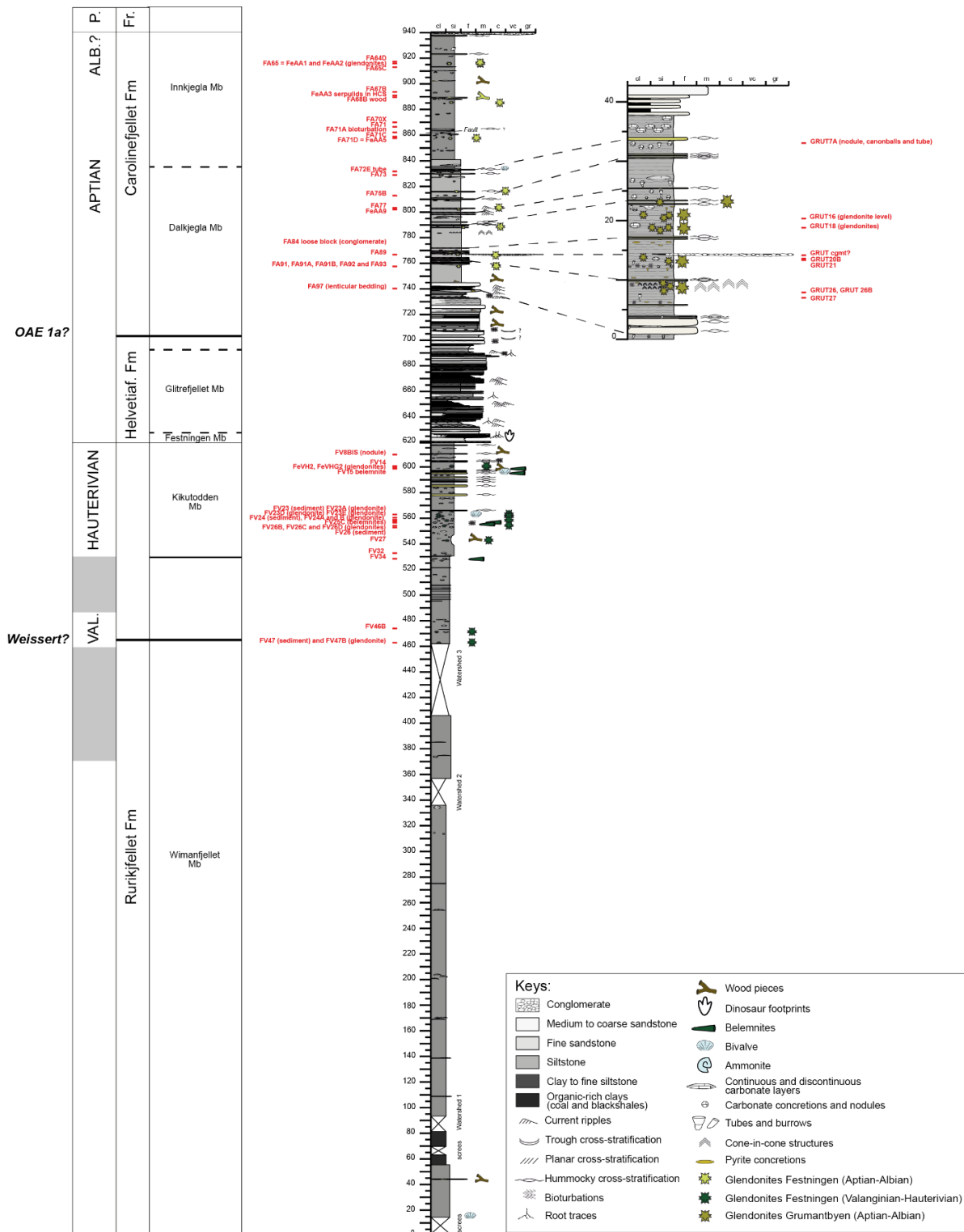
Figure 4.1 – *Lithostratigraphic log of the Festningen section (left; 78.09910˚N, 13.94257˚E) and Grumantbyen section (right; 78.17498˚N, 15.10689˚E) together with place markers for each samples that was used during this study. The proposed correlation between both sections shown here is based upon the general stratigraphy and lithological trends, such as the distinct conglomerate beds (i.e., FA89 and GRUT cgmt), the pyrite concretions, and predominance of siltstone as well as similarities between the glendonites from both sections. A more robust correlation was unfortunately impossible due to the lack of specific age constraints for the Grumantbyen section. For a larger and more defined version of this lithostratigraphic log, please refer to Appendix A.*

The intermediate Helvetiafjellet Formation represent 80-90 m of the total thickness and is subdivided into the basal Festningen Member (±15 m tick) and the overlying Glitrefjellet Member (±65-75 m tick). The lithology of the Festningen Member consists of 2-3 m thick fine sandstone and 0.3-0.5 m thick medium to coarse sandstone beds. While these fine sandstone beds are plain, the medium to coarse sandstone beds exhibit planar cross-stratification, traces of roots, signs of bioturbation, and even dinosaur footprints. Following this succession, the Glitrefjellet Member is comprised of thinner 0.5-1.0 m thick fine sandstone beds are increasingly alternated by uniform, 0.3-0.8 m thick clay to fine siltstone beds towards the upper part of the sequence. As these clay to fine siltstone beds become more prominent, the degree of planar cross-stratification, current ripples, and root traces in the fine sandstone beds decreases. The uppermost part of the Helvetiafjellet Formation (around 650-700 m), is comprised of about 3 coarsening-upward successions where 0.1-1.0 m clay to fine siltstone and siltstone beds are intercalated with infrequent organic-rich clays that transition into 0.4-0.9 m fine sandstone beds that exhibit distinct current ripples and planar cross-stratification, root traces, and signs of bioturbation. No glendonites were found within this entire sequence.

The Carolinefjellet Formation, which composes the final 230-240 m of the Festningen section, is only subdivided in the Dalkjegla Member (±135 m tick) and the Innkjegla Member (±105 m thick) as the youngest Langstakken, Zillerberget and Schönrockfjellet Members were not exposed. Lithologically, the Dalkjegla Member is predominately composed of siltstone that is interspersed by 0.6-0.8 m thick beds of fine sandstone with abundant current ripples, hummocky cross-stratified pyrite concretions with a similar thickness, and a very prominent conglomerate bed at 769 m. Carbonate layers, concretions and nodules, together with tubes and burrows, are mainly present in the upper part of the sequence around the alternating fine sandstone and pyrite concretion beds. Other features include wood pieces around 746 m, cone-in-cone structures at 784 m, and a bivalve in the uppermost pyrite concretion around 833 m. Around 835 m the Dalkjegla Member transitions into the Innkjegla Member as finer siltstone, reminiscent of shale, becomes dominant. The Innkjegla Member is thinner than the Dalkjegla Member and clearly represents more distal deposition as fine sand beds are absent and pyrite concretions are less abundant. The presence of continuous and discontinuous carbonate layers is especially pronounced at the fault, situated around 860-865 m, and in between the pyrite concretions around 902-913 m. Both carbonate concretions and nodules and tubes and burrows are more abundant in the Innkjegla Member than the Dalkjegla Member and are interspersed throughout the entire sequence. Ichnofabrics were only found in the bottom part of the member (around 848 m and 861 m), while wood pieces were identified in the middle to upper part of the member (around 889 m and 902 m). At 940 m, the Innkjegla Member is topped off by a distinct coarse conglomerate bed with a thickness of around 1.5 m. Glendonite horizons were found in the at 758 m, 788 m, 802 m, 816 m (Dalkjegla Member) and 857.5 m, 885 m, and 915 m (Innkjegla Member).

The Grumantbyen section (Figure 4.1), located close to an abandoned mine, has a thickness of approximately 42 m and is consists predominately of layered siltstone that is intercalated by about 0.2-0.4 m thick hummocky cross-stratified pyrite concretions that either occur as a single bed or as a multitude of smaller, closely interspaced beds. At the base of the section (around 1.5-3.5 m), 4 beds of hummocky cross-stratified medium to coarse sandstone with a thickness of around 0.2-1.3 m were found. The upper part of the section (around 37.5-42.0 m) consists of an alternation of around 0.5 m thick fine sandstone beds and 0.3-0.6 m thick layers of organic-rich clay, followed by a clear 1.7 m

thick medium to coarse sandstone bed that, contrary to the previous sandstone beds, lacks hummocky cross-stratification. This type of succession was not found at Festningen and may, therefore, be unique to the Grumantbyen section as it is also not readily observable at and other localities. While continuous and discontinuous carbonate layers, as well as carbonate concretions and nodules, are generally more abundant in the upper part of the section (especially around 22-27 m and 35-37 m), tubes and burrows can be found throughout the entire section and are occasionally pyritized. Ichnofabrics can be found within the siltstone and are prevalent around 16 m, 19 m, and 22.5 m. Another more unique feature exhibited within the host lithology are cone-in-cone structures that were only found around 18-19 m. All glendonite horizons in the Grumantbyen section were found in the supposed equivalent of the Dalkjegla Member (Festningen section) and are located at 9 m, 13 m, 18 m, 21 m, and 23 m. With the exception of the glendonite horizon at 561-562 m in the Kikutodden Member (Festningen section), the abundance of glendonites found within each particular horizon is typically higher in the Grumantbyen section than in the Festningen section.

4.2. Macro- and microscopic descriptions

The external morphology of the glendonites collected from the Lower Cretaceous Festningen and Grumantbyen section of Spitsbergen can be broadly divided into 6 groups based upon their shapes: (1) small aggregate of crystals (Figure 4.2H-I); (2) small to medium aggregate of crystals to stellate pseudomorph (Figure 4.2A-C; Figure 4.3A-B, E); (3) small stellate pseudomorph (Figure 4.2D-G); (4) small single acinaform (Figure 4.2J); (5) small double acinaform (Figure 4.2K); and (6) small stellate pseudomorph in carbonate concretion (Figure 4.2C-D). With the exception of the acinaforms and certain samples (e.g., Figure 4.2B,H,I; Figure 4.2A,E) that appear to have been flattened, the majority of the samples within each category are more or less spherical. Although the sample size varies considerably, even for samples from the same horzions, some trends can be identified. The smallest samples are found within the Rurikfjellet Formation and Innkjegla Member (Carolinefjellet Formation) from the Festningen section with slightly larger specimens within the Dalkjegla Member (Carolinefjellet Formation). Typical sizes range from around 0.4-0.8 cm (diameter) to 2.0 x 2.5 cm for the smallest samples to around 1.4 x 1.6 cm to 2.5 x 2.8 cm for the larger specimens. These sizes are considerably smaller than those of the samples found within the Grumantbyen section where the size ranges from around 2.0 cm (diameter) to 7.5 x 8.7 cm. Externally, the glendonites exhibit various colors ranging predominately from grey to dark, shades of light to dark amber, and occasionally also mimics rust (e.g., Figure 4.2A). In certain horizons, glendonites are broken up and integrated into loose conglomerates (e.g., FA84; Figure 4.1) or intraformational conglomerate beds (e.g., FA89, GRUT cgmt-a,b,c; Figure 4.1).

At a microscale, the internal morphology of the glendonites appears to be homogeneous (e.g., Figure 4.4A,C-H), but in certain cases also shows a separation between cores and rims (e.g., Figure 4.4B,I-K), or distinctive zonations (e.g., Figure 4.4I-L). Based upon the thin-section microphotographs (Figure 4.5-4.9) it seems that the internal structure of most glendonites is quite similar, however, when observed under a microscope, the carbonate infillings of each glendonite are actually very heterogeneous in terms of shape, size, and even fabric. As a result, some specimens with similar internal morphologies exhibit very different structures at a microscopic level, making it difficult to establish clear relationships.

Figure 4.2 – *Typical glendonite morphologies observed in the Festningen section (78.09910°N, 13.94257°E) of Svalbard, ranked according to stratigraphic height, with A representing the glendonite found within the youngest sedimentary deposit. The morphologies seen here are classified as: small aggregate of crystals (H-I), small aggregate of crystals to stellate pseudomorph (A-C), small stellate pseudomorph (D-G), small single acinaform (J), and small double acinoform (K). Images show glendonites at different scales as indicated by the provided tape-measures. See Appendix B1 for an overview of all observations.*

Figure 4.3 - *Typical glendonite morphologies observed in the Grumantbyen section (78.17498°N, 15.10689°E) of Svalbard, ranked according to stratigraphic height, with A representing the glendonite found within the youngest sedimentary deposit. The morphologies seen here are classified as: medium aggregate of crystals to stellate pseudomorph (A-B, E) and small stellate pseudomorph in carbonate concretion (C-D). Images show glendonites at different scales as indicated by the provided tape-measures. See Appendix B1 for an overview of all observations.*

Similar to the previous studies, the first phase within the paragenetic sequence or *Ros* constitutes sub-rounded/oval to rosette-like or lath-shaped crystals with a predominant transparent/grey to light amber yellow/brown color in PPL and a brown/dark color under UV (Figure 4.5-4.9). The size of these crystals varies greatly (Ø ±15-400 µm), not only between specimens but also within individual glendonites. On average, the sizes typically range from 75-175 µm. Aside from the infrequent internally zoned specimens, *Ros* lacks any clear structure and tends to exhibit a spotty/granular fabric due to the presence of abundant organic impurities. Although not always well-defined or present, in certain cases a distinction between *Ros* and a subsequent overgrowth (i.e., *Rov*), that does not belong to the second *Bot* phase, can be made. These overgrowths seem to preferentially grow on the narrow side of the crystals, and while their colors in PPL are similar to those of *Ros*, they gravitate towards brighter green tints under UV (potentially suggesting a higher degree of organic content) (Qu et al., 2017; Morales et al., 2017b). The relative contribution of *Ros* (and if present *Rov*) seems to be the highest within the glendonites that were found within the Innkjegla Member of the Aptian-Albian Carolinefjellet Formation (Festningen section) and the Grumantbyen section. Here, they constitute ±30-55% of the glendonite, which is much more than the ±10-35% of the glendonites from the Dalkjegla Member of the same formation and the ±5-15% for the Valanginian-Hauterivian glendonites from the Rurikfjellet Formation (Festningen section). This very low estimate for the zoned glendonites could actually be higher and thus closer to the expected value if the dark zonations interspersed between the botryoidal zonations of the second phase (Figure 4.8A-D) also prove to be manifestations of replacive calcite (i.e., *Ros*). Unfortunately, it was impossible to test or confirm this with our current approach and methodologies used.

The second phase in the paragenetic sequence or *Bot* consists of practically absent to large interconnected botryoidal overgrowths that show granular to mostly fibrous fabrics (Figure 4.5-4.9). Similar to *Ros*, the size of this phase varies considerably, even within the same specimen, with thicknesses ranging from 0-100 µm. The color of *Bot* phase can be transparent/grey to light and dark amber yellow/brown in PPL and partly depends upon whether the botryoidal overgrowths have developed distinct zonations (e.g., GRUT21, Figure 4.6D). When this is the case, the overgrowths gravitate towards forming an amber yellow to brown inner rim and a dark brown outer rim with a thicker transparent/grey area in between. Under UV, the color of the *Bot* phase is typically pale and bright to dark green or brown. Its relative contribution is highest (e.g., ±75-85%) within the zoned glendonites found within the Valanginian-Hauterivian Rurikfjellet Formation (Festningen section), where it is the main constituent of the macro-zonations and centers. For the unzoned glendonites from the same section, the contribution is the lowest with ranges from ±5-20%. The most substantial differences can be found within the glendonites from the Grumantbyen section where the estimated contribution varies from ±5-50%.

The third phase, or *Cc*, that appears consistently within the paragenetic sequence of all glendonites consists of anhedral/microcrystalline calcite to calcite spar (c.f., Figure 4.7G) that is found to fill the remaining pore space or in some cases late-stage fractures. In PPL, this phase appears to be mostly clear as it typically exhibits a distinct transparent/grey to occasionally light amber yellow color, but under UV is seems much dirtier due to a spotty fabric with a mix of green/brown to dark colors (Figure 4.6 and Figure 4.5 respectively). The estimated contribution of this phase is highest (±30-60%) within the glendonites from the Innkjegla Member of the Carolinefjellet Formation (Festningen section) (Figure 4.4A-B), where it appears to be more abundant within the center and less around the borders

of the pseudomorph. Although, some specimens show lower estimated contributions (i.e., FeAA9 and FA91-1; with ±10% and ±15%) most of the glendonites from the Dalkjegla Member of the Carolinefjellet Formation (Festningen section) show similar contribution with values from ±25-45%. The lowest estimations (around ±5-10%) are found within the zoned glendonites from Valanginian-Hauterivian Rurikfjellet Formation (Festningen section) and the unzoned glendonites from the Grumantbyen section. Interestingly, with the exception of FV26 (Figure 4.8C), the *Cc* phase only seems to occur within the center of the zoned glendonites. Morover, the relative contribution of the *Cc* phase within the glendonites of the Grumantbyen section may be higher than listed here as the boundary between *Bot* and *Cc* was often not very well-defined.
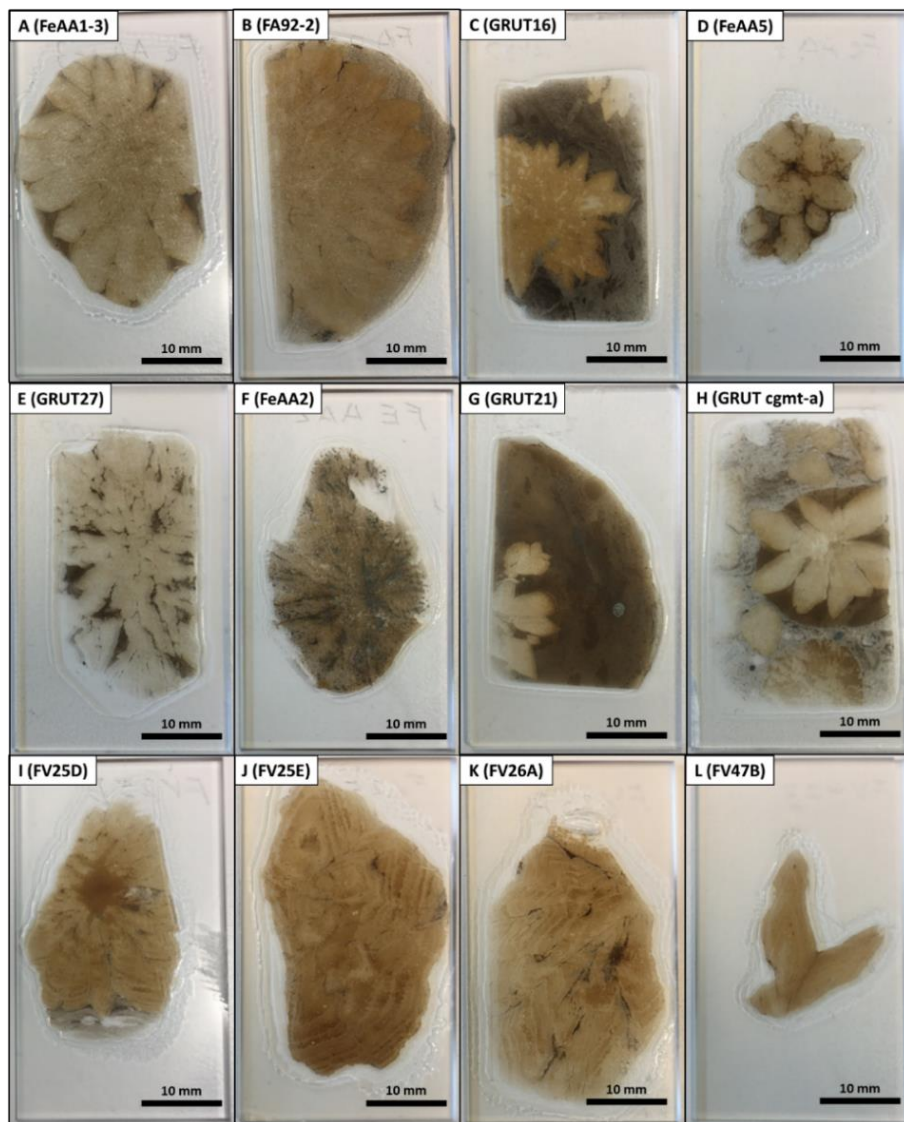

Figure 4.4 – *Photographs of thin-sections highlighting the internal morphology of the glendonites. These structures include unzoned and typically homogeneous specimens (e.g., A and C-H), specimens with a distinct difference between the core and rim (e.g., B, I, K), or specimens with microzoning (I-L). (A-B, C, E-F) Samples found within the Dalkjegla and Innkjegla Members of the Aptian-Albian Carolinefjellet Formation from the Festningen section (78.09910°N, 13.94257°E). (C, E, G-H) Samples found within the presumed Aptian Grumantbyen section. (I-L) Samples found within the Wimanfjellet and Kikutodden Member of the Valanginian-Hauterivian Rurikfjellet Formation from the Festningen section (78.09910°N, 13.94257°E).*
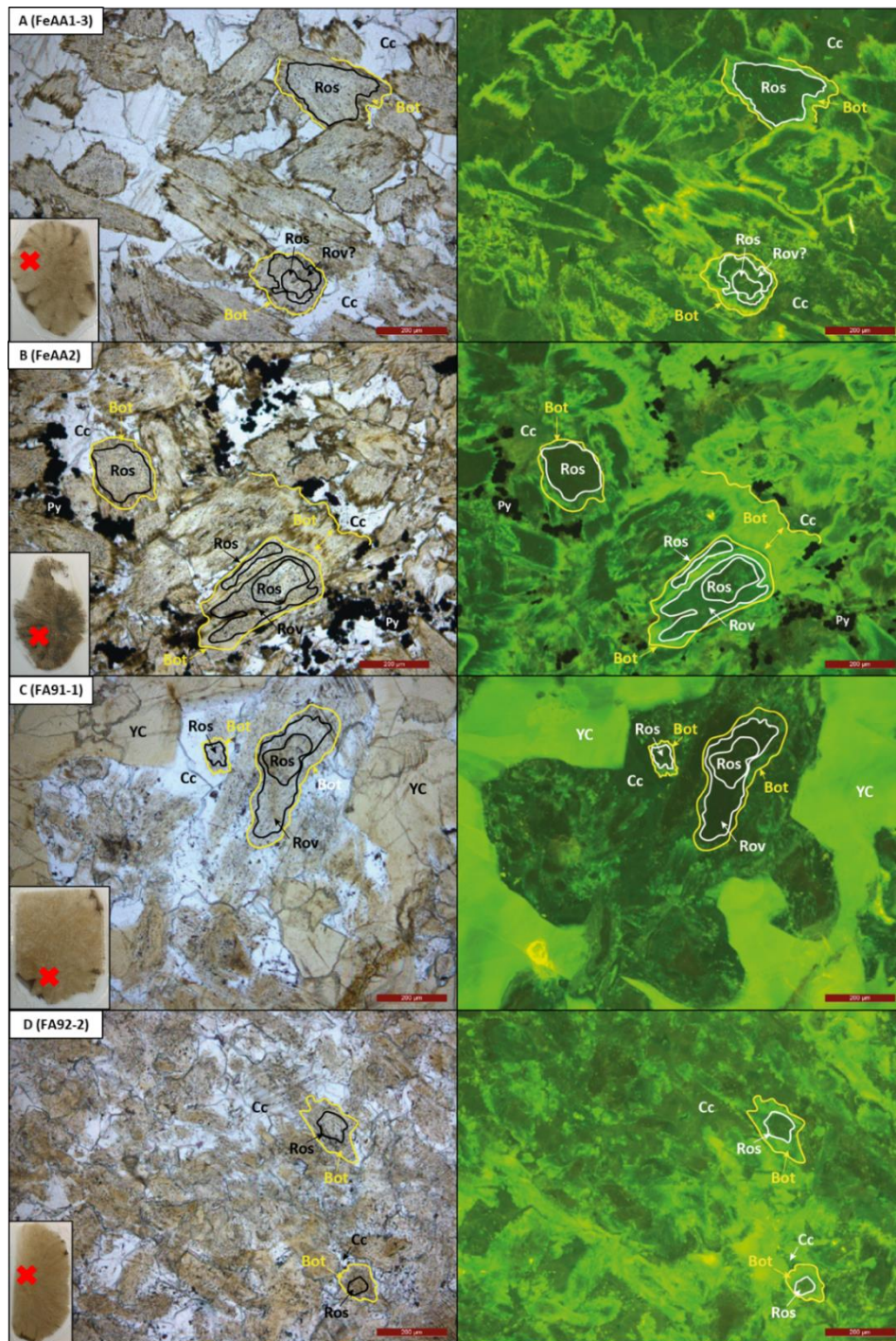
Figure 4.5 – *Microphotographs of thin-sections showing the most prevalent internal structures found within the glendonites from the Aptian-Albian Festningen section (78.09910°N, 13.94257°E). Pictures on the left are optical microscopy images (plane-polarized light) and those on the right are UV fluorescence images (FLUO-Filtertube I3). Each set of images contains the same scale (200 μm; depicted on the bottom right) and their location within the thin-section is indicated by a red cross on the included image. The white outlines show the interpreted extend of the first phase or Ros as well as their overgrowths (Rov), while the yellow outlines mark the interpreted extend of the secondary botryoidal cements (Bot). Cc denotes the third and typically final phase of calcite growth while YC indicates anhedral yellow calcite. Py is pyrite. **(A)** Homogeneous, unzoned glendonite showing a clear distinction between the 3 prevalent carbonate phases and a lack of other components. **(B)** Similar homogeneous, unzoned glendonite, but with more Ros, Rov, and Bot constituents and abundant framboidal pyrite. **(C)** Homogenous and unzoned glendonite with a less clear distinction between Bot and Cc and bountiful amounts of YC. **(D)** Glendonite with a distinctive outer rim consisting of YC (not shown in picture) and considerably less distinction between the 3 prevalent carbonate phases. See Appendix C1-2 for all obervations.*
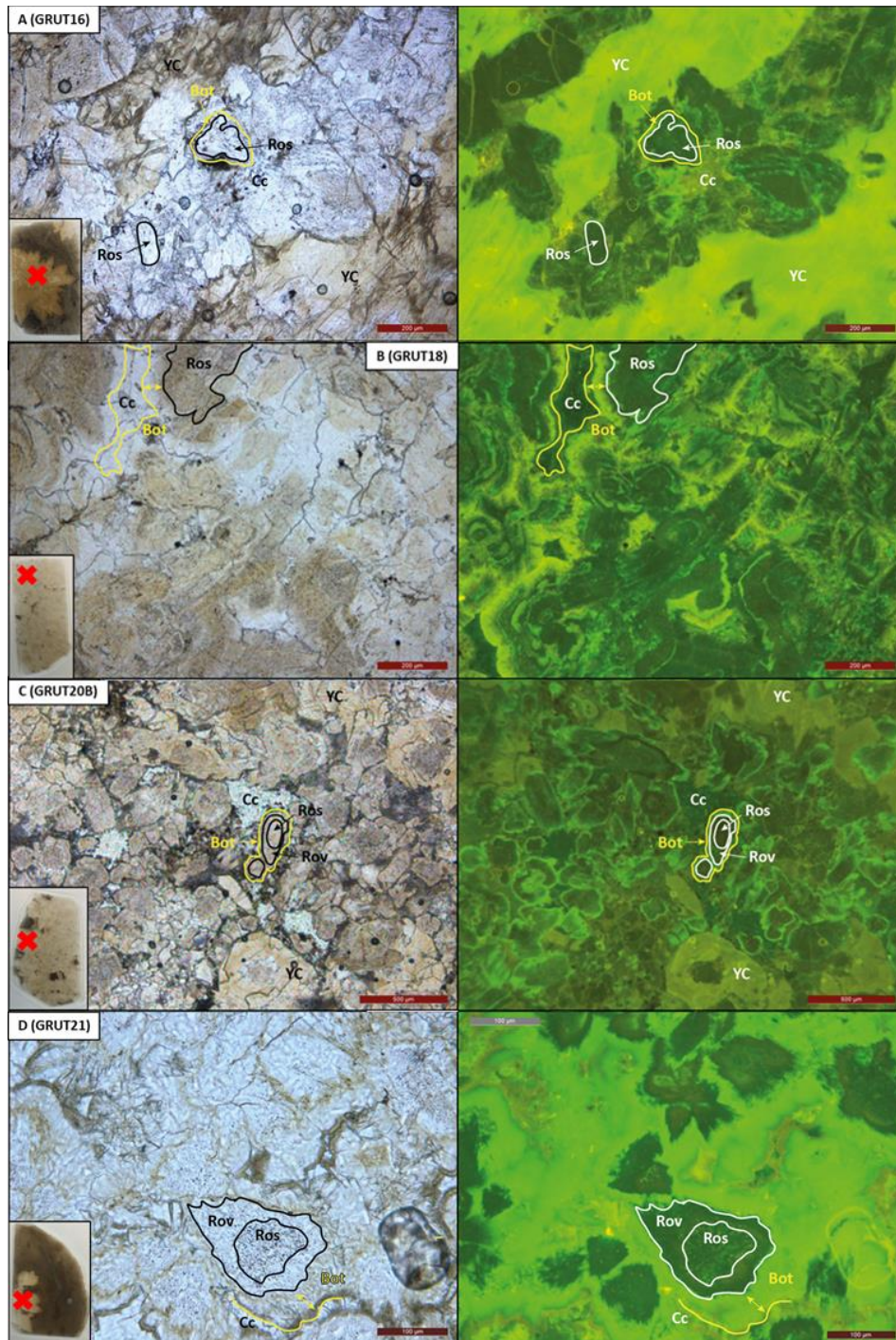
Figure 4.6 - *Microphotographs of thin-sections showing the most distinctive internal structures found within the glendonites from the Grumantbyen section (78.17498°N, 15.10689°E). Pictures on the left are optical microscopy images (plane-polarized light) and those on the right are UV fluorescence images (FLUO-Filtertube I3). Each set of images contains the same scale (depicted on the bottom right), but this scale differs between individual samples (i.e., 100-500 µm). The location of each microphotograph within the thin-section is indicated by a red cross on the included image. The white outlines show the interpreted extend of the first phase or Ros as well as their overgrowths (Rov), while the yellow outlines mark the interpreted extend of the secondary botryoidal cements (Bot). Cc denotes the third and typically final phase of calcite growth while YC indicates anhedral yellow calcite.* **(A)** *Homogeneous and unzoned glendonite with restricted amounts of Bot and bountiful YC, similar to C.* **(B)** *Homogeneous and unzoned glendonite showing more interconnection between Ros and Bot.* **(C)** *Homogeneous and unzoned glendonite with predominately loose Ros/Rov and Bot crystals dispersed between Cc and YC.* **(D)** *Glendonite found within carbonate concretion with distinct Ros and Rov crystals and well-defined/interconnected Bot cements that show the least amount of alteration. See Appendix C1-2 for all obervations.*
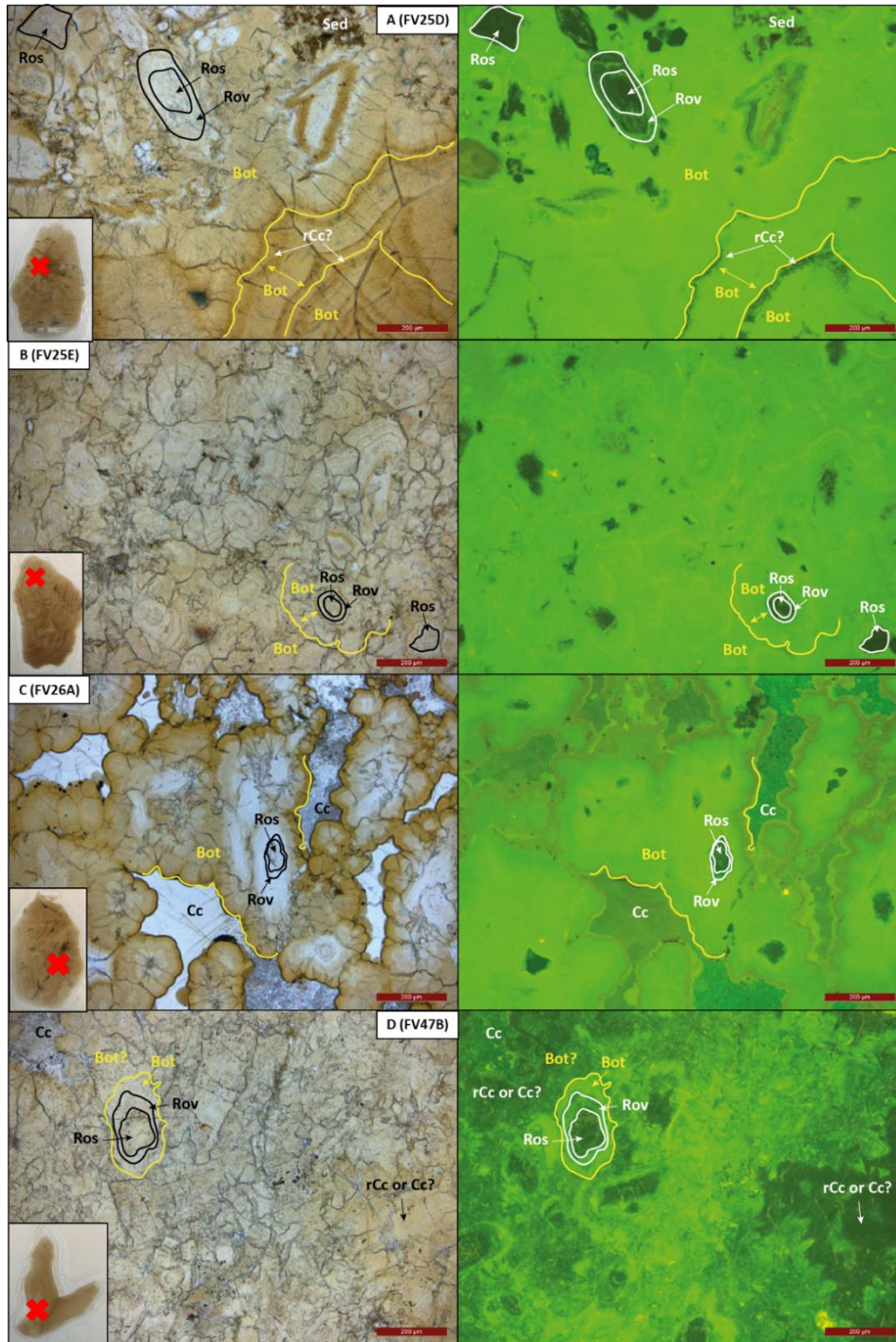
Figure 4.7 - *Microphotographs of thin-sections showing the most prevalent internal structures found within the center of zoned glendonites from the Festningen section (78.09910°N, 13.94257°E). Pictures on the left are optical microscopy images (plane-polarized light) and those on the right are UV fluorescence images (FLUO-Filtertube I3). Each set of images contains the same scale (200 μm; depicted on the bottom right) and their location within the thin-section is indicated by a red cross on the included image. The white outlines show the interpreted extend of the first phase or Ros as well as their overgrowths (Rov), while the yellow outlines mark the interpreted extend of the secondary botryoidal cements (Bot). Cc denotes the third and typically final phase of calcite growth while YC indicates anhedral yellow calcite. rCc stands for calcite cement that has potentially been recrystallized, but its origin remains enigmatic. Sed is sediment. (**A**) Separate Ros (occasionally with Rov) and sediment embedded in a large Bot matrix that is interspaced by small phases of rCc or Cc. (**B**) Smaller separate Ros (occasionally with overgrowths) embedded in Bot. (**C**) Isolated Ros with a more distinct separation of Bot (with dark brown boundary) and Cc (both equant spar as well as microcrystalline) as well as small traces of pyrite. (**D**) Large Ros with some Rov overgrowth enveloped by a Bot phase that seems contaminated and interspaced by either rCc or Cc. See Appendix C1-2 for all obervations.*
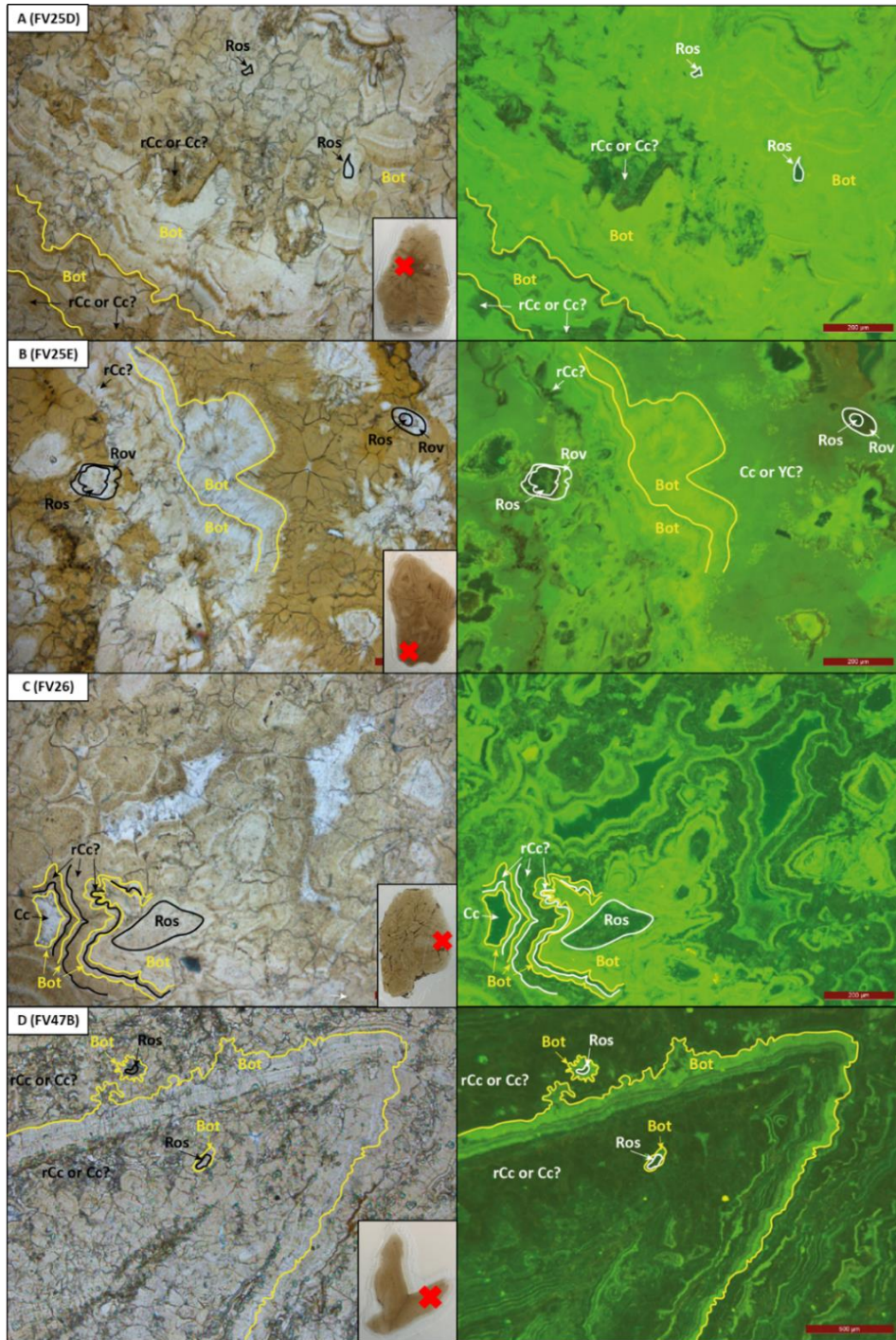
Figure 4.8 - *Microphotographs of thin-sections showing the most prevalent internal structures found within the zonations or the center-zonation transition of zoned glendonites from the Festningen section (78.09910°N, 13.94257°E). Pictures on the left are optical microscopy images (plane-polarized light), and those on the right are UV fluorescence images (FLUO-Filtertube I3). Each set of images contains the same scale (depicted on the bottom right), but this scale differs between individual samples (i.e., 200-500 μm). The location of each microphotograph within the thin-section is indicated by a red cross on the included image. The white outlines show the interpreted extend of the first phase or Ros as well as their overgrowths (Rov), while the yellow outlines mark the interpreted extend of the secondary botryoidal cements (Bot). Cc denotes the third and typically final phase of calcite growth while YC indicates anhedral yellow calcite. rCc stands for calcite cement that has potentially been recrystallized, but its origin remains enigmatic. Sed is sediment. **(A)** Small isolated Ros encompassed by an irregular alternation of Bot and potentially rCc or Cc. **(B)** Ros with Rov overgrowths embedded in a chaotic matrix Bot and potentially rCc or Cc/YC. **(C)** Ros without clear Rov overgrowths surrounded by a distinct alternation of more or less isopachous Bot and potentially rCc or Cc. **(D)** Tip of one of the acinaform glendonites showing small Ros with Bot overgrowths embedded in a zoned matrix consisting of alternations between Bot and potentially rCc or Cc. See Appendix C1-2 for all obervations.*

Beside the 3 prevailing carbonate phases identified in all glendonites from previous studies, numerous cracks and partial or full late diagenetic recrystallization was recognized in all glendonites. This late diagenetic overprint dissolves the borders/textures of the previously deposited carbonate phases and frequently coincides with lamellar twinning within the newly formed crystals (Figure 4.9F). Another prevalent sign of recrystallization is the presence of YC (Figure 4.5C-D, Figure 4.6A, Figure 4.8C) within most specimens. This YC has a distinct amber yellow to dark brown color in PPL that transitions into a pale green color under UV. Event though, this YC seems to preferentially occur around the outer edges of the pseudomorph, filling the pyramidal points, it has also been observed within the center and in between the zonations of the zoned glendonites. The relative contribution of this YC varies greatly with estimations as low as ±5-20% within the zoned glendonites up to ±10-75% for the glendonites from the Dalkjegla Member of the Carolinefjellet Formation (Festningen section) and specific specimens (e.g., GRUT18, GRUT21, and GRUT27) from the Grumantbyen section. The only glendonites that consistently lack this YC are those found within the Innkjegla Member of the Carolinefjellet Formation (Festningen section).

Although pyrite is plentiful within the sediment, which mainly consists of a combination of dark micritic mud and fine quartz sand (average grain-size: ±10-50 μm; sub-rounded and spherical grains) with ample OM, it does not always occur within the glendonites, especially in terms of abundance. While the sediment features small to large patches of anhedral or framboidal pyrite (e.g., Figure 4.9B), the glendonites typically only contain small traces of pyrite that tend to be more euhedral/framboidal and are concentrated within the second and predominantly third paragenetic sequence. In some cases (e.g., FeAA5, FA92-3, GRUT16, GRUT16-1), pyrite is also observed within the *Ros* phase, but this seems to be negligible. The only glendonites in which pyrite forms a major constituent of the pseudomorph (e.g., Figure 4.5B) are those found within the Innkjegla Member of the Carolinefjellet Formation (Festningen section), where it contributes ±10-20%.

Besides pyrite, sediment and quartz grains have also been found to be incorporated around the rims as well as in the center the glendonites (e.g., Figure 4.7A). At the rims, this mainly occurs at areas in between the pyramidal points where the glendonite is broken up, and material was allowed to enter either soon after or during the final stages of consolidation of the pseudomorph. In the case of the center, it seems that the sediment and quartz grains were incorporated early on during either the growth of ikaite crystals or their transformation into anhydrous polymorphs. However, as the rims around the sediment are almost always poorly defined, this could also mean that glendonite structure perpendicular to the surface of the thin-sections is discontinuous in nature.

Although glendonite borders/rims are typically both well-defined and rough (Figure 4.9A-B,E), in most cases it seems that the rims around the outline of the original ikaite crystal tend to be better defined than those found within the center. This has been observed for both the unzoned as well as zoned glendonites. Nonetheless, even the same rim can exhibit considerable variability in terms of its expression, indicating that dissolution and etching are heterogeneous and thus likely to be the result of local phenomena. Some of these phenomena might already occur soon after deposition as multiple dissolution events that have the potential to protrude into the sediments have been found (e.g., Figure 4.9A). Within exclusively the specimen from the Innkjegla Member, the rims that constitute the outline of the original ikaite crystal are heavily recrystallized and transformed into anhedral calcite with a fabric similar to that of *YC*, but a much darker brown color in PPL (Figure

4.9C). As this anhedral calcite shows both similarities as well as clear differences with *YC* and is only found within this specific group of glendonites, it remains unclear whether they were formed by the same or similar processes.

Altogether, there seem to be different categories of centers that can been recognized: (1) a center with small to large *Ros* crystals (sometimes with *Rov* overgrowths) that tend to be isolated and are enveloped by a large matrix of relatively homogeneous *Bot* overgrowths, with a light to dark brown color, and a lack of white *Cc* (Figure 4.7A-B); (2) a center with similar isolated *Ros* crystals (sometimes with *Rov* overgrowths) and *Bot* overgrowths, but also contains white *Cc* with both a microcrystalline as well as an equant spar fabric (Figure 4.7C); and (3) a very chaotic center where isolated *Ros* crystals (with *Rov* and *Bot* overgrowths) are embedded in a matrix that seems to be a combination of *Bot* overgrowth, *rCc*, and *Cc* (Figure 4.7D). This first type of center seems to yield similar zonations that consist of isolated Ros crystals (sometimes with *Rov* overgrowths) within alternations of potentially *rCc*, *Cc*, or *YC* with *Bot* overgrowths (Figure 4.8A-B). The second type of center shows a much more well-defined zonation pattern, similar to the structure observed in certain unzoned glendonites (Figure 4.6B), that seems to consist of several alternations between *Bot* overgrowths and potentially *rCc* as well as some remaining pore space filled with white *Cc*. The third chaotic center with large amounts of apparent *rCC* or *Cc* is the only category that produces zonations that resemble the center.
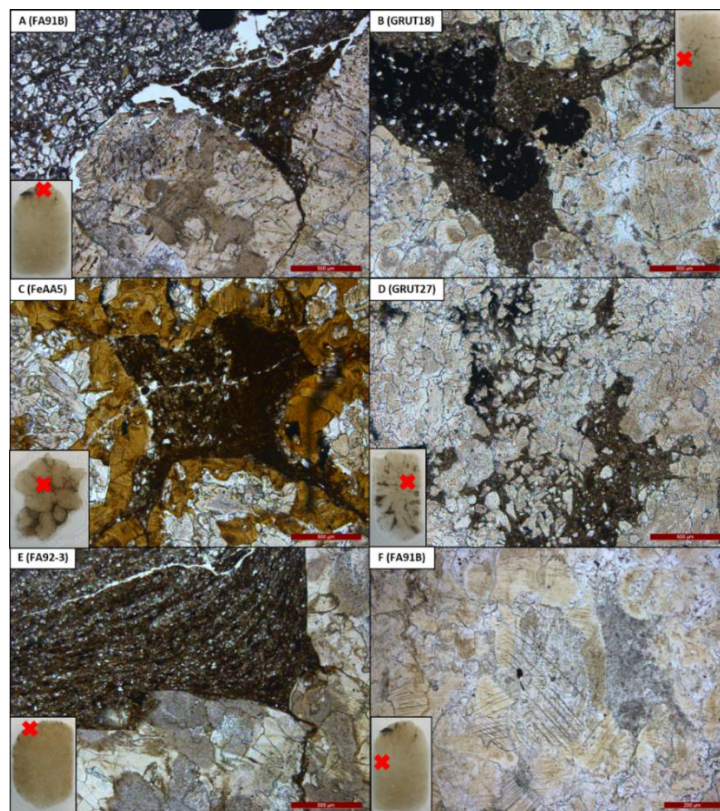
Figure 4.9 - *Microphotographs of thin-sections that highlight the differences in the morphology of the glendonite rims as well as showcasing the sediment and other depositional characteristics. The pictures are optical microscopy images (plane-polarized light) whose scale (depicted in the bottom right) is the same with exception of F. The location of each picture within the thin-section is indicated by a red cross on the included image.* **(A)** *Pyramidal point consisting predominately of YC that is affected by a dissolution event.* **(B)** *Rough and well-defined glendonite rims combined with large anhedral patches of pyrite within the sediment.* **(C)** *An uncommon, but distinct alteration only found at the rims of the glendonites from the Innkjegla Member of the Carolinefjellet Formation (Festningen section).* **(D)** *Broken-up internal glendonite rim.* **(E)** *Draping of sediment around a pretty well-defined rim.* **(F)** *Recrystallization and late diagenetic overprint combined with lamellar twinning. See Appendix C1-2 for all obervations.*

4.2.1. Structural glendonite groups

Using the aforementioned observations and patterns found in the internal structure, the glendonites from this study were categorized into 5 different groups, of which 3 were given subgroups (Table 4-1). Within this framework, Group 1-3 consist of unzoned glendonites, the potential Group 4 of unzoned/zoned glendonites, and Group 5 of zoned glendonites. To show how these groups relate to or are different from each other, the common characteristics of each group will be discussed below.

Group 1a and 1b (Table 4-1) consist of unzoned glendonites (from 0.4-0.8 cm to 2.0 x 2.5 cm) with predominately distinctive cores/rims. Internally, these glendonites contain brownish *Ros* crystals (Ø 15 µm to 265 x 1176 µm; ±30-55% of the total volume) that typically lack *Rov* overgrowths and have a thin acicular to fibrous dark brown *Bot* overgrowths (2-70 µm thick; ±5-20% of total volume) with mostly an isopachous nature (e.g., D). What is especially pronounced in this group of glendonites is the distinctly larger pore space (±25-60% of total volume) compared to the specimens from the other groups, where it only tends to be a minor component (±5-45%). Despite being much more extensive, the pore space within these specimens is still filled with the same kind of clear sparite *Cc*. While the glendonites from both 1a and 1b are quite similar in internal structure, subgroups were established to differentiate between samples that contained abundant pyrite (i.e., Group 1b; Figure 4.5B) and those that did not (i.e., Group 1a; Figure 4.5A).

The glendonites from Group 2 (Table 4-1) consist of slightly larger unzoned glendonites (from 1.4-1.6 cm to 2.1 x 4.8 cm), which internally exhibit transparent/grey to brown *Ros* crystals (Ø 15 µm to 400 x 400 µm; ±10-35% of total volume) that either lack or contain *Rov* overgrowths (Figure 4.5C and Figure 4.6A). These *Ros* crystals are surrounded by thin fibrous *Bot* overgrowths (0-100 µm thick; ±5-35% of total volume) with a transparent/grey to light brown color and distinct light amber yellow to dark brown discontinuity horizons. Pore space constitutes ±10-45% and is filled by anhedral to microcrystalline *Cc* with a transparent and occasionally pale amber yellow color in PPL and a brown to dark or green color under UV. The most striking characteristic of this group is the fact that all of the previously mentioned *Ros/Rov*, *Bot*, and *Cc* phases are enclosed by large amounts of *YC* (±25-70% of total volume) that is associated with recrystallization. While the internal structure of the glendonites from Group 2a and 2b are similar in terms of components, the specimen from Group 2b tend to show thicker *Bot* overgrowths and by YC with a considerably less uniform and more fragmented fabric (Table 4-1).
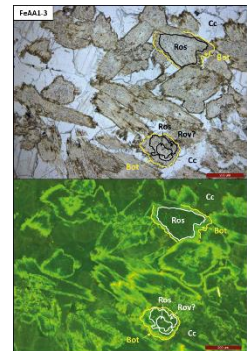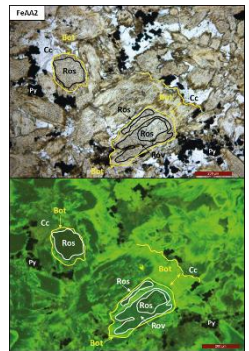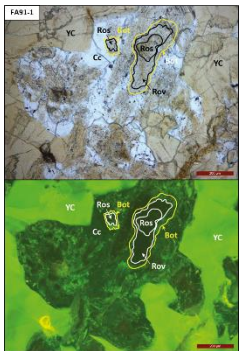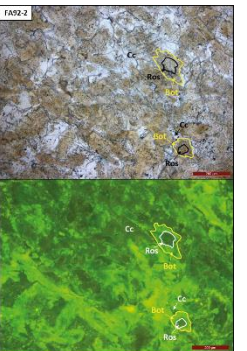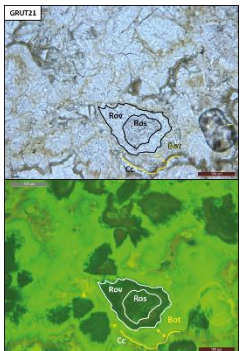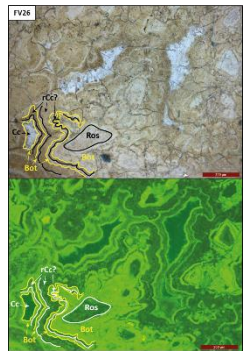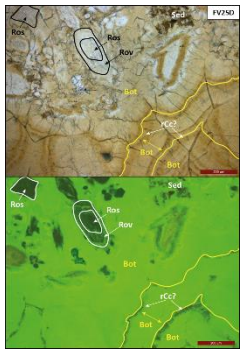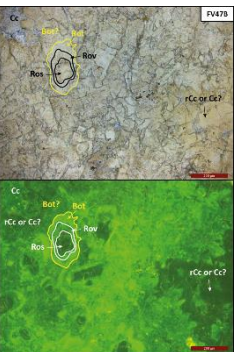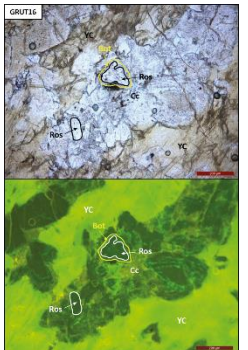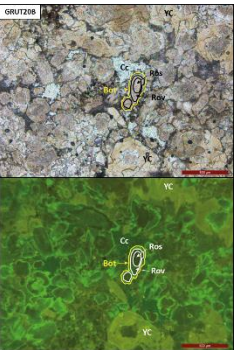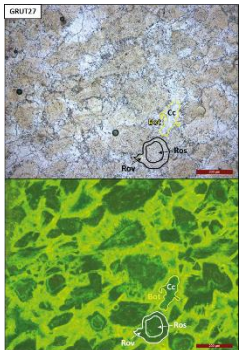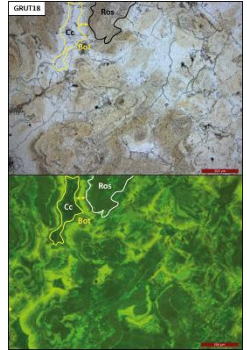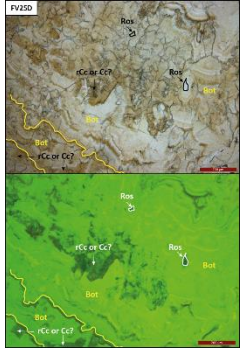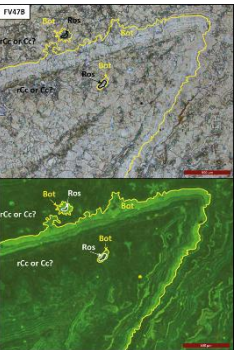
Group 3 (Table 4-1) consists of a larger glendonite (4.3 x 6.5 cm; Figure 4.3E and Figure 4.9D) and a glendonite found in a carbonate concretion (2.2 x 2.5 cm; Figure 4.3C-D and Figure 4.6D). Both of these glendonites are unzoned and exhibit an internal structure that is most reminiscent of the best-preserved specimens (e.g., Figure 3.7C) from the Early Jurassic to Early Cretaceous strata of Siberia reported by Morales et al. (2017a). Typical features of these specimens are well-defined *Ros* crystals with clear *Rov* overgrowths overgrown by thick and interconnected *Bot* overgrowths (containing a light brown, clear, and dark brown discontinuity horizons) as well as minor amounts of pore space (Morales et al., 2017a). In this study, the *Ros* crystals (Ø 15 µm to 230 x 400 µm; ±40% of total volume) are transparent/grey or light amber brown in PPL (amber brown or greenish to dark under UV) and have distinct *Rov* overgrowths. The *Bot* overgrowths (10-75 µm thick; ±50% of total volume) are interconnected in both cases, but in the larger glendonite, it has a more fibrous texture and lacks clear light to dark brown discontinuity horizons. The

minor amount of pore space (±5-10% of total volume) is occupied by clear whitish *Cc* (light yellow/greenish to dark under UV) with sparite-like fabric.

Group 4 (Table 4-1) consists of 2 glendonites, of which, GRUT18 (Figure 4.6B) is unzoned and FV26 (Figure 4.8C) is zoned, that show unique *Bot* structures (25-100 µm thick; ±45-80% of total volume), with fibrous to botryoidal fabrics and less well-defined zonations, that are not readily identified within the other groups. The color of these Bot phases ranges from transparent to light amber yellow and brown in PPL (pale greenish yellow to bright green under UV). Unfortunately, the other features of these glendonites are not as analogous. The *Ros* crystals (Ø 35 µm to 120 x 240 µm) have a similar sub-rounded to rosette-like shape with a transparent to light amber yellow color in PPL (dark with light greenish spots under UV) and contain organic impurities. However, their respective volume is drastically different (±10% of total volume for FV26 compared to ±50% for GRUT18). The *Cc* (±5-10% of total volume) that fills the pore space in both specimens appears anhedral and tends not to be well-defined. It mostly has a transparent/grey color in PPL (dark green to dark under UV) and, in contrast to GRUT18, is almost exclusively found in the center and zonations of FV26.

Categorizing the macro-zoned glendonites proved to be more difficult as their centers and zonations often did not resemble each other in individual specimens as well as between different glendonites (c.f., Figure 4.7 and Figure 4.8). Ultimately, the best way to differentiate them appeared to be whether they *Bot* or *Cc/rCC* phases were predominant components in their centers and especially their zonations. Visually, these differences are most clear under UV as the *Bot* phases are associated with bright green colors (indicative of higher organic content), while the *Cc/rCC* are essentially dark (Table 4-1). Within the zoned glendonites, Group 5a (Table 4-1) represents the specimens that contain predominately *Bot* phases. These glendonites consist predominantly of small aggregate of crystals to small stellate pseudomorphs (0.9 x 1.1 cm to 1.7 x 1.8 cm) that have sub-rounded to rosette-like or lath-shaped *Ros* crystals (Ø 25 µm to Ø 170 µm; ±5-10% of total volume) that tend to be isolated and contain some organic impurities. The *Bot* overgrowths (5-100 µm thick; ±75-85% of total volume) tend to have an acicular to fibrous fabric and a transparent/grey to light amber yellow or brown color in PPL (bright green to dark under UV). These overgrowths also exhibit distinct zonations and are occasionally interspersed by *YC*. If present, pore space filled by anhedral *Cc* (±5-10% of total volume) with a transparent/grey color in PPL (dark with brown spots under UV) is found almost exclusively within the centers. *YC* is present in small amounts (±5-20% of total volume) and situated in between the *Bot* overgrowths. Alternatively, the zoned glendonites from Group 5b (Table 4-1) consist of small double acinaforms or small aggregate of crystals (0.9 x 1.6 cm) with a predominance in *Cc/rCc* phases. The *Ros* crystals (Ø 20 µm to 80 x 300 µm; ±5-15% of total volume) within these glendonites are mostly sub-rounded to lath-shaped, contain fewer organic impurities than those in other groups, and are typically not internally zoned. Their color is transparent/grey to mostly dark amber yellow in PPL and dark with brown tints under UV. These crystals sit in a messy matrix of *Cc/rCc* phases (±75-80% of total volume) that have a very irregular fabric that prevents quantification of their size. Similar to most other phases, their color is transparent/grey to light amber yellow in PPL and mainly dark with some shades of green under UV. No pore space and thus *Cc* was observed within this group.

Table 4-1 – *Glendonite groups based upon the prevalent inner structures. Group 1a and 1b consists of glendonites with brown Ros crystals that typically lack Rov overgrowths and are enveloped by a thin Bot phase (only the late stage dark brown rim). The pore space of these glendonites, which is larger than those found in other groups, is filled by clear Cc that either lacks or contains abundant pyrite. Group 2a consists of glendonites with clear to brown Ros crystals (with or without Rov overgrowths) that are surrounded by a thin Bot phase (only the clear early stage) and minor amount of clear Cc that occupies the pore space. All these carbonate phases are enclosed by large amounts of YC indicative of recrystallization. The glendonites in group 2b are similar to those in group 2b, but are less enclosed by the YC and occasionally show thicker Bot phases. The internal structure found within group 3, considered to be ideal example of a well-preserved specimen, is characterized by typically large Ros crystals (and Rov overgrowths) overgrown by thick and interconnected Bot phases (containing a light brown, clear, and dark brown zone). The small amount of remaining pore space is occupied by clear calcite cement. The glendonites in Group 4 show structures that are not readily identified in the other groups, but as other similarities beside these structures are lacking it these specimens could also be categorized into other groups: FV26 could belong to Group 5b and GRUT18 to potentially Group 3. Group 5a and 5b represent the macro-zoned glendonites that are subdivided based upon having Bot phases or rCc/Cc as the predominant component of the centers and especially the zonations.*

Unzoned						Zoned	
Group 1a (unzoned)	Group 1b (unzoned)	Group 2a (unzoned)	Group 2b (unzoned)	Group 3 (unzoned)	Group 4? (zoned/unzoned)	Group 5a (zoned)	Group 5b (zoned)

Sample ID	δ¹⁸O	δ¹³C	Sample ID	δ¹⁸O	δ¹³C	Sample ID	δ¹⁸O	δ¹³C	Sample ID	δ¹⁸O	δ¹³C	Sample ID	δ¹⁸O	δ¹³C	Sample ID	δ¹⁸O	δ¹³C	Sample ID	δ¹⁸O	δ¹³C	Sample ID	δ¹⁸O	δ¹³C
FeAA1-2	-5.29	-14.53	FeAA1-1	-6.15	-12.26	FeAA9	-7.03	-17.87	FA92-2	-8.74	-16.31	GRUT21	-2.25	-29.20	FV26	-5.58	-21.41	FeVH2?	-10.28	-18.41	FV23	-13.61	-10.47
FeAA1-3			FeAA2	-5.43	-14.55	FA91-1				-5.96	-18.54	GRUT27	-4.57	-17.43		-3.07	-22.07		-11.02	-17.68	FV47B	-11.41	-15.44
FeAA1-4			FeAA2-2	-3.87	-15.30	FA91-2	-6.13	-18.93	GRUT20B	-7.08	-23.41				GRUT18	-5.53	-11.25	FV24A	-3.28	-23.50		-12.53	-10.21
FeAA5	-6.35	-18.22				FA91A	-6.72	-17.23												-1.98	-24.14		-13.32	-10.79
						FA91A-2	-6.72	-17.23										FV24B	-3.28	-23.50			
						FA91B													-1.98	-24.14			
						FA92-1	-6.50	-18.43										FV25D	-3.19	-24.42			
						FA92-3													-3.41	-24.31			
						FA92-4												FV25E	-5.87	-22.64			
						FA93	-6.32	-19.30											-2.77	-23.90			
						FA93-2												FV26A	-1.95	-23.22			
						GRUT16	-10.20	-23.41											-3.57	-21.58			

44

4.3. Bulk stable isotope data

When $\delta^{18}O_{carb}$ is plotted against $\delta^{13}C_{carb}$, the bulk stable isotopic data from all glendonites is characterized by a general inverse correlation (Figure 4.10) with various mixing lines that seem to be related both their area of formation and their respective age. Overall, the glendonite with the most negative $\delta^{13}C_{carb}$ value (-29.20‰) was GRUT21, a glendonite found in the horizon at 13.0 m in the Grumantbyen section (Figure 4.1, Figure 4.11); whereas the most positive $\delta^{13}C_{carb}$ value (-9.16‰) corresponds to GRUT16, a glendonite from the horizon found at 20.5 m in the same section (Figure 4.1, Figure 4.11). On average, the $\delta^{13}C_{carb}$ value for all glendonites was calculated to equal a value of -18.34‰. Similarly, the most negative $\delta^{18}O_{carb}$ value (-14.23‰) belongs to FV23D, a glendonite from the horizon situated at 561 m in the Festningen section (Figure 4.1, Figure 4.11); while the most positive $\delta^{18}O_{carb}$ value (-1.95‰) corresponds to FV26A, a glendonite from the horizon found at 554 m in the same part of the Festningen section (Figure 4.1, Figure 4.11). The calculated average $\delta^{18}O_{carb}$ for all glendonites equals -6.90‰.
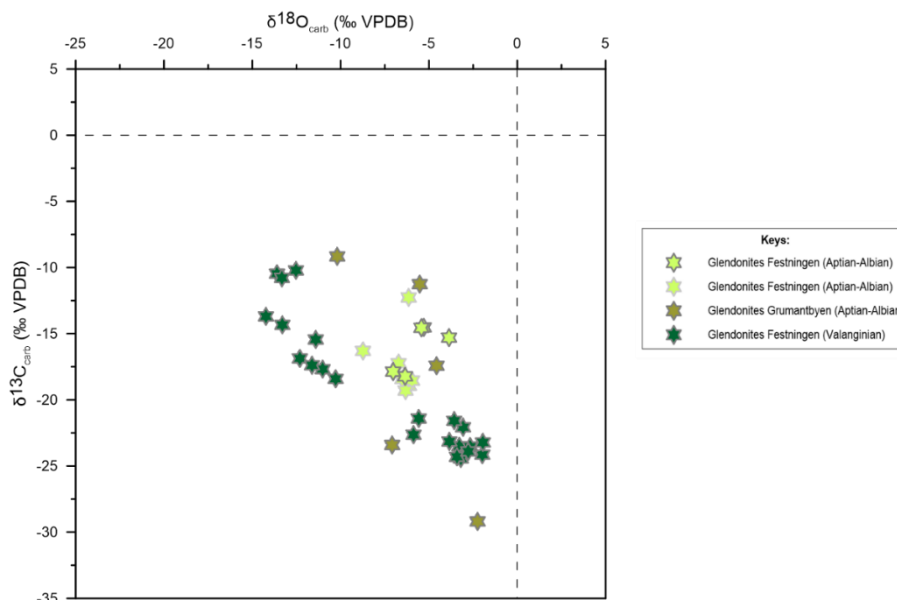
Figure 4.10 - *The $\delta^{18}O_{carb}$ plotted against $\delta^{13}C_{carb}$ from glendonites of the Festningen section (78.09910°N, 13.94257°E; green stars) and Grumantbyen section (78.17498°N, 15.10689°E; olive stars). Glendonites from the Festningen Section are subdivided into dark and light green stars, where dark green stars indicate the macro-zoned glendonites found in the Valanginian-Hauterivian Kikutodden Member (Rurikfjellet Formation) and light green stars refers to the unzoned glendonites found in the Aptian-Albian Dalkjegla/Innkjegla Member (Carolinefjellet Formation). The colored borders around the stars are indicative of the respective host lithology as documented in Figure 4.1 and Appendix A. In this particular case, dark grey represents siltstone and light grey refers to fine sandstone. For sample names, their specific isotope values and other related information, please refer to sample lists (Appendix B1).*

Figure 4.11 - The δ13Ccarb and δ18Ocarb from glendonites of the Festningen section (left; 78.09910°N, 13.94257°E) and Grumantbyen section (right; 78.17498°N, 15.10689°E) plotted against their respective stratigraphic height (in meters). The red dashed lines constitute an abridged version of the correlation between both sections as proposed in Figure 4.1. Explanations for the symbols used within the isotopic plots as well as the stratigraphy can be found within the provided legends. For sample names, their specific isotope values and other related information, please refer to sample lists in the Appendix B1.

When examined in more detail, the bulk isotopic data shows that the glendonites from the Grumantbyen section exhibit the widest spread and highest variability in terms of $\delta^{13}C_{carb}$ (20.04‰, from -29.20 to -9.16‰) and moderate spread in $\delta^{18}O_{carb}$ (7.95‰, from -10.20 to -2.25‰) (Figure 4.10). This appears counterintuitive as these horizons are the most closely interspaced, but could be a result of their richness in specimens (Figure 4.1, Figure 4.11). Interestingly, the opposite seems to be true for the glendonites from the Festningen section, where both the glendonites from the Aptian-Albian (light green stars) and those from the Valanginian-Hauterivian (dark green stars) each form roughly 2 distinct clusters (Figure 4.10). The largest variability in $\delta^{18}O_{carb}$ (12.28‰, from -14.23 to -1.95‰) is exhibited by the glendonites from the Valanginian-Hauterivian Rurikfjellet Formation at the Festningen section (Figure 4.10). The glendonites with the least amount of spread, in terms of both $\delta^{13}C_{carb}$ (7.04‰, from -19.30 to -12.26‰) as well as $\delta^{18}O_{carb}$ (4.87‰, from -8.74 to -3.87‰) are those from Aptian-Albian Carolinefjellet Formation at the same Festningen section (Figure 4.10). While the appearance of these clusters seems quite evident, it is important to mention that certain glendonites are measured multiple times and could thus be responsible for a bias within these results (Appendix B1).

Aside from the Aptian-Albian glendonites from the Festningen section (light green stars), each of the aforementioned clusters seems to also adhere to the general inverse correlation internally (Figure 4.10). These negative linear correlations produce an R^2 that ranges from 0.49-0.87, where the lowest value coincides with only the glendonites from the Grumantbyen section and the highest value is attained when only the Valanginian-Hauterivian glendonites from the Festningen section are considered. Together, all glendonites yield an R^2 of 0.51, suggesting a moderate linear relationship.
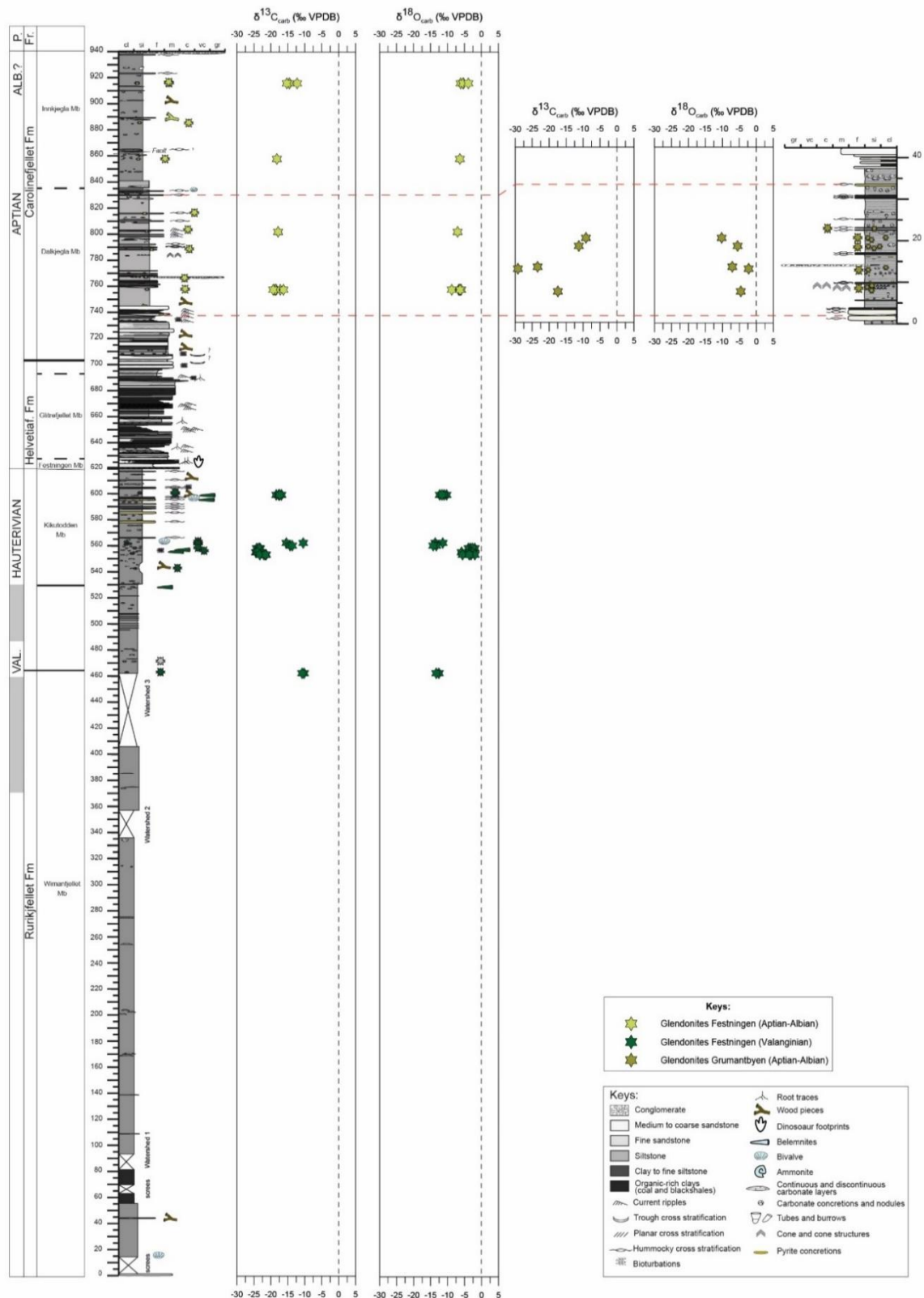
Beside these co-variant trends in $\delta^{13}C_{carb}$ and $\delta^{18}O_{carb}$, there does not seem to be any trend between isotopic values and the type of host lithology as most glendonites were found in siltstone (dark grey) and the ones that originated in fine sandstone (light grey) belong to the glendonite cluster with the least amount of spread (Figure 4.10). The only feature that somewhat stands out is the minor trend towards more positive values in both $\delta^{13}C_{carb}$ and $\delta^{18}O_{carb}$ that can be observed in the Festningen section (Figure 4.11). Although this trend appears to be absent in the Grumantbyen section, it is impossible to confirm this with the current amount of measurements as well as the supposed lack of a depositional equivalent to the Innkjegla Member (Figure 4.11; Appendix B1).

In general, the diagenetic features, sediments, conglomerates, limestones, and belemnites of both the Festningen and Grumantbyen sections exhibit an isotopic composition that is more or less similar in terms of $\delta^{18}O_{carb}$, but more positive in $\delta^{13}C_{carb}$ (Figure 4.12). With the exception of the belemnites, a similar although less evident inverse correlation could be observed when looking at all data together. However, as this correlation is not as clear as the one seen within the glendonites and appears to be absent when looking at individual categories (e.g., only sediments), it cannot be firmly established. While most specimen from each category plot quite close together, a larger variability in terms of $\delta^{13}C_{carb}$ (15.42‰, from -18.49 to -3.07‰) for the tubes and $\delta^{13}C_{carb}$ (12.00‰, from -18.81 to -5.82‰) as well as $\delta^{18}O_{carb}$ (10.83‰, from -15.09 to -4.27‰) for the concretions from the Festningen section can be found (Figure 4.12). Despite this large variability in composition, their average $\delta^{13}C_{carb}$ (-12.64‰ for tubes; -10.71‰ for concretions) and $\delta^{18}O_{carb}$ (-7.19‰ for tubes; -8.43 ‰ for concretions) are actually quite similar. The specimens with the most positive $\delta^{13}C_{carb}$ and the most negative $\delta^{18}O_{carb}$ are the conglomerates, which showed an average $\delta^{13}C_{carb}$ of -7.63‰ (ranging from -9.71 to -

4.73‰) an average $\delta^{18}O_{carb}$ of -17.48 (ranging from -19.90 to -14.71‰) (Figure 4.12). The limestones plot close to the conglomerates with an average $\delta^{13}C_{carb}$ of -5.58‰ (ranging from -6.58 to -4.57‰), but are slightly less negative in terms of $\delta^{18}O_{carb}$ (average: -14.03‰, ranging from -14.76 to -13.30‰). The $\delta^{13}C_{carb}$ and $\delta^{18}O_{carb}$ values for cone-in-cone structures ($\delta^{13}C_{carb}$ = -5.89‰; $\delta^{18}O_{carb}$ = -11.08‰) and wood samples ($\delta^{13}C_{carb}$ = -6.76‰; $\delta^{18}O_{carb}$ = -8.24‰), appear to be closest to that of the sediment, which had an average $\delta^{13}C_{carb}$ of -7.37‰ (ranging from -12.30 to -2.33‰) and $\delta^{18}O_{carb}$ of -11.44‰ (ranging from -13.09 to -9.75‰). Both the nodules from the Festningen section and especially the cannonball concretion from the Grumantbyen section show the most negative $\delta^{13}C_{carb}$ values (-18.17 and -29.20‰ respectively) as well as the least negative $\delta^{18}O_{carb}$ values (-4.48 and -3.71‰ respectively) (Figure 4.12). Finally, the belemnites from the Valanginian-Hauterivian Rurikfjellet Formation plotted around the reference value with an average $\delta^{13}C_{carb}$ of 0.55‰ (ranging from -0.06 to 2.10‰) and $\delta^{18}O_{carb}$ of -0.75‰ (ranging from -1.66 to 0.35‰) (Figure 4.12).

Looking beyond the scope of co-variant trends in $\delta^{13}C_{carb}$ and $\delta^{18}O_{carb}$, it can be said that, although a clear stratigraphical trend is absent, most diagenetic features are preferentially formed within specific lithologies (c.f., Figure 4.12 and Figure 4.13). This trend can be identified most clearly within the concretions. Unfortunately, the diagenetic features found within the Kikutodden Member of the Valanginian-Hauterivian Rurikfjellet Formation have not been analyzed and it is therefore unknown whether these specimens have a composition that is similar to the diagenetic features found within the Carolinefjellet Formation or that they more closely resemble those of the belemnites. Nevertheless, the fact that the isotopic composition of the belemnites plots close to the reference value seems to suggest that the specimens from at least Valanginian-Hauterivian part of the Festningen section have been preserved quite well.
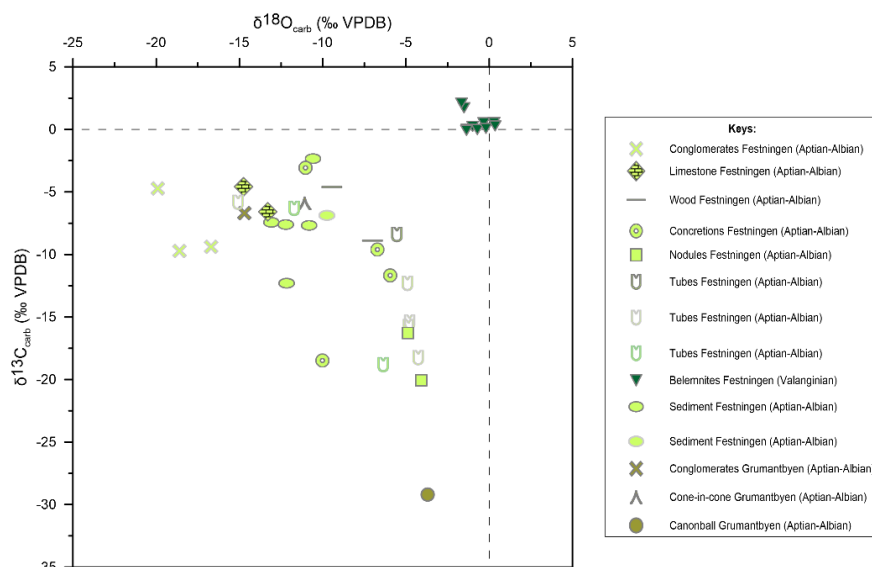
Figure 4.12 - *The $\delta^{18}O_{carb}$ plotted against $\delta^{13}C_{carb}$ from diagenetic features, sediments, conglomerates, limestones, and belemnites of the Festningen section (78.09910°N, 13.94257°E; green symbols) and diagenetic features of Grumantbyen section (78.17498°N, 15.10689°E; olive symbols). The symbols for the Festningen section are subdivided into dark and light green symbols based on whether they are part of the Valanginian-Hauterivian Kikutodden Member (Rurikfjellet Formation) or the Aptian-Albian Dalkjegla/Innkjegla Member (Carolinefjellet Formation). The colored borders around the symbols are indicative of the respective host lithology as documented in Figure 4.1 and Appendix A.. In this case, dark grey represents siltstone, light grey refers to fine sandstone, and green indicates an unknown origin. For sample names, their specific isotope values and other related information, please refer to sample lists (Appendix B2).*
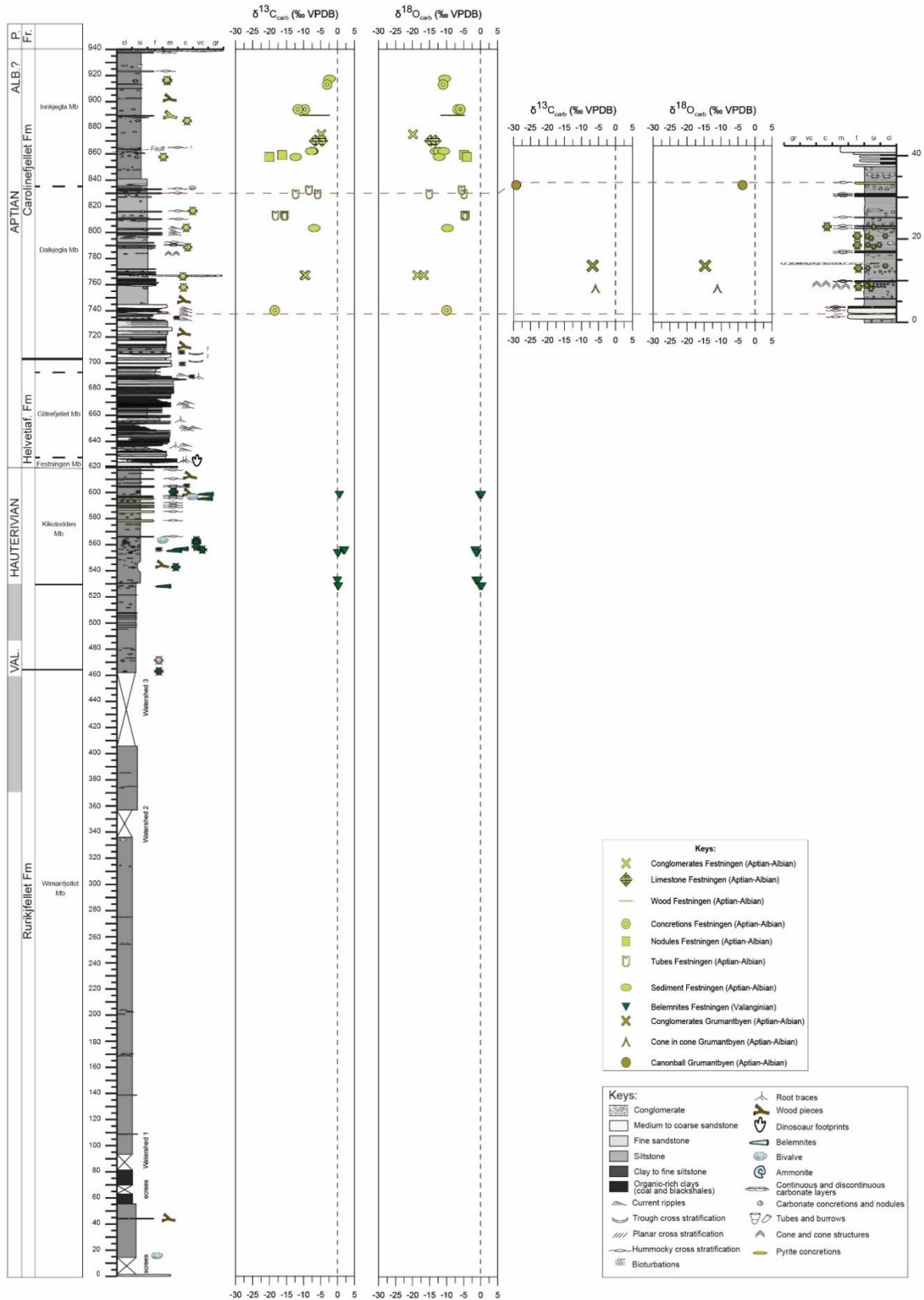
Figure 4.13 - The $\delta^{13}C_{carb}$ and $\delta^{18}O_{carb}$ from diagenetic features, sediments and belemnites of the Festningen section (left; 78.09910°N, 13.94257°E) and Grumantbyen section (right; 78.17498°N, 15.10689°E) plotted against their respective stratigraphic height (in meters). The red dashed lines contitute an abridged version of the correlation between both sections as proposed in Figure 4.1. Explanations for the symbols used within the isotopic plots as well as the stratigraphy can be found within the provided legends. For sample names, their specific isotope values and other related information, please refer to sample lists in the Appendix B2.

49

4.3.1. Internal structure and stable isotopic composition

When the previously described structural glendonite groups (Table 4-1) are compared with their respective stable isotopic measurements, it becomes apparent that with these results, the bulk isotopic composition is not a clear predictor of the internal structure or expression of the carbonate phases (Figure 4.14). This finding is somewhat puzzling as glendonites from various ages and locations do show clear similarities in overall cementation patterns (i.e., Figure 3.7). It should, however, be noted that, in hindsight, using the micro-drill to obtain this data is not exactly desirable for answering this kind of research questions and thus limits the veracity of the conclusions drawn here. The main problem being that the thin-sections and isotopic data were obtained from different parts of each specimen. This discrepancy makes it impossible to ensure that the drilled material coincides with the exact location of analyzed carbonate layers, which may have resulted in large artifacts. Fortunately, the veracity of the assumption that the drilled material is representative of the analyzed carbonate layers is somewhat supported by the fact that multiple measurements from the same glendonites (i.e., glendonites from Hauterivian Kikutodden Member) at different locations yielded very similar results in terms of isotopic composition (Appendix B1).
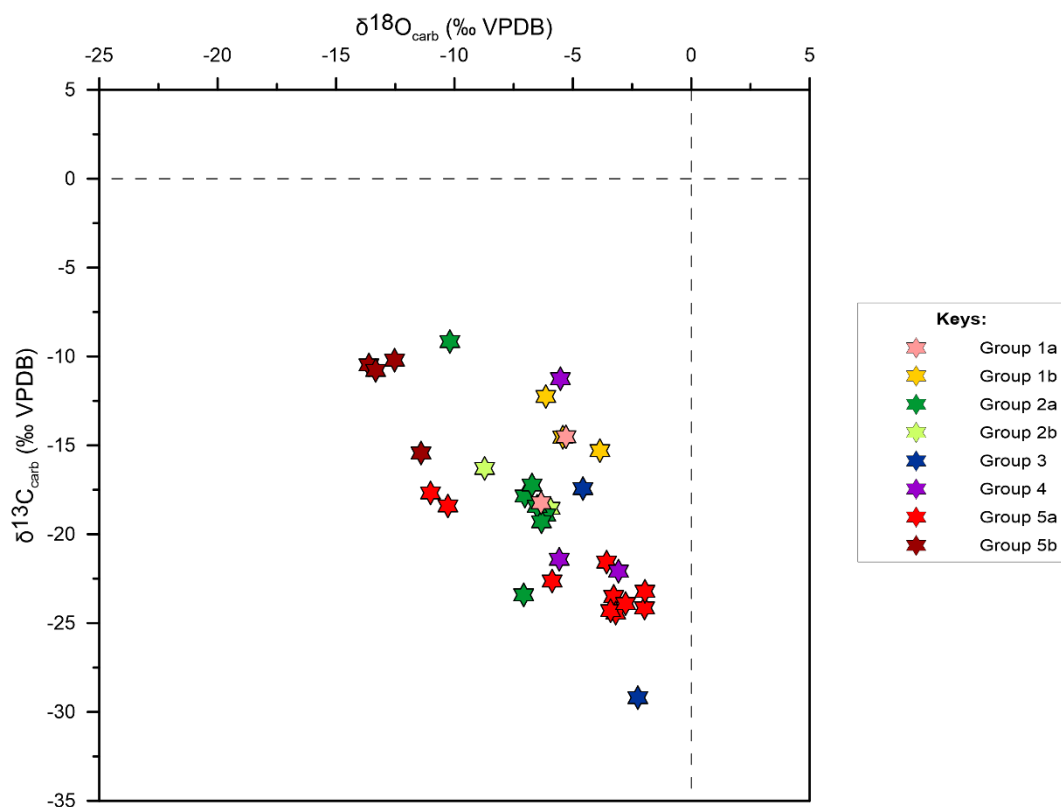
Figure 4.14 - The $\delta^{18}O_{carb}$ plotted against the $\delta^{13}C_{carb}$ from glendonites of the Festningen section (78.09910°N, 13.94257°E) and Grumantbyen section (78.17498°N, 15.10689°E). The glendonites are categorized into groups, as indicated by the different colors, based upon differences and similarities between the carbonate phases as well as their prevalent inner structure (see for visual examples). For sample names, their specific isotope values and other related information, please refer to in conjunction with the sample lists (Appendix B1).
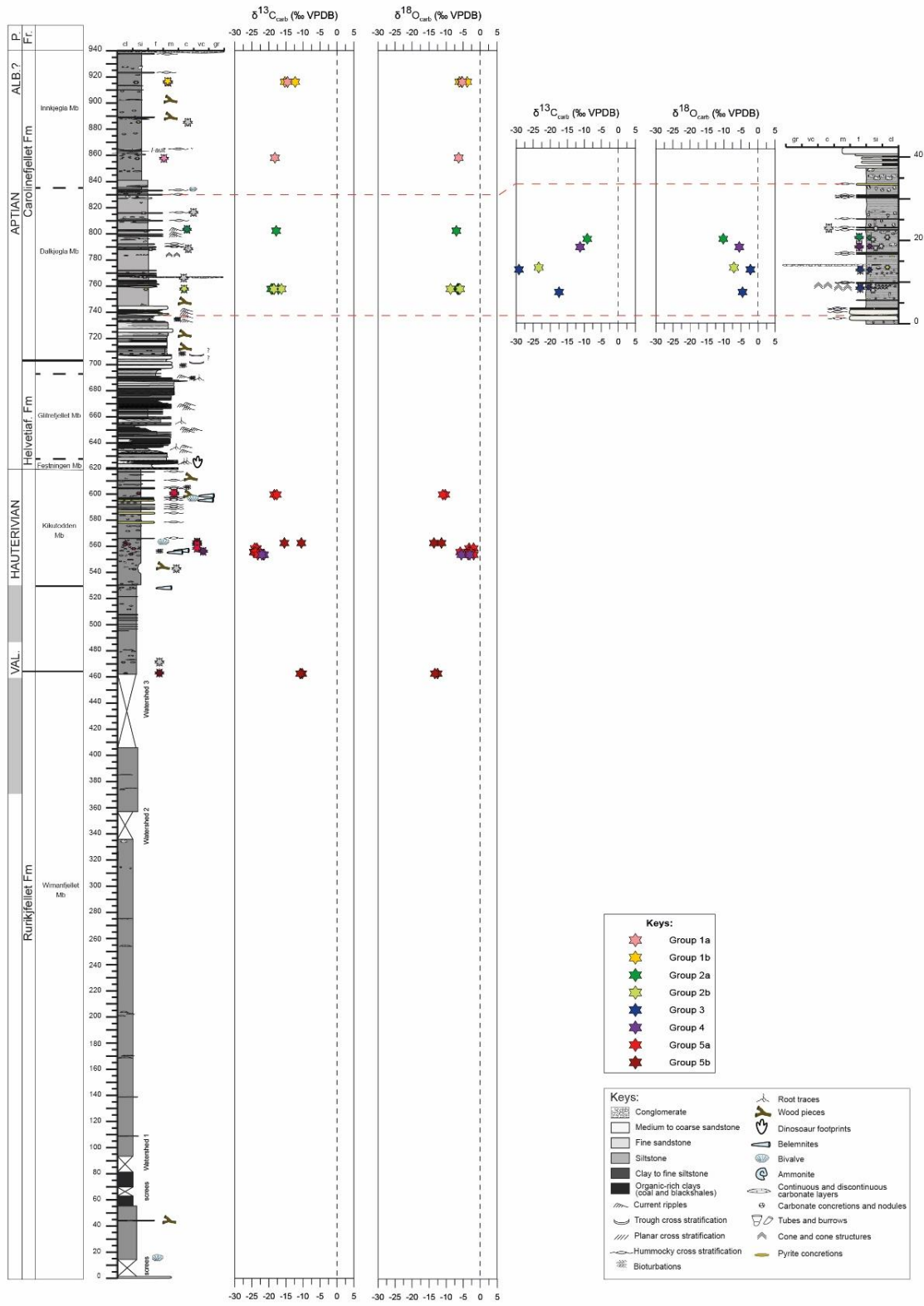
Figure 4.15 - The $\delta^{13}C_{carb}$ and $\delta^{18}O_{carb}$ from glendonites of the Festningen section (left; 78.09910°N, 13.94257°E) and Grumantbyen section (right; 78.17498°N, 15.10689°E) plotted against their respective stratigraphic height (in meters). The glendonites are categorized into groups, as indicated by the different colors, based upon differences and similarities between carbonate phases as well as their prevalent inner structure (see for visual examples). The red dashed lines constitute an abridged version of the correlation between both sections as proposed in Figure 4.1. Explanation for the symbols used within the isotopic plots as well as the stratigraphy can be found within the provided legends. For sample names, their specific isotope values and other related information, please refer to in conjunction with the sample lists (Appendix B1).

Instead of the stable isotopic composition, the respective stratigraphic height and thus the environment or time period in which the glendonite was formed seems to provide a much better explanation for the distribution in the structural glendonite groups that were established in this study (Figure 4.15). This correspondence is even more pronounced when the questionable Group 4 is indeed omitted and FV26 and GRUT18 are reclassified into their other potential groups (Table 4-1). When this change is implemented, each of the structural glendonite groups is characteristic for a specific part of the stratigraphy and the only discrepancy that would need to be explained is the fact that Group 2 and Group 3 somehow occur conjointly within the Grumantbyen section (Figure 4.15). Therefore, together with the previous observations, this indicates that in some, yet to be explained, way either environmental conditions, geochemical parameters, or geological time periods have a paramount influence on the internal structure as well as expression of the carbonate phases. Unfortunately, it proves to be difficult to pinpoint certain structural elements to specific conditions as for example the distinct zoning found within the Valanginian-Hauterivian glendonites of this study is not observed in other glendonites found within the Valanginian strata such as those of Siberia (Kaplan, 1978; Rogov and Zakharov, 2010) and the Sverdrup Basin (Kemper and Schmitz, 1975; Grasby et al., 2017). Additional problems arise when trying to explain the origin of the distinct *YC* that constitutes a major part of the total volume in glendonites from the Aptian Dalkjegla Member (Carolinefjellet Formation) as well as certain specimens of the Grumantbyen section. Although this *YC* is quite prevalent in these samples and other specimen from the Valanginian Deer Bay Formation and Albian Christopher Formation in the Sverdrup Basin (Grasby et al., 2017), it is typically not included in the mechanistic models as it has yet to be identified at other locations and/or time periods. It is therefore likely that *YC* does not constitute a primary phase (i.e., formed secondarily) and is thus not crucial for understanding the general formation of glendonites.

5. Discussion

5.1. Glendonite formation

5.1.1. Isotopic constraints and biogeochemical processes

The $\delta^{13}C_{carb}$ of various ikaite and glendonite specimens shows a wide range in values (Figure 5.1), with -60 to 3‰ for ikaite type 3 (Lu et al., 2012; Morales et al., 2017b) and -45 to 0‰ for glendonites (Selleck et al., 2007; Teichert and Luppold, 2013; Morales et al., 2017a; Morales et al., 2017b). In general, more negative $\delta^{13}C_{carb}$ values in glendonites are associated with $\delta^{18}O_{carb}$ values closest to that of seawater and ikaite. Because of this, these glendonites are believed to most accurately reflect the conditions in which precursor ikaite was formed and may therefore also be interpreted as the specimens that are best preserved (Frank et al., 2008; Morales et al., 2017a; Morales et al., 2017b). In previous studies, the glendonites with these very negative $\delta^{13}C_{carb}$ values (i.e., lower than -30‰) have been associated with AOM, while positive $\delta^{13}C_{carb}$ values were attributed to methanogenesis, and intermediate $\delta^{13}C_{carb}$ values (-30 to 0‰) to a mixture of organic carbon (degradation of OM) and seawater (Lu et al., 2012; Teichert and Luppold, 2013; Peckmann, 2017; Qu et al., 2017; Morales et al., 2017b). The general inverse correlation towards more positive $\delta^{13}C_{carb}$ values and more negative $\delta^{18}O_{carb}$ values exhibited by all glendonites (Figure 5.1) has been suggested to reflect burial diagenesis (Frank et al., 2008; Price and Nunn, 2010; Morales et al., 2017a; Vickers et al., 2018), and together with the prevalence of the 3 distinct paragenetic phases suggests that ikaite (and subsequently glendonites) are formed through similar biogeochemical processes. However, due to ambiguous $\delta^{13}C_{carb}$ values and other uncertainties regarding the factors that govern the ikaite-to-glendonite transformation it has proven to be quite difficult to constrain the relative importance of these different biogeochemical processes.
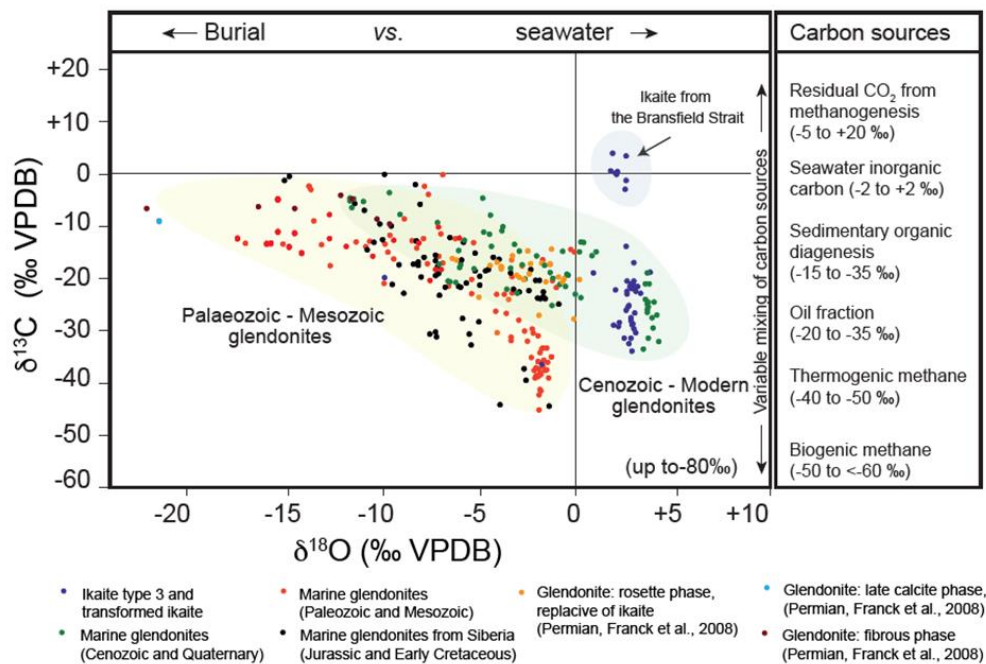
Figure 5.1 – *Compilation of published $\delta^{13}C_{carb}$ and $\delta^{18}O_{carb}$ data (reported as ‰ VPDB) measured on ikaite (type 3), whole glendonite samples, and specific carbonate phases within glendonites plotted together with potential carbon sources (Morales et al., 2017b). For additional information about each specimen please refer to the Supplementary Information from the article of the aforementioned author.*

If we try to disentangle these ambiguous $\delta^{13}C_{carb}$ values by comparing the features of the established structural glendonite groups (Table 4-1) with their respective isotopic compositions (Figure 4.14) it becomes apparent that despite the similarities in overall cementation patterns, the isotopic composition is not a clear predictor of type of internal structure and/or expression of the carbonate phases. If this finding is not the result of shortcomings in the sampling method (location of drilling does not exactly overlap with the location of thin-section) for the isotopic measurements then it would be a bit puzzling as studied glendonites do indeed show the same typical general inverse correlation (cf., Figure 4.10, Figure 4.14, and Figure 5.1). This general inverse correlation, that was also found within the diagenetic features from this study (Figure 4.12), was previously ascribed to either reflect the transition in carbon source with depth (from microbial OM in the sulphate reduction zone or primary-sourced OM settling on the seabed towards increasingly more marine DIC) throughout the various paragenetic phases (Selleck et al., 2007; Frank et al., 2008; Vickers et al., 2018) or the tendency of a methane-enriched system to progress towards a closed system (Morales et al., 2017a; Morales et al., 2017b). The latter is explained by the fact that carbonates with more negative $\delta^{13}C_{carb}$ values (up to -45‰) and $\delta^{18}O_{carb}$ value close to seawater (i.e., 0‰) are formed through the oxidation of allochthonous methane in pore waters that are in contact with the ocean, whereas carbonates with more positive $\delta^{13}C_{carb}$ values and more negative $\delta^{18}O_{carb}$ values (of up to 0 and -20‰ respectively) are formed deeper in the sedimentary column from carbon derived from upwardly diffusing methane that was formed by methanogenesis and oxygen that originated from diagenetic fluids (Birgel et al., 2015; Morales et al., 2017a; Morales et al., 2017b).

Although ikaite as well as recent Holocene glendonites and Early Jurassic (proto-) glendonites, which both lack later paragenetic phases, typically show negative $\delta^{13}C_{carb}$ values (of up to -34‰ for ikaite, Figure 5.1; -35.97 to −42.42‰ for the (proto-)glendonites) and $\delta^{18}O_{carb}$ values close to seawater (on average 2.4‰ for ikaite, Figure 5.1; -1.80 to -2.01‰ for the (proto-)glendonites), it remains unclear if methane is prerequisite for the formation of marine ikaite (i.e., type 3) or its transformation to glendonites as phase specific sampling is almost always prohibited by interfingering of the paragenetic phases (Teichert and Luppold, 2013; Peckmann, 2017; Morales et al., 2017b; Vickers et al., 2018). This, combined with the recent discovery of biomarkers for organoclastic sulphate reduction in a glendonite specimen supports the idea that methane is not a requirement for the formation of ikaite/glendonites and that large differences in $\delta^{13}C$ composition (cf., Figure 4.10, Figure 4.14, and Figure 5.1) are more readily explained through the utilization of different carbon sources (Selleck et al., 2007; Grasby et al., 2017; Qu et al., 2017; Vickers et al., 2018), which in term could be responsible for the heterogeneity and large variety in internal structures of glendonites.

5.1.2. Mechanistic model

Using the frameworks from the previously published mechanistic models for glendonite formation (Greinert and Derkachev, 2004; Teichert and Luppold, 2013; Morales et al., 2017b; Vickers et al., 2018) and combining these with (indigenous) observations and constraints from other relevant studies have led towards the formulation of the following mechanistic model for the formation of the glendonites from Spitsbergen. Please note that some of these interpretations are based upon correlations with other studies and thus lack robust evidence from the glendonites that were studied.

1. The formation of these glendonites started with the precipitation of ikaite within a shallow zone, situated close to the SMT, where elevated levels of DIC (above ±40 mM at local pH), Ca^{2+}, and PO_4^{3-} (above ±400 µM) in cold marine waters are believed to have been the most important factors for providing ikaite precedence over the other polymorphs (Lu et al., 2012; Zhou et al., 2015). Depending on the local $\delta^{13}C_{DIC}$ profile, SMT stability, crystal growth rate, and depth of formation, there may have been some variation $\delta^{13}C_{carb}$ of this ikaite, similar to what is observed within recent Quaternary ikaite (Figure 5.1) (Lu et al., 2012; Morales et al., 2017b). Although their estimates are less accurate than those for ikaite type 1, with laboratory synthesis experiments combined with extrapolation of modern examples Lu et al. (2012) showed that growing ikaite type 3 crystals could have reached dimensions of 1.0 x 3.0 cm and 1.5 x 4.5 cm within a few decades If we assume that recorded glendonite sizes are equal to that of the ikaite crystal before it broke down, we this would mean that in most cases the glendonites from the Festningen section (0.4 x 0.8 cm to 2.5 x 2.8 cm) should have been formed well within this timescale, while those from the Grumantbyen section (2.0 cm (diameter) to 7.5 x 8.7 cm) took considerably longer to grow. This approach is of course not entirely correct as some glendonites show signs of collapse or compaction and in many specimens the *Ros* phase constitutes either more or less than the expected 31.4% of the volume of the pseudomorph (as the water that is lost makes up 68.6% of the structure of ikaite) (Larsen, 1994; De Lurio and Frakes, 1999; Vickers et al., 2018). Nevertheless, it would still safe to say that all glendonites from this study were formed on short geological timescales, which together with observations such as dissolution events and sediment draping (Figure 4.9A,E), make it very reasonable for ikaite to still be situated within unconsolidated sediment around the SMT when the ikaite crystals reached their final size.

2. As a result of changing porewater conditions, ikaite became unstable and started to break down. It remains unclear whether this change in conditions is related a uniform factor or changes in different factors. In this model, it is assumed that the most likely perpetrator is thermal destabilization as a result of increased burial in conjunction with a decrease in solution supersaturation with respect to ikaite (due to mineral formation). Another way in which this destabilization could have occurred is through significant transport of sediment away from the area (between the fair-weather wave base and storm wave base) during storms as many of the glendonites found within this study are located close to or directly beneath deposits hummocky cross-stratification, a phenomenon that has also been noted in other studies (James et al., 2005; Selleck et al., 2007). For the original crystal structure to be preserved, the break down should have occurred rather slowly (Bischoff et al., 1993a; Purgstaller et al., 2017). However, the abundancy in inclusions (could also be a relict of ikaite) and low morphological perfection of the *Ros* phase (Figure 4.5-4.8) controversially advocate a more rapid formation (directly from ikaite) within a disequilibrium (Bischoff et al., 1993a; Huggett et al., 2005; Hansen et al., 2011; Purgstaller et al., 2017; Qu et al., 2017). These contrasting notions seem to

suggest that either some a certain concord was reached in order to achieve pseudomorphosis or that structural support was provided through other means. One possibility could be that the break down of ikaite itself was rapid, but involved the formation of intermediate compounds (e.g., vaterite, aragonite) that later transformed into the calcite observed as the *Ros* phase (Sánchez-Pastor et al., 2016; Vickers et al., 2018). Another way in which structural integrity could have been maintained is through heterogenous break down of ikaite, where for example the rim or certain parts of the crystal decompose first. This last process provides an elegant explanation for the large size differences of the *Ros* crystals (i.e., 15-400 µm in diameter) observed within this and other studies (Morales et al., 2017b), but would simultaneously also complicate the established contemporary relationship between the different carbonate phases as the rims tend to show the same structural elements are the cores (not always the case for the zoned glendonites). In any case, a uniform process that should have initially prevented the pore space from collapsing would be the positive pressure (directed away from the ikaite crystal) created by the water that is released from the decomposing ikaite crystal (Larsen, 1994; Frank et al., 2008). In addition to providing stability, this mechanism would also temporarily isolate the ikaite crystal from the surrounding pore waters, resulting in the pure calcite observed within the *Ros* phases as only ions released by ikaite, known to incorporate less minor or trace elements than the other polymorphs, can be incorporated (Larsen, 1994; Purgstaller et al., 2017).

3. Soon after this initial transformation, the newly formed *Ros* crystals appear to have been subjected to dissolution as indicated by their often truncated or flattened rims (Figure 4.5-4.8) (Morales et al., 2017b). This phenomenon is quite confusing as the transformation of ikaite (to the *Ros* phase) and the formation of the subsequent *Bot* phase are thought to have occurred around similar depth intervals (Morales et al., 2017b; Vickers et al., 2018). However, a potential cause for this drastic change could have been the fact that the positive pressure exerted by the decomposition water receded and thereby allowed the pore waters to enter porous crystal mesh. Other possibilities include: a decrease in either or both $[Ca^{2+}]$ and $[PO_4^{3-}]$ (e.g., potentially as a result of coprecipitation with ikaite) or changes in the phosphate speciation due to lowered alkalinity/pH as these factors are influenced by ikaite precipitation also more likely to vary in marine pore waters than Mg^{2+} and SO_4^{2-} (Burton, 1993; Hu et al., 2014a; Hu et al., 2014b; Zhou et al., 2015).

4. Following these hostile conditions, somehow precipitation conditions became favorable again for the deposition of the *Bot* phase (possibly through an increase in Ca^{2+}/alkalinity or the removal of an inhibitor). As the morphology of this particular phase varies between glendonites as well as within a single specimen, it is hypnotized either calcite or aragonite (as an intermediate step) precipitated based upon local Mg^{2+}/Ca^{2+} ratios, pH, and flow restriction within the pore space of each glendonite (i.e., geometry) (Burton and Walter, 1990; Flügel, 2013). As many of these *Bot* phases have been identified as Fe-bearing (<3 mol% $FeCO_3$) or Mg-bearing (<6 mol% $MgCO_3$) in other studies and tend to lack pyrite (Qu et al., 2017; Vickers et al., 2018), it seems that precipitation occurred in an area with low $[SO_4^{2-}]$, which would fit the methanic zone. Although the methane derived DIC ($\delta^{13}C_{carb}$ = -30 to -110‰) in this zone would mix with the native DIC pool, leading to more positive $\delta^{13}C_{carb}$ values, this scenario could prove to be unsuitable for the zoned glendonites due to high contribution in *Bot* phases (i.e., estimated to be around 75-85% of the total volume) and quite positive $\delta^{13}C_{carb}$ values (Figure 4.10) (Peckmann, 2017; Morales et al., 2017b). This problem would be less pronounced with upwelling hydrocarbons (-30‰) as a carbon source (Greinert and Derkachev, 2004; Morales et al., 2017b), but as phase specific isotope data is lacking it is impossible to allocate the growth of the *Bot* phase towards a specific carbon source.

Instead, the most logical explanation appears to be that a combination of carbon sources (i.e., oxidation of OM, DIC, methane, or hydrocarbons) were used and that the relative contribution of each source depended upon the characteristics of the local environment in which each glendonite was formed.

5. Before the deposition of the third and final *Cc* phase during deeper burial diagenesis, local dissolution of the calcitic matrix is thought to have been responsible for the etched boundaries around the *Bot* phase as well as the blocky pyrite (e.g., Figure 4.5A,B), similar to the proposed way in which were formed in cannonball concretions of another locality of the Carolinefjellet Formation (Krajewski and Luks, 2003; Vickers et al., 2018).

5.2. Glendonite preservation

Based upon the findings of this study, it is thought that there have been 2 prominent factors that have influenced and modified the observed glendonites after they were formed according to the mechanistic model. The first of these factors is a minor recrystallization that has affected each glendonite in a similar manner and manifests itself throughout each whole specimen (Figure 4.9F). This recrystallization is portrayed by irregular crystals with curved and not well-defined boundaries that tend to follow a different pattern that the original boundaries formed during the ikaite-to-glendonite transformation. Both these characteristics are commonly associated with neomorphic processes and combined with the thin width of calcite twins (dominant below 170˚C), also found within these crystals (Figure 4.9F), strongly suggest that this is the result of late diagenetic overprint due to a mutual persistent low burial temperature (Ferrill et al., 2004; Flügel, 2013). This interpretation fits with the estimated burial temperature for the more recent Paleocene sediments in the Tertiary Central Spitsbergen Basin (Figure 3.1), which yielded a maximum temperature of 120˚C with a geothermal gradient of 50°C/km (Marshall et al., 2015). The other prominent factor is the formation of the *YC* phase (Figure 4.5C-D, Figure 4.6A, Figure 4.9C) that lacks distinct textural features and seems to preferentially occur around the outer edges of the affected glendonites. Most interestingly is the observation that this phase is only exhibited by certain glendonites and that its relative contribution to the total volume varies greatly (e.g., from ±5-20% for the zoned glendonites to ±10-75% for those from the Dalkjekla Member of the Carolinefjellet Formation). The reason that this *YC* phase is not included in the mechanistic model is related to the fact that this phase has yet to be identified in other locations or time periods than the Cretaceous deposits of Svalbard and the Sverdrup Basin (Grasby et al., 2017). Therefore, it is hypothesized that this strong recrystallization was caused by a local, rather than regional, process. Potential phenomena that could have induced such a sharp and local increase in temperature are heating by magmatic intrusions (i.e., HALIP) or deformation, both of which are shown to be common within the Early Cretaceous stratigraphy of Svalbard and Ellef Ringnes Island (Corfu et al., 2013; Senger et al., 2014; Grasby et al., 2017). Since the glendonite that harbor the highest proportion of this *YC* phase (i.e., those from the Aptian Dalkjegla Member) are also the ones that are estimated to contain less than the expected 31.4% of the *Ros* phase (Larsen, 1994; De Lurio and Frakes, 1999; Vickers et al., 2018), it could be possible that the *YC* phase was formed at the expense of the original *Ros* phase. Based upon the lack of textural features related to the previously mentioned late diagenetic overprint within the *YC* phase, it is postulated that this recrystallization was the more recent process that strongly affected the glendonites.

Another factor that is common within the diagenetic evolution of carbonate rocks and could have influenced the preservation of these glendonites is alteration through mediation by meteoric fluids (Swart, 2015). This process occurs within the meteoric phreatic zone and results in more negative $\delta^{18}O_{carb}$ and $\delta^{13}C_{carb}$ values, that is generally referred to as the inverted 'J' pattern seen within $\delta^{18}O_{carb}$ and $\delta^{13}C_{carb}$ cross plots (Flügel, 2013; Swart, 2015). While glendonites from this study do show the increasingly more negative $\delta^{18}O_{carb}$ values, $\delta^{13}C_{carb}$ instead tends to become more positive, resulting in the aforementioned general inverse correlation (Figure 4.10; Figure 5.1) that, although less evident, can also be seen in the diagenetic features (Figure 4.10). Based upon these observations, it would be reasonable to say that the glendonites and their host sediment formed relatively closed systems and were thus not readily affected by this process. However, the abundancy in cracks, fractures, joints, and fluid dissolution events in all specimens (Figure 4.5-4.8) makes this seem unlikely. Alternatively, this discrepancy could also be related to the fact that the overall alteration rate for $\delta^{13}C_{carb}$ has been found to take considerably longer than that of $\delta^{18}O_{carb}$ (Campbell, 2006; Swart, 2015). In any case, based upon the current evidence it seems eligible to assume that this process did not alter the glendonites to a large extent.

The combined effect of these 2 prominent alteration factors would suggest that the glendonites from the Aptian Dalkjegla Member (Festningen section) are the least preserved and according to the general hypothesis should represent the most positive $\delta^{18}O_{carb}$ and most negative $\delta^{13}C_{carb}$ values. Unfortunately, this is not the case (Figure 4.10), and thus a clear relationship between isotopic composition and preservation cannot be established with the current data set.

6. Conclusion and outlook

Detailed petrological observations combined with bulk isotopic compositions of glendonites from adjoining locations on Spitsbergen formed during complementary time periods provide novel constraints on the ikaite-to-glendonite transformation and the utility of glendonites as a mineralogical archive of paleoclimatic significance. The characterization of 5 different groups (some with subgroups) according to trends in internal structure showed that none of these groups exhibited a clear relationship with their respective bulk isotopic compositions. Instead, specific internal structures were found to correlate best with their corresponding sedimentological environments (or potentially geochemical conditions) and respective period of formation.

Although optical microscopy and UV fluorescence proved to be insufficient to establish exact ikaite-to-glendonite transformation models for each of the groups, the formation of the studied glendonites fits best within a framework that combines facets of existing mechanistic models proposed by Morales et al. (2017b) and Vickers et al. (2018) with additional observations from this study that are thought clarify certain temporal and spatial relationships within the paragenetic sequence.

The striking contrast between more or less uniform expressions of the *Ros* phase and profound differences in that of the *Bot* phase strongly suggests that precipitation conditions were more consistent during the initial break down of ikaite than during the formation of later carbonate phases. This makes sense if the water released from the decomposing ikaite does indeed temporarily isolate the crystal from the surrounding pore waters, which are likely to be more variable, and thus advocates to notion that the factors which govern ikaite precipitation are not necessarily the same as those that ensure its transformation to glendonites and the formation of later carbonate phases.

Undiagnostic $\delta^{13}C_{carb}$ values, that do not appear to have been altered to a great extent, indicate that ikaite and the glendonites were most likely formed using a mixture of different carbon sources. It is therefore hypnotized that glendonites with the most negative $\delta^{13}C_{carb}$ values, together with $\delta^{18}O_{carb}$ values closest to that of ambient seawater, are not automatically also the ones which are best-preserved. Instead, it is postulated that based upon the relevant combination of biogeochemical processes, the timing of secondary mineral formation, and the corresponding preservation, it is possible to obtain best-preserved glendonites with different bulk isotopic compositions.

These results underline the importance of separating the governing conditions of ikaite formation and its subsequent transformation to glendonites as well as making clear distinctions between each carbonate phase within the paragenetic sequence. Future studies should therefore strive to gain as much information from each individual phase as possible by using an integrative approach that combines staining thin-section (or using EPME and µXRF) together with multiple microscopy techniques (e.g., optical, UV fluorescence, cathodoluminescence, electron microprobe) and other promising approaches (Peckmann, 2017) such as: (1) analyzing lipid biomarkers (Qu et al., 2017), (2) studying the isotopic composition of carbonate-associated sulfate (CAS) (Qu et al., 2017), (3) studying the molecular and isotopic composition of gas inclusions (Morales et al., 2017a) without putting too much emphasis on the composition and $\delta^{13}C$ of ethane and propane (Blumenberg et al., 2017), and (4) a comparison with common carbonate mineral phases in seep limestones (Morales et al., 2017a). Additionally, technological advances and other approaches that enable phase-specific sampling would also be of immense value.

Acknowledgements

References

Birgel, D., Meister, P., Lundberg, R., Horath, T. D., Bontognali, T. R. R., Bahniuk, A. M., de Rezende, C. E., Vasconcelos, C., and McKenzie, J. A., 2015, Methanogenesis produces strong 13C enrichment in stromatolites of Lagoa Salgada, Brazil: a modern analogue for Palaeo-Neoproterozoic stromatolites?: Geobiology, v. 13, no. 3, p. 245-266.

Bischoff, J. L., Fitzpatrick, J. A., and Rosenbauer, R. J., 1993a, The Solubility and Stabilization of Ikaite (CaCO3·6H2O) from 0° to 25°C: Environmental and Paleoclimatic Implications for Thinolite Tufa: The Journal of Geology, v. 101, no. 1, p. 21-33.

Bischoff, J. L., Herbst, D. B., and Rosenbauer, R. J., 1991, Gaylussite formation at mono lake, california: Geochimica et Cosmochimica Acta, v. 55, no. 6, p. 1743-1747.

Bischoff, J. L., Stine, S., Rosenbauer, R. J., Fitzpatrick, J. A., and Stafford, T. W., 1993b, Ikaite precipitation by mixing of shoreline springs and lake water, Mono Lake, California, USA: Geochimica et Cosmochimica Acta, v. 57, no. 16, p. 3855-3865.

Blumenberg, M., Pape, T., Seifert, R., Bohrmann, G., and Schlömer, S., 2017, Can hydrocarbons entrapped in seep carbonates serve as gas geochemistry recorder?: Geo-Marine Letters.

Boch, R., Dietzel, M., Reichl, P., Leis, A., Baldermann, A., Mittermayr, F., and Pölt, P., 2015, Rapid ikaite (CaCO3·6H2O) crystallization in a man-made river bed: Hydrogeochemical monitoring of a rarely documented mineral formation: Applied Geochemistry, v. 63, p. 366-379.

Boggs, S., and Hull, D. A., 1975, The Ore bin; Vol. 37 No. 6 (June 1975).

Boistelle, R., and Astier, J. P., 1988, Crystallization mechanisms in solution: Journal of Crystal Growth, v. 90, no. 1, p. 14-30.

Brookes, I. A., McAndrews, J. H., and von Bitter, P. H., 1982, Quaternary interglacial and associated deposits in southwest Newfoundland: Canadian Journal of Earth Sciences, v. 19, no. 3, p. 410-423.

Brooks, R., Clark, L. M., and Thurston, E. F., 1950, Calcium carbonate and its hydrates: Philosophical Transactions of the Royal Society of London. Series A, Mathematical and Physical Sciences, v. 243, no. 861, p. 145-167.

Browell, E., 1860, Description and analysis of an undescribed mineral from Jarrow Slake: Tyneside Naturalists Field Club, v. 5, p. 103-104.

Buchardt, B., Israelson, C., Seaman, P., and Stockmann, G., 2001, Ikaite Tufa Towers in Ikka Fjord, Southwest Greenland: Their Formation by Mixing of Seawater and Alkaline Spring Water: Journal of Sedimentary Research, v. 71, no. 1, p. 176-189.

Buchardt, B., Seaman, P., Stockmann, G., Vous, M., Wilken, U., Düwel, L., Kristiansen, A., Jenner, C., Whiticar, M. J., Kristensen, R. M., Petersen, G. H., and Thorbjørn, L., 1997, Submarine columns of ikaite tufa: Nature, v. 390, p. 129.

Burton, E. A., 1993, Controls on marine carbonate cement mineralogy: review and reassessment: Chemical Geology, v. 105, no. 1, p. 163-179.

Burton, E. A., and Walter, L. M., 1990, The role of pH in phosphate inhibition of calcite and aragonite precipitation rates in seawater: Geochimica et Cosmochimica Acta, v. 54, no. 3, p. 797-808.

Campbell, K. A., 2006, Hydrocarbon seep and hydrothermal vent paleoenvironments and paleontology: Past developments and future research directions: Palaeogeography, Palaeoclimatology, Palaeoecology, v. 232, no. 2, p. 362-407.

Corfu, F., Polteau, S., Planke, S., Faleide, J. I., Svensen, H., Zayoncheck, A., and Stolbov, N., 2013, U–Pb geochronology of Cretaceous magmatism on Svalbard and Franz Josef Land, Barents Sea Large Igneous Province: Geological Magazine, v. 150, no. 6, p. 1127-1135.

Dallmann, W. K. K., T.; Nøttvedt, A., 2001, Geological map of Svalbard 1:100,000, sheet C9G Adventdalen. Map description, 1–55.

Dana, J. D., 1849, United States Exploring Expedition During the Years 1838, 1839, 1840, 1841, 1842 Under the Command of Charles Wilkes, USN: 10: Geology, C. Sherman.

David, T. W. E., 1905, Occurrence of the Pseudomorph Glendonite in New South Wales: Rec. Geol. Surv. NSW, v. 3, no. 2, p. 162-179.

De Lurio, J. L., and Frakes, L. A., 1999, Glendonites as a paleoenvironmental tool: implications for early Cretaceous high latitude climates in Australia: Geochimica et Cosmochimica Acta, v. 63, no. 7, p. 1039-1048.

Dickens, B., and Brown, W. E., 1970, Crystal structure of calcium carbonate hexahydrate at about -120.deg: Inorganic Chemistry, v. 9, no. 3, p. 480-486.

Dieckmann, G., Nehrke, G., Papadimitriou, S., Göttlicher, J., Steininger, R., Kennedy, H., Wolf-Gladrow, D., and Thomas, D. N., 2008, Calcium carbonate as ikaite crystals in Antarctic sea ice: Geophysical Research Letters, v. 35, no. 8.

Dieckmann, G., Nehrke, G., Uhlig, C., Göttlicher, J., Gerland, S., Granskog, M., and Thomas, D., 2010, Ikaite (CaCO3. 6H2O) discovered in Arctic sea ice: The Cryosphere, v. 4, p. 227-230.

Doré, A. G., Lunin, E. R., Jensen, L. N., Birkeland, Ø., Eliassen, P. E., and Fichler, C., 1999, Principal tectonic events in the evolution of the northwest European Atlantic margin: Geological Society, London, Petroleum Geology Conference series, v. 5, no. 1, p. 41-61.

Dypvik, H., Eikeland, T. A., Backer-Owe, K., Andresen, A., Johanen, H., Elverhøi, A., Nagy, J., Haremo, P., and Bjærke, T., 1991, The Janusfjellet Subgroup (Bathonian to Hauterivian) on central Spitsbergen: a revised lithostratigraphy: Polar Research, v. 9, no. 1, p. 21-44.

Elvevold, S., Dallmann, W. K., & Blomeier, D., 2007, Geology of Svalbard [popular], Norwegian Polar Institute.

Ferrill, D. A., Morris, A. P., Evans, M. A., Burkhard, M., Groshong, R. H., and Onasch, C. M., 2004, Calcite twin morphology: a low-temperature deformation geothermometer: Journal of Structural Geology, v. 26, no. 8, p. 1521-1529.

Flügel, E., 2013, Microfacies of carbonate rocks: analysis, interpretation and application, Springer Science & Business Media.

Frank, T. D., Thomas, S. G., and Fielding, C. R., 2008, Glendonites as Paleoclimatic and Paleoceanographic Indicators: A Case Study from the Glacially Influenced Permian System of Eastern Australia: Search and Discovery Article (50129).

Freiesleben, J., 1827, Ueber einige Vorkommnisse im Schlottenleimen (Alluvialthon) bey Obersdorf, ohnweit Sangerhausen: Isis, v. 20, p. 334-337.

Geptner, A. R., Vetoshkina, O. S., and Petrova, V. V., 2014, New data on the composition of stable isotopes in glendonites of the White Sea and their genesis: Lithology and Mineral Resources, v. 49, no. 6, p. 473-490.

Gjelberg, J., and Steel, R. J., 1995, Helvetiafjellet formation (Barremian-Aptian), Spitsbergen: characteristics of a transgressive succession, in Steel, R. J., Felt, V. L., Johannessen, E. P., and Mathieu, C., eds., Norwegian Petroleum Society Special Publications, Volume 5, Elsevier, p. 571-593.

Grasby, S. E., McCune, G. E., Beauchamp, B., and Galloway, J. M., 2017, Lower Cretaceous cold snaps led to widespread glendonite occurrences in the Sverdrup Basin, Canadian High Arctic: GSA Bulletin, v. 129, no. 7-8, p. 771-787.

Greinert, J., and Derkachev, A., 2004, Glendonites and methane-derived Mg-calcites in the Sea of Okhotsk, Eastern Siberia: implications of a venting-related ikaite/glendonite formation: Marine Geology, v. 204, no. 1, p. 129-144.

Grundvåg, S. A., Marin, D., Kairanov, B., Śliwińska, K. K., Nøhr-Hansen, H., Jelby, M. E., Escalona, A., and Olaussen, S., 2017, The Lower Cretaceous succession of the northwestern Barents Shelf: Onshore and offshore correlations: Marine and Petroleum Geology, v. 86, p. 834-857.

Han, X., Schultz, L., Zhang, W., Zhu, J., Meng, F., and Geesey, G. G., 2016, Mineral formation during bacterial sulfate reduction in the presence of different electron donors and carbon sources: Chemical Geology, v. 435, p. 49-59.

Hansen, M. O., Buchardt, B., Kühl, M., and Elberling, B., 2011, The Fate of the Submarine Ikaite Tufa Columns in Southwest Greenland Under Changing Climate Conditions: Journal of Sedimentary Research, v. 81, no. 8, p. 553-561.

Harland, W. B., Anderson, L. M., Manasrah, D., Butterfield, N. J., Challinor, A., Doubleday, P. A., Dowdeswell, E. K., Dowdeswell, J. A., Geddes, I., and Kelly, S. R., 1997, The geology of Svalbard, Geological Society.

Henriksen, E., Bjørnseth, H. M., Hals, T. K., Heide, T., Kiryukhina, T., Kløvjan, O. S., Larssen, G. B., Ryseth, A. E., Rønning, K., Sollid, K., and Stoupakova, A., 2011, Chapter 17 Uplift and erosion of the greater Barents Sea: impact on prospectivity and petroleum systems: Geological Society, London, Memoirs, v. 35, no. 1, p. 271-281.

Herrle, J. O., Schröder-Adams, C. J., Davis, W., Pugh, A. T., Galloway, J. M., and Fath, J., 2015, Mid-Cretaceous High Arctic stratigraphy, climate, and Oceanic Anoxic Events: Geology, v. 43, no. 5, p. 403-406.

Hesse, K., Küppers, H., and Suess, E., 1983, Refinement of the structure of Ikaite, CaCO3·6H2O: Zeitschrift für Kristallographie-Crystalline Materials, v. 163, no. 1-4, p. 227-232.

Hiki, T., 1915, Tadasu Hiki: On the Gennoishi (Memoirs., Kyoto Imperial University., Vol., 1., No., 2, 1915, p., 55-58.,): 地質學雜誌, v. 22, no. 259, p. 176-178.

Hu, Y.-B., Dieckmann, G. S., Wolf-Gladrow, D. A., and Nehrke, G., 2014a, Laboratory study on coprecipitation of phosphate with ikaite in sea ice: Journal of Geophysical Research: Oceans, v. 119, no. 10, p. 7007-7015.

Hu, Y.-B., Wolf-Gladrow, D. A., Dieckmann, G. S., Völker, C., and Nehrke, G., 2014b, A laboratory study of ikaite (CaCO3·6H2O) precipitation as a function of pH, salinity, temperature and phosphate concentration: Marine Chemistry, v. 162, p. 10-18.

Hu, Y.-B., Wolthers, M., Wolf-Gladrow, D. A., and Nehrke, G., 2015, Effect of pH and Phosphate on Calcium Carbonate Polymorphs Precipitated at near-Freezing Temperature: Crystal Growth & Design, v. 15, no. 4, p. 1596-1601.

Huggett, J. M., Schultz, B. P., Shearman, D. J., and Smith, A. J., 2005, The petrology of ikaite pseudomorphs and their diagenesis: Proceedings of the Geologists' Association, v. 116, no. 3, p. 207-220.

Ito, T., 2004, Comparative isotopic (delta18O, delta13C) study between gennoishi and thinolite of Pyramid Lake, Nevada: Journal of Hokkaido University of Education. Natural Sciences (Japan).

James, N. P., Narbonne, G. M., Dalrymply, R. W., and Kyser, T. K., 2005, Glendonites in Neoproterozoic low-latitude, interglacial, sedimentary rocks, northwest Canada: Insights into the Cryogenian ocean and Precambrian cold-water carbonates: Geology, v. 33, no. 1, p. 9-12.

Jones, M. T., Augland, L. E., Shephard, G. E., Burgess, S. D., Eliassen, G. T., Jochmann, M. M., Friis, B., Jerram, D. A., Planke, S., and Svensen, H. H., 2017, Constraining shifts in North Atlantic plate motions during the Palaeocene by U-Pb dating of Svalbard tephra layers: Scientific Reports, v. 7, no. 1, p. 6822.

Kaplan, M., 1978, Calcite pseudomorphoses in Jurassic and Lower Cretaceous deposits of the northern area of eastern Siberia: Geol. Geofiz, v. 19, p. 62-70.

-, 1979, Calcite pseudomorphs (pseudogaylussite, jarrowite, thinolite, glendonite, gennoishi, White Sea hornlets) in sedimentary rocks; origins of the pseudomorphs: Lithology and Mineral Resources, v. 14, no. 5, p. 623-636.

Kemper, E., 1987, Das Klima der Kreidezeit.

Kemper, E., and Schmitz, H., 1975, Stellate nodules from the upper Deer Bay formation (Valanginian) of Arctic Canada: Geological Survey of Canada, Paper, v. 75, p. 109-119.

King, C., 1878, Report of the Geological Exploration of the Fortieth Parallel, Volume I: Systematic Geology.

Koevoets, M. J., Abay, T. B., Hammer, Ø., and Olaussen, S., 2016, High-resolution organic carbon–isotope stratigraphy of the Middle Jurassic–Lower Cretaceous Agardhfjellet Formation of central Spitsbergen, Svalbard: Palaeogeography, Palaeoclimatology, Palaeoecology, v. 449, p. 266-274.

Koevoets, M. J., Hammer, Ø., Olaussen, S., Senger, K., and Smelror, M., 2018, Integrating subsurface and outcrop data of the Middle Jurassic to Lower Cretaceous Agardhfjellet Formation in central Spitsbergen: Norwegian Journal of Geology, v. 98, no. 4, p. 1-34.

Krajewski, K. P., and Luks, B., 2003, Origin of "cannon-ball" concretions in the Carolinefjellet Formation (Lower Cretaceous), Spitsbergen: Polish Polar Res, v. 24, no. 3-4, p. 217-242.

Larsen, D., 1994, Origin and paleoenvironmental significance of calcite pseudomorphs after ikaite in the Oligocene Creede Formation, Colorado: Journal of Sedimentary Research, v. 64, no. 3a, p. 593-603.

Leever, K. A., Gabrielsen, R. H., Faleide, J. I., and Braathen, A., 2011, A transpressional origin for the West Spitsbergen fold-and-thrust belt: Insight from analog modeling: Tectonics, v. 30, no. 2.

Light, M. A., 1952, Evidence of Authigenic and Detrital Glauconite: Science, v. 115, no. 2977, p. 73-75.

Lin, Y.-P., and Singer, P. C., 2005, Inhibition of calcite crystal growth by polyphosphates: Water Research, v. 39, no. 19, p. 4835-4843.

-, 2006, Inhibition of calcite precipitation by orthophosphate: Speciation and thermodynamic considerations: Geochimica et Cosmochimica Acta, v. 70, no. 10, p. 2530-2539.

Lu, Z., Rickaby, R. E. M., Kennedy, H., Kennedy, P., Pancost, R. D., Shaw, S., Lennie, A., Wellner, J., and Anderson, J. B., 2012, An ikaite record of late Holocene climate at the Antarctic Peninsula: Earth and Planetary Science Letters, v. 325-326, p. 108-115.

Maher, H. D., 2001, Manifestations of the Cretaceous High Arctic Large Igneous Province in Svalbard: The Journal of Geology, v. 109, no. 1, p. 91-104.

Marland, G., 1975, The stability of CaCO3·6H2O (ikaite): Geochimica et Cosmochimica Acta, v. 39, no. 1, p. 83-91.

Marshall, C., Uguna, J., Large, D. J., Meredith, W., Jochmann, M., Friis, B., Vane, C., Spiro, B. F., Snape, C. E., and Orheim, A., 2015, Geochemistry and petrology of palaeocene coals from Spitzbergen — Part 2: Maturity variations and implications for local and regional burial models: International Journal of Coal Geology, v. 143, p. 1-10.

Midtkandal, I., Nystuen, J. P., Nagy, J., and Mørk, A., 2008, Lower Cretaceous lithostratigraphy across a regional subaerial unconformity in Spitsbergen: the Rurikfjellet and Helvetiafjellet formations: Norwegian Journal of Geology / Norsk Geologisk Forening, v. 88, no. 4, p. 287-304.

Morales, C., Rogov, M. A., de Lange, G. J., and van de Schootbrugge, B., 2017b, Glendonites: formation, distribution, and significance for understanding paleo-environmental conditions at high latitudes: Unpublished.

Morales, C., Rogov, M. A., Wierzbowski, H., Ershova, V. B., Suan, G., Adatte, T., Föllmi, K. B., Tegelaar, E., Reichart, G.-J., de Lange, G. J., Middelburg, J. J., and van de Schootbrugge, B., 2017a, Glendonites track methane seepage in Mesozoic polar seas: Geology, v. 45, no. 6, p. 503-506.

Nielsen, T., Laier, T., Kuijpers, A., Rasmussen, T. L., Mikkelsen, N. E., and Nørgård-Pedersen, N., 2014, Fluid flow and methane occurrences in the Disko Bugt area offshore West Greenland: indications for gas hydrates?: Geo-Marine Letters, v. 34, no. 6, p. 511-523.

Oehlerich, M., Mayr, C., Griesshaber, E., Lücke, A., Oeckler, O. M., Ohlendorf, C., Schmahl, W. W., and Zolitschka, B., 2013, Ikaite precipitation in a lacustrine environment – implications for palaeoclimatic studies using carbonates from Laguna Potrok Aike (Patagonia, Argentina): Quaternary Science Reviews, v. 71, p. 46-53.

Omelon, C. R., Pollard, W. H., and Marion, G. M., 2001, Seasonal formation of ikaite (CaCO3·6H2O) in saline spring discharge at Expedition Fiord, Canadian High Arctic: Assessing conditional constraints for natural crystal growth: Geochimica et Cosmochimica Acta, v. 65, no. 9, p. 1429-1437.

Pauly, H., 1963, "Ikaite", a New Mineral from Greenland: 1963, v. 16, no. 4, p. 2.

Peckmann, J., 2017, Unleashing the potential of glendonite: A mineral archive for biogeochemical processes and paleoenvironmental conditions: Geology, v. 45, no. 6, p. 575-576.

Peckmann, J., Thiel, V., Michaelis, W., Clari, P., Gaillard, C., Martire, L., and Reitner, J., 1999, Cold seep deposits of Beauvoisin (Oxfordian; southeastern France) and Marmorito (Miocene; northern Italy): microbially induced authigenic carbonates: International Journal of Earth Sciences, v. 88, no. 1, p. 60-75.

Pedersen, G. K., and Buchardt, B., 1996, The calcareous concretions (cementsten) in the Fur Formation (Paleogene, Denmark): isotopic evidence of early diagenetic growth: Bulletin of the Geological Society of Denmark, v. 43, no. 1, p. 78-86.

Pelouze, M., 1865, Sur une combinaison nouvelle d'eau et de carbonate de chaux: Chemical Review, v. 60, p. 429-431.

Petersen, T. G., Thomsen, T. B. l., Olaussen, S., and Stemmerik, L., 2016, Provenance shifts in an evolving Eurekan foreland basin: the Tertiary Central Basin, Spitsbergen: Journal of the Geological Society, v. 173, no. 4, p. 634-648.

Piepjohn, K., Brinkmann, L., Grewing, A., and Kerp, H., 2000, New data on the age of the uppermost ORS and the lowermost post-ORS strata in Dickson Land (Spitsbergen) and implications for the age of the Svalbardian deformation: Geological Society, London, Special Publications, v. 180, no. 1, p. 603-609.

Piepjohn, K., von Gosen, W., Läufer, A., McClelland, W. C., and Estrada, S., 2013, Ellesmerian and Eurekan fault tectonics at the northern margin of Ellesmere Island (Canadian High Arctic) [Ellesmerische und Eurekan-Störungstektonik am Nordrand von Ellesmere Island (kanadische Hocharktis).]: Zeitschrift der Deutschen Gesellschaft für Geowissenschaften, v. 164, no. 1, p. 81-105.

Price, G. D., 1999, The evidence and implications of polar ice during the Mesozoic: Earth-Science Reviews, v. 48, no. 3, p. 183-210.

Price, G. D., and Nunn, E. V., 2010, Valanginian isotope variation in glendonites and belemnites from Arctic Svalbard: Transient glacial temperatures during the Cretaceous greenhouse: Geology, v. 38, no. 3, p. 251-254.

Purgstaller, B., Dietzel, M., Baldermann, A., and Mavromatis, V., 2017, Control of temperature and aqueous Mg2+/Ca2+ ratio on the (trans-)formation of ikaite: Geochimica et Cosmochimica Acta, v. 217, p. 128-143.

Qu, Y., Teichert, B. M. A., Birgel, D., Goedert, J. L., and Peckmann, J., 2017, The prominent role of bacterial sulfate reduction in the formation of glendonite: a case study from Paleogene marine strata of western Washington State: Facies, v. 63, no. 2, p. 10.

Rogov, M. A., Ershova, V. B., Shchepetova, E. V., Zakharov, V. A., Pokrovsky, B. G., and Khudoley, A. K., 2017, Earliest Cretaceous (late Berriasian) glendonites from Northeast Siberia revise the timing of initiation of transient Early Cretaceous cooling in the high latitudes: Cretaceous Research, v. 71, p. 102-112.

Rogov, M. A., and Zakharov, V. A., 2010, Jurassic and Lower Cretaceous glendonite occurrences and their implication for Arctic paleoclimate reconstructions and stratigraphy: Earth Science Frontiers, v. Volume 17, no. Special Issue.

Rysgaard, S., Glud, R., Lennert, K., Cooper, M., Halden, N., Leakey, R., Hawthorne, F., and Barber, D., 2012, Ikaite crystals in melting sea ice-implications for pCO. sub. 2 and pH levels in Arctic surface waters: The Cryosphere, v. 6, no. 4, p. 901-901.

Sánchez-Pastor, N., Oehlerich, M., Astilleros, J. M., Kaliwoda, M., Mayr, C. C., Fernández-Díaz, L., and Schmahl, W. W., 2016, Crystallization of ikaite and its pseudomorphic transformation into calcite: Raman spectroscopy evidence: Geochimica et Cosmochimica Acta, v. 175, p. 271-281.

Schrag, D. P., Higgins, J. A., Macdonald, F. A., and Johnston, D. T., 2013, Authigenic Carbonate and the History of the Global Carbon Cycle: Science, v. 339, no. 6119, p. 540-543.

Schubert, C. J., Nürnberg, D., Scheele, N., Pauer, F., and Kriews, M., 1997, 13C isotope depletion in ikaite crystals: evidence for methane release from the Siberian shelves ?: Geo-Marine Letters, v. 17, no. 2, p. 169-174.

Selleck, B. W., Carr, P. F., and Jones, B. G., 2007, A review and synthesis of glendonites (pseudomorphs after ikaite) with new data: Assessing applicability as recorders of ancient coldwater conditions: Journal of Sedimentary Research, v. 77, no. 11-12, p. 980-991.

Senger, K., Tveranger, J., Ogata, K., Braathen, A., and Planke, S., 2014, Late Mesozoic magmatism in Svalbard: A review: Earth-Science Reviews, v. 139, p. 123-144.

Shearman, D. J., McGugan, A., Stein, C., and Smith, A. J., 1989, Ikaite, CaCO36H2O, precursor of the thinolites in the Quaternary tufas and tufa mounds of the Lahontan and Mono Lake Basins, western United States: GSA Bulletin, v. 101, no. 7, p. 913-917.

Shearman, D. J., and Smith, A. J., 1985, Ikaite, the parent mineral of jarrowite-type pseudomorphs: Proceedings of the Geologists' Association, v. 96, no. 4, p. 305-314.

Smerlor, M. P., O.; Larssen, G.B.; Werner, S., 2009, ATLAS - Geological History of the Barents Sea, Trondheim, Norway, Geological Survey of Norway.

Spielhagen, R. F., and Tripati, A., 2009, Evidence from Svalbard for near-freezing temperatures and climate oscillations in the Arctic during the Paleocene and Eocene: Palaeogeography, Palaeoclimatology, Palaeoecology, v. 278, no. 1, p. 48-56.

Stange, R., 2009, Spitsbergen - Svalbard: a complete guide around the artic archipelago, 495 p.:

Steacy, H., and Grant, D., 1974, Tidal muds reveal mineral curiosity: Canadian Geographic, v. 88, no. 1, p. 36-38.

Stein, C. L., and Smith, A. J., 1986, Authigenic carbonate nodules in the Nankai Trough, Site 583: Init. Repts. DSDP., v. 87, p. 659-668.

Suess, E., Balzer, W., Hesse, K. F., Müller, P. J., Ungerer, C. A., and Wefer, G., 1982, Calcium Carbonate Hexahydrate from Organic-Rich Sediments of the Antarctic Shelf: Precursors of Glendonites: Science, v. 216, no. 4550, p. 1128-1131.

Sun, X., and Turchyn, A. V., 2014, Significant contribution of authigenic carbonate to marine carbon burial: Nature Geoscience, v. 7, p. 201.

Swart, P. K., 2015, The geochemistry of carbonate diagenesis: The past, present and future: Sedimentology, v. 62, no. 5, p. 1233-1304.

Teichert, B. M. A., and Luppold, F. W., 2013, Glendonites from an Early Jurassic methane seep — Climate or methane indicators?: Palaeogeography, Palaeoclimatology, Palaeoecology, v. 390, p. 81-93.

Tessensohn, F., and Piepjohn, K., 2000, Eocene compressive deformation in Arctic Canada, North Greenland and Svalbard and its plate tectonic causes: Polarforschung, v. 68, no. 1-3, p. 121-124.

Trampe, E. C. L., Larsen, J. E. N., Glaring, M. A., Stougaard, P., and Kühl, M., 2016, In situ dynamics of O2, pH, light, and photosynthesis in ikaite tufa columns (Ikka Fjord, Greenland)-A unique microbial habitat: Frontiers in Microbiology, v. 7, no. MAY.

Trechmann, C. O., 1901, Uber einen Fund von ausgezeichneten Pseudogaylussit (Thinolit Jarrowit-) Krystallen: Zeitschrift für krystallographie, v. 25, p. 283-285.

van Calker, F., 1897, XXIX. Beitrag zur Kenntniss des Pseudogaylussit und über dessen Vorkommen in Holland: Zeitschrift für Kristallographie-Crystalline Materials, v. 28, no. 1-6, p. 556-572.

Vickers, M., Watkinson, M., Price, G. D., and Jerrett, R., 2018, An improved model for the ikaite-glendonite transformation: evidence from the Lower Cretaceous of Spitsbergen, Svalbard.

Vickers, M. L., Price, G. D., Jerrett, R. M., and Watkinson, M., 2016, Stratigraphic and geochemical expression of Barremian–Aptian global climate change in Arctic Svalbard: Geosphere, v. 12, no. 5, p. 1594-1605.

Whiticar, M. J., and Suess, E., 1998, The Cold Carbonate Connection Between Mono Lake, Californiaand the Bransfield Strait, Antarctica: Aquatic Geochemistry, v. 4, no. 3, p. 429-454.

Wierzbowski, A., Hryniewicz, K., Hammer, Ø., Nakrem, H. A., and Little, C. T. S., 2011, Ammonites from hydrocarbon seep carbonate bodies from the uppermost Jurassic - Lowermost Cretaceous of Spitsbergen and their biostratigraphical importance: Neues Jahrbuch für Geologie und Paläontologie - Abhandlungen, v. 262, no. 3, p. 267-288.

Worsley, D., 2008, The post-Caledonian development of Svalbard and the western Barents Sea: Polar Research, v. 27, no. 3, p. 298-317.

Zhou, X., Lu, Z., Rickaby, R. E. M., Domack, E. W., Wellner, J. S., and Kennedy, H. A., 2015, Ikaite Abundance Controlled by Porewater Phosphorus Level: Potential Links to Dust and Productivity: The Journal of Geology, v. 123, no. 3, p. 269-281.

Appendix

A. Lithostatigraphic log
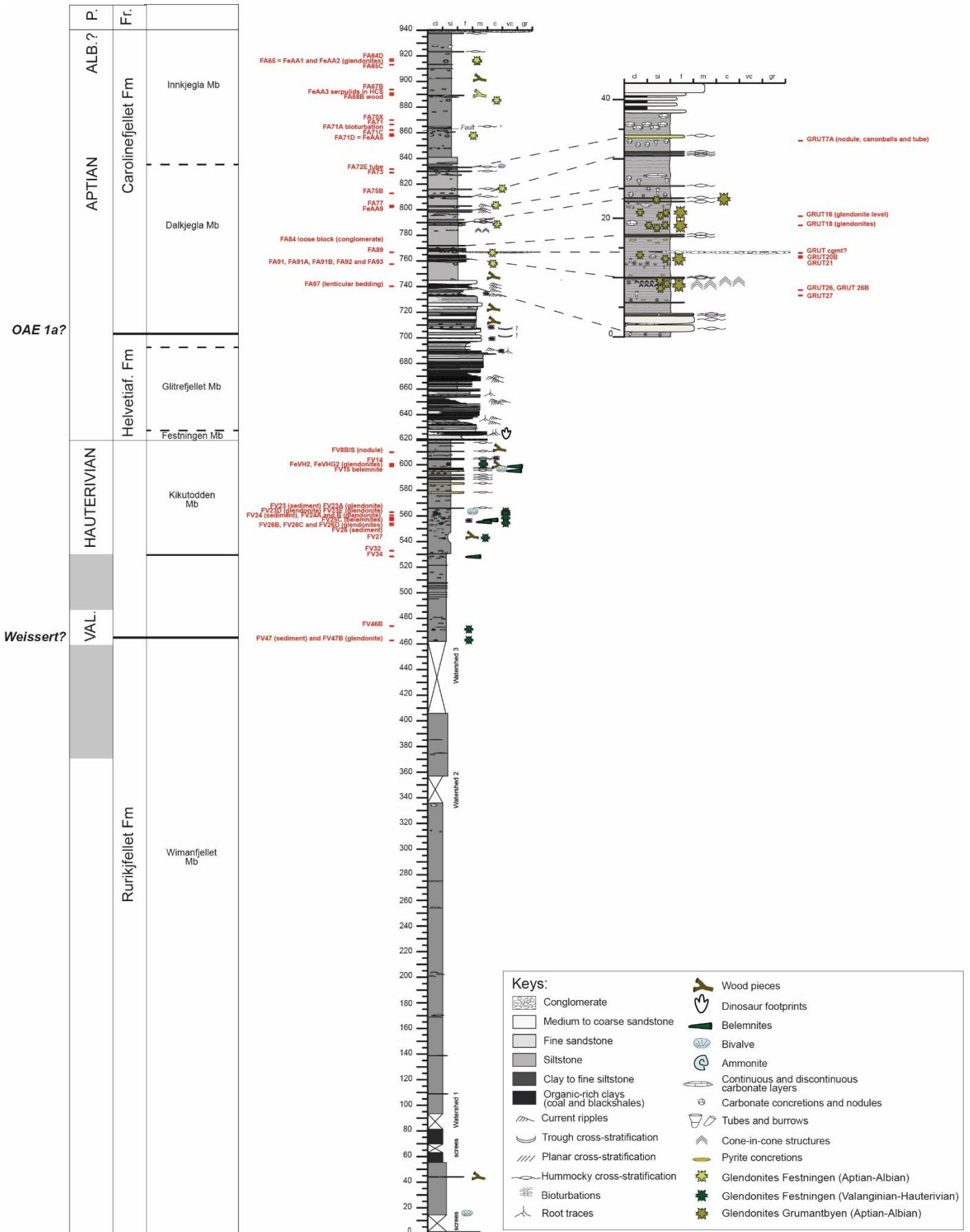
B. Sample lists

1. Glendonites

Sample ID	Section	Formation	Member	Horizon (m)	δ¹³C_carb (‰ VPDB)	δ¹⁸O_carb (‰ VPDB)	Host lithology	Shape	Size (cm)	Structure
FeAA1-1	Festningen	Carolinefjellet Fm	Innkjegla Mb	916.0	-12.26	-6.15	Siltstone	Small stellate pseudomorph	Around 1.2 x 1.8 to 2.0 x 2.5	Not zoned
FeAA1-2	Festningen	Carolinefjellet Fm	Innkjegla Mb	916.0	-14.53	-5.29	Siltstone	Small stellate pseudomorph	Around 1.2 x 1.8 to 2.0 x 2.5	Not zoned
FeAA1-3	Festningen	Carolinefjellet Fm	Innkjegla Mb	916.0	-	-	Siltstone	Small stellate pseudomorph	Around 1.2 x 1.8 to 2.0 x 2.5	Not zoned
FeAA1-4	Festningen	Carolinefjellet Fm	Innkjegla Mb	916.0	-	-	Siltstone	Small stellate pseudomorph	Around 1.2 x 1.8 to 2.0 x 2.5	Not zoned
FeAA2	Festningen	Carolinefjellet Fm	Innkjegla Mb	916.0	-14.55	-5.43	Siltstone	Small stellate pseudomorph	Around 1.0 x 1.1 to 1.4 x 1.5	Not zoned
FeAA2-2	Festningen	Carolinefjellet Fm	Innkjegla Mb	916.0	-15.30	-3.87	Siltstone	Small stellate pseudomorph	Around 1.0 x 1.1 to 1.4 x 1.5	Not zoned
FeAA5	Festningen	Carolinefjellet Fm	Innkjegla Mb	858.0	-18.22	-6.35	Siltstone with carbonate concretions, tubes/burrows, and bioturbation	Small stellate pseudomorph to small aggregate of crystals with carbonate nodule	Around 0.4 to 0.8 (diameter)	Not zoned
FeAA9	Festningen	Carolinefjellet Fm	Dalkjegla Mb	802.0	-17.87	-7.03	Fine sandstone with current ripples	Small stellate pseudomorph to small aggregate of crystals	Around 2.0 x 2.5	Not zoned
FA91-1	Festningen	Carolinefjellet Fm	Dalkjegla Mb	757.5	-	-	Fine sandstone	Small stellate pseudomorph	Around 1.4 x 1.6 to 2.5 (diameter)	Not zoned
FA91-2	Festningen	Carolinefjellet Fm	Dalkjegla Mb	757.5	-18.93	-6.13	Fine sandstone	Small stellate pseudomorph	Around 1.4 x 1.6 to 2.5 (diameter)	Not zoned
FA91A	Festningen	Carolinefjellet Fm	Dalkjegla Mb	757.5	-17.23	-6.72	Fine sandstone	Small stellate pseudomorph	Around 1.4 x 1.6 to 2.5 (diameter)	Not zoned
FA91A-2	Festningen	Carolinefjellet Fm	Dalkjegla Mb	757.5	-	-	Fine sandstone	Small stellate pseudomorph	Around 1.4 x 1.6 to 2.5 (diameter)	Not zoned
FA91B	Festningen	Carolinefjellet Fm	Dalkjegla Mb	757.5	-	-	Fine sandstone	Small stellate pseudomorph	Around 1.4 x 1.6 to 2.5 (diameter)	Not zoned
FA92-1	Festningen	Carolinefjellet Fm	Dalkjegla Mb	757.5	-18.43	-6.50	Fine sandstone	Mainly small stellate pseudomorphs (also signs of acinaform)	Around 1.5 (diameter) to 2.1 x 4.8	Not zoned
FA92-2	Festningen	Carolinefjellet Fm	Dalkjegla Mb	757.5	-16.31	-8.74	Fine sandstone	Mainly small stellate pseudomorphs (also signs of acinaform)	Around 1.5 (diameter) to 2.1 x 4.8	Not zoned
FA92-3	Festningen	Carolinefjellet Fm	Dalkjegla Mb	757.5	-18.54	4.00	Fine sandstone	Mainly small stellate pseudomorphs (also signs of acinaform)	Around 1.5 (diameter) to 2.1 x 4.8	Not zoned
FA92-4	Festningen	Carolinefjellet Fm	Dalkjegla Mb	757.5	-	-	Fine sandstone	Mainly small stellate pseudomorphs (also signs of acinaform)	Around 1.5 (diameter) to 2.1 x 4.8	Not zoned
FA93	Festningen	Carolinefjellet Fm	Dalkjegla Mb	757.5	-19.30	-6.32	Fine sandstone	Small stellate pseudomorph to small aggregate of crystals	Around 1.9 x 2.1 to 2.5 x 2.8	Not zoned
FA93-2	Festningen	Carolinefjellet Fm	Dalkjegla Mb	757.5	-	-	Fine sandstone	Small stellate pseudomorph to small aggregate of crystals	Around 1.9 x 2.1 to 2.5 x 2.8	Not zoned
FeVH2	Festningen	Rurikfjellet Fm	Kikutodden Mb	600.0	-18.41/ -17.68	-10.28/ -11.02	Siltstone with belemnites and wood pieces	Small stellate pseudomorph	Around 1.7 x 1.8	Macrozoned
FV23	Festningen	Rurikfjellet Fm	Kikutodden Mb	563.0	-10.47/ -15.44	-13.61/ -11.41	Siltstone with carbonate concretions and bivalves	Small aggregate of crystals	Around 0.9 x 1.6	Macrozoned
FV23D	Festningen	Rurikfjellet Fm	Kikutodden Mb	563.0	-14.33/ -13.69	-13.3/ -14.23	Siltstone with carbonate concretions and bivalves	Small aggregate of crystals	Around 2.5 x 3.1 to 2.8 x 4.1	-

Sample	Locality	Formation	Member	Height (m)	δ13C	δ18O	Lithology	Morphology	Size (mm)	Zoning
FV24A	Festningen	Rurikfjellet Fm	Kikutodden Mb	559.0	-23.5/ -24.14	-3.28/ -1.98	Siltstone with carbonate concretions and bivalves	Small aggregate of crystals	Around 0.9 x 1.1	Zoning
FV24B	Festningen	Rurikfjellet Fm	Kikutodden Mb	559.0	-23.15/ -23.53	-3.85/ -2.67	Siltstone with carbonate concretions and bivalves	Small single acinaform	Around 0.9 x 1.5	Macrozoned
FV25D	Festningen	Rurikfjellet Fm	Kikutodden Mb	556.0	-24.42/ -24.31	-3.19/ -3.41	Siltstone with carbonate concretions, tubes/burrows, bioturbation, and belemnites	Small aggregate of crystals to small stellate pseudomorph	Around 0.9 x 1.4 to 0.9 x 1.6	Zoning
FV25E	Festningen	Rurikfjellet Fm	Kikutodden Mb	556.0	-22.64/ -23.9	-5.87/ -2.77	Siltstone with carbonate concretions, tubes/burrows, bioturbation, and belemnites	Small aggregate of crystals	Around 1.1 x 1.6	Macrozoned
FV26	Festningen	Rurikfjellet Fm	Kikutodden Mb	554.0	-21.41/ -22.07	-5.58/ -3.07	Siltstone with carbonate concretions, tubes/burrows, bioturbation, and belemnites	Small aggregate of crystals to small stellate pseudomorph	Around 1.6 x 1.7	Macrozoned
FV26A	Festningen	Rurikfjellet Fm	Kikutodden Mb	554.0	-23.22/ -21.58	-1.95/ -3.57	Siltstone with carbonate concretions, tubes/burrows, bioturbation, and belemnites	Small aggregate of crystals to small stellate pseudomorph	-	Zoning
FV47B	Festningen	Rurikfjellet Fm	Wimanfjellet Mb	463.0	-10.21/ -10.79	-12.53/ -13.32	Siltstone with carbonate concretions and wood pieces	Small double acinaform	-	Macrozoned
GRUT16	Grumantbyen	Carolinefjellet Fm	Dalkjegla Mb?	20.5	-9.16	-10.20	Siltstone with carbonate concretions	Medium aggregate of crystals	Around 7.5 x 8.7	Not zoned
GRUT16-1	Grumantbyen	Carolinefjellet Fm	Dalkjegla Mb?	20.5	-	-	Siltstone with carbonate concretions	Medium aggregate of crystals	Around 7.5 x 8.7	Not zoned
GRUT18	Grumantbyen	Carolinefjellet Fm	Dalkjegla Mb?	18.5	-11.25	-5.53	Siltstone with carbonate concretions	Medium aggregate of crystals to medium stellate pseudomorph	Around 4.8 x 7.3	Not zoned
GRUT cgmt-a,b,c	Grumantbyen	Carolinefjellet Fm	Dalkjegla Mb?	14.0?	-6.71	-14.71	Conglomerate	Small stellate pseudomorph in carbonate concretion and broken pieces	Around 2.0 (diameter)	Not zoned
GRUT20B	Grumantbyen	Carolinefjellet Fm	Dalkjegla Mb?	13.5	-23.41	-7.08	Siltstone with carbonate concretions	Medium aggregate of crystals to medium stellate pseudomorph	Around 3.2 x 3.9	Not zoned
GRUT21	Grumantbyen	Carolinefjellet Fm	Dalkjegla Mb?	13.0	-29.20	-2.25	Siltstone with carbonate concretions, tubes/burrows, and bioturbation	Small stellate pseudomorph in carbonate concretion	Around 2.2 x 2.5	Not zoned
GRUT27	Grumantbyen	Carolinefjellet Fm	Dalkjegla Mb?	7.5	-17.43	-4.57	Siltstone with cone-in-cone structures	Medium aggregate of crystal to medium single acinaform	Around 4.3 x 6.5	Not zoned

2. Diagenetic features and sediments

Sample ID	Section	Formation	Member	Horizon (m)	$\delta^{13}C_{carb}$ (‰ VPDB)	$\delta^{18}O_{carb}$ (‰ VPDB)	Host lithology	Type of sample	Size (cm)	Remarks
FeAA6-1	Festningen	Carolinefjellet Fm	-	-	-6.33	-11.72	-	Tube	Around 1.9 x 2.0 x 5.3	
FeAA6-2	Festningen	Carolinefjellet Fm	-	-	-18.81	-6.36	-	Tube	Around 1.9 x 2.0 x 5.3	
FA64D	Festningen	Carolinefjellet Fm	Innkjegla Mb	917.5	-2.3	-10.6	Siltstone	Sediment	Around 3.8 x 13.3	
FA65C	Festningen	Carolinefjellet Fm	Innkjegla Mb	913.0	-3.07	-11.04	Siltstone	Concretion	Around 4.5 x 6.2	Corresponds to FeAA1 and FeAA2
FA67B	Festningen	Carolinefjellet Fm	Innkjegla Mb	894.0	-9.61/ -11.67	-6.73	Siltstone	Concretion	Around 3.3 x 3.8	
FA68B	Festningen	Carolinefjellet Fm	Innkjegla Mb	889.5	-4.61/ -8.9	-9.45/ -7.03	Pyrite concretion (siltstone)	Wood	Around 1.8 x 4.0 x 4.3	
FA70X	Festningen	Carolinefjellet Fm	Innkjegla Mb	870.0	-4.57/ -6.6	-14.76/ -13.3	Siltstone	Limestone on fault	Around 3.6 x 4.2 x 4.3	
FA71A	Festningen	Carolinefjellet Fm	Innkjegla Mb	862.0	-7.44	-13.09	Siltstone	Sediment	Around 2.7 x 4.2	Bioturbation
FA71A-2	Festningen	Carolinefjellet Fm	Innkjegla Mb	862.0	-7.68	-10.82	Siltstone	Sediment	Around 2.7 x 4.2	Bioturbation; cone in cone fragments
FA71C	Festningen	Carolinefjellet Fm	Innkjegla Mb	859.0	-16.28	-4.89	Siltstone	Nodule	Around 3.0 (diameter) x 2.1	
FA71D-1	Festningen	Carolinefjellet Fm	Innkjegla Mb	857.5	-20.06	-4.08	Siltstone	Nodule	Around 0.8-0.9 (diameter) x 1.8	
FA71D-2	Festningen	Carolinefjellet Fm	Innkjegla Mb	857.5	-12.30	-12.17	Siltstone	Sediment	Around 0.8 x 2.7 to 2.0 x 4.0	
FA72E	Festningen	Carolinefjellet Fm	Dalkjegla Mb	832.0	-8.40	-5.54	Fine sandstone to siltstone	Tube	Around 3.2 (diameter) x 6.3	
FA73-1	Festningen	Carolinefjellet Fm	Dalkjegla Mb	829.0	-12.32	-4.91	Fine sandstone	Tube	Around 3.5 (diameter) x 4.5	
FA73-2	Festningen	Carolinefjellet Fm	Dalkjegla Mb	829.0	-5.82	-15.09	Fine sandstone	Tube	Around 3.5 (diameter) x 4.5	
FA75B-1	Festningen	Carolinefjellet Fm	Dalkjegla Mb	812.5	-18.25	-4.27	Fine sandstone	Tube	Around 1.9 (diameter) x 2.7	
FA75B-2	Festningen	Carolinefjellet Fm	Dalkjegla Mb	812.5	-15.78/ -15.4	-4.84/ -4.79	Fine sandstone	Tube	Around 1.9 (diameter) x 2.7	
FA77	Festningen	Carolinefjellet Fm	Dalkjegla Mb	803.0	-6.9	-9.7	Medium to coarse sandstone	Sediment	Around 5.5 x 7.0	Bioturbation
FA84	Festningen	Carolinefjellet Fm	Innkjegla Mb	875.0?	-4.73	-19.90	Conglomerate	Broken pieces	-	Contains glendonite pieces
FA89-1	Festningen	Carolinefjellet Fm	Dalkjegla Mb	767.0	-9.71	-18.60	Fine sandstone	Conglomerate	Around 1.5 x 2.9 x 5.0	
FA89-2	Festningen	Carolinefjellet Fm	Dalkjegla Mb	767.0	-9.39	-16.71	Fine sandstone	Conglomerate	Around 1.5 x 2.9 x 5.0	
FA97	Festningen	Carolinefjellet Fm	Dalkjegla Mb	740.0	-18.49	-10.01	Silstone	Pyrite concretion	Around 1.5 x 1.6 to 1.3 x 2.3	
FV8BIS	Festningen	Rurikfjellet Fm	Kikutodden Mb	610.0	-	-	Siltstone	Carbonate concretion	-	
FV14	Festningen	Rurikfjellet Fm	Kikutodden Mb	600.5	-25.24	-	Siltstone	Sediment	-	
FV15	Festningen	Rurikfjellet Fm	Kikutodden Mb	598.5	0.53/ 0.55	-0.33/ 0.29	Siltstone	Belemnite	Around 2.8 (diameter)	
FV23	Festningen	Rurikfjellet Fm	Kikutodden Mb	563.0	-25.33	-	Siltstone	Sediment	-	
FV23D	Festningen	Rurikfjellet Fm	Kikutodden Mb	563.0	-	-	Siltstone	Sediment	-	
FV24	Festningen	Rurikfjellet Fm	Kikutodden Mb	559.0	-25.46	-	Siltstone	Sediment	-	
FV25C	Festningen	Rurikfjellet Fm	Kikutodden Mb	556.0	1.73/ 2.1	-1.51/ -1.66	Siltstone	Belemnite	-	

FV26	Festningen	Rurikfjellet Fm	Kikutodden Mb	554.5	-25.54	-	Siltstone	Sediment	-
FV26A	Festningen	Rurikfjellet Fm	Kikutodden Mb	554.0	0.24/ 0.02	-0.99/ -1.34	Siltstone	Belemnite	-
FV27	Festningen	Rurikfjellet Fm	Kikutodden Mb	543.0	-	-	Siltstone	Carbonate concretion	-
FV32	Festningen	Rurikfjellet Fm	Kikutodden Mb	533.0	-0.06/ -0.01	-1.37/ -0.71	Siltstone	Belemnite	Around 1.8 (diameter)
FV34	Festningen	Rurikfjellet Fm	Wimanfjellet Mb	528.5	0.09/ 0.29	-0.19/ 0.35	Siltstone	Belemnite	Around 1.4 (diameter)
FV34B	Festningen	Rurikfjellet Fm	Kikutodden Mb	528.0	-	-	Siltstone	Carbonate concretion	-
FV34S	Festningen	Rurikfjellet Fm	Wimanfjellet Mb	528.0	-	-	Siltstone	Sediment	-
FV46B	Festningen	Rurikfjellet Fm	Wimanfjellet Mb	474.0	-24.55	-	Siltstone	Sediment	-
FV47E	Festningen	Rurikfjellet Fm	Wimanfjellet Mb	462.5	-26.25	-	Siltstone	Sediment	-
Grut7A	Grumantbyen	Carolinefjellet Fm	Dalkjegla Mb?	33.0	-29.20	-3.71	Siltstone	Canonball concretion	Around 6.1 (diameter)
GRUT cgmt-a,b,c	Grumantbyen	Carolinefjellet Fm	Dalkjegla Mb?	14.0?	-6.71	-14.71	Siltstone	Conglomerate	Around 9.1 x 10.0 x 12.7
Grut26	Grumantbyen	Carolinefjellet Fm	Dalkjegla Mb?	8.0	-5.89	-11.08	Siltstone	Cone in cone	Around 4.4 x 4.5 x 11.3
Grut26B	Grumantbyen	Carolinefjellet Fm	Dalkjegla Mb?	8.0	-5.89	-11.08	Siltstone	Cone in cone	Around 4.4 x 4.5 x 11.3

C. Microscopic observations

1. Prevalent carbonate phases

Sample ID	Shape	Size	Color	%	Shape	Size	Color	%	Shape	Size	Color	%
	Ros (and *Rov*) phase				*Bot* phase				*Cc* phase			
FeAA1-1	Rosette-like, sub-rounded, lath-shaped; internally zoned	Around 97 µm (diameter) to 278 x 375 µm	Transparent/grey to light yellowish brown	55	Fibrous to bladed (generally isopachous) > surrounding Ros	Around 6-24 µm thick	Dark brown	5	Equant spar?	-	Transparent	±30
FeAA1-2	Rosette-like, sub-rounded, lath-shaped; internally zoned	Around 83 µm (diameter) to 208 x 458 µm	Transparent/grey, but mostly overprinted by a light yellowish brown to dark brown	45-55	Fibrous to bladed (isopachous?) > surrounds Type 1 and difficult to see (dissolution?)	Around 8-12 µm thick	Dark brown to black	5	Sparite	Around 61 µm (diameter) to 71 x 122 µm?	Transparent to grey (smaller crystals)	30
FeAA1-3	Mostly sub-rounded to lath-shaped, but also rosette-like; internal zonation; areas with overabundance of organic impurities	Around 29 µm (diameter) to 265 x 1176 µm	Transparent/grey to light brown with golden brown or pinkish tint	35	Fibrous anisopachous with preferential growth on narrow plane	Around 7-28 µm thick	Dark brown to black	5?	Equant spar	Around 212 µm (diameter)?	Transparent with light brown tint	40-60
FeAA1-4	Sub-rounded to occasionally rosette-like and lath-shaped; internally zoned	Around 44 µm (diameter) to 397 x 441 µm; average 103 x 162 µm	Transparent/grey to light yellowish brown and dark golden brown	55	Fibrous to acicular (anisopachous)	Around 8-25 µm thick	Dark brown to mostly black	5?	Equant spar	On average around 88 x 147 µm?	Transparent to grey	30-35
FeAA2	Sub-rounded to rectangular/lath-shaped and rosette-like	Around 44 µm (diameter) to 485 x 662 µm; average 206 µm (diameter)	Transparent/grey to light yellowish brown	45	Fibrous to bladed with preferential growth on narrow plane	Around 6-31 µm thick	Dark brown to black	5?	Equant spar	-	Transparent to grey	20-30
FeAA2-2	Sub-rounded to lath-shaped; sometimes internally zoned; variability in organic impurities; distinction Ros and Rov difficult to interpret	Around 20 x 40 µm to 125 x 250 µm; average 75 µm (diameter)	Transparent/grey to mostly light amber yellow/brown in PPL; dark to bright green in UV	30	Fibrous anisopachous to isopachous overgrowths surrounding Ros; preferential growth on the narrow side of lath-shaped Ros	Around 2-25 µm thick	Dark brown in PPL; bright light green in UV	10	Dirty anhedral calcite spar	-	Transparent/grey to light brown in PPL; amber brown to green and dark in UV	45
FeAA5	Mostly rosette, also sub-rounded or lath-shaped; generally good distinction between Ros and Rov (dark with shades of green); organic impurities	Around 15 µm (diameter) to 75 x 250 µm; average 60 µm (diameter)	Transparent/grey and light amber yellow to amber yellow	30	Typically fibrous botryoidal overgrowths with internal zonation both anisopachous and isopachous	Around 5-70 µm thick	Amber yellow to brown	20	Dirty anhedral calcite spar and microcrystalline	-	Transparent/grey in PPL; amber brown to green/dark in UV	40
FeAA9	Original structure not well-defined; mostly sub-rounded to oval; very rich in organic impurities	Around 20 µm (diameter) to 110 x 200 µm? (diameter)	Mostly light amber yellow to brown in PPL; bright green to dark in UV	35	Fibrous/granular overgrowths that are anisopachous and lack internal zonation	Around 5-50? µm thick	Dark brown	35	Dirty anhedral calcite spar	-	Transparent/brownish in PPL; granular brown and dark in UV	10
FA91-1	Sub-rounded to rosette-like; original shape not clear/well-defined; organic impurities	Around 20 x 35 µm to 60 µm (diameter)?	Predominately light amber brown/yellow in PPL; green to mostly dark in UV	10	Very thin or nonexistent overgrowths on Ros with an acicular/fibrous to granular fabric; distinction Ros-II not very clear	Around 0-30 µm thick	Light brown in PPL; bright green in UV	5	Dirty anhedral calcite (microcrystalline?); spotty/granular fabric	Overgrowths: 0-80 µm (anisopachous)	Transparent/grey in PPL; dark with yellow/brown spots in UV	15
FA91-2	Sub-rounded to oval and lath-shaped; original shape not clear; organic impurities; internal zonation rare	Around 15 µm (diameter) to 100 x 175 µm	Transparent/grey to mostly light amber yellow and dark brown in PPL; brown/green to mainly dark in UV	10	Very thin or nonexistent overgrowths on Ros with an acicular/fibrous to granular fabric	Around 0-50 µm thick	Amber yellow to brown in PPL; pale to bright green in UV	5	Dirty anhedral calcite with a granular and occasionally microcrystalline fabric	-	Transparent/grey in PPL; brown/green to dark in UV	25
FA91A	Irregular to mostly sub-rounded; spotty/granular fabric; lack of internal zonation; shape/structure both clearly visible and almost nonexistent; distinction Ros and Rov not clear/present	Around 40 µm (diameter) to 175 x 250 µm	Transparent/grey to mostly amber yellow/brown	30	Anisopachous overgrowths with an increasingly acicular/fibrous fabric; some organic impurities (especially in outer rim)	Around 5-100 µm thick	Light amber brown to dark brown	20	Anhedral calcite spar with lots of fractures	-	Transparent/grey in PPL; brown to dark in UV	40
FA91A-2	Sub-rounded to oval shape; variable organic impurity content; distinction Ros and Rov not clear/present	Around 30 µm (diameter) to 300 µm (diameter)	Light to dark amber brown with some transparent spots in PPL; brown to dark in UV	20	Almost absent anisopachous overgrowths with an acicular/fibrous fabric	Around 0-40 µm thick	Brown in PPL; pale or bright green in UV	<5	Anhedral calcite spar with lots of fractures	-	Transparent/grey in PPL; brown to dark in UV	25
FA91B	Sub-rounded to oval shape; organic impurities; distinction Ros-Rov and Bot not very clear; occasionally internally zoned, but mostly a spotty fabric	Around 25 µm (diameter) to 100 x 220 µm	Transparent to mostly light amber yellow and dark brown in PPL; brown/green to mostly dark in UV	25	Messy irregular overgrowth with no clear structure or an acicular/fibrous fabric		?	Transparent/brown in PPL; bright green under UV	<5	Anhedral calcite to occasionally microcrystalline	-	Transparent to light amber yellow in PPL; brown to green and dark in UV	40
FA92-1	Sub-rounded to oval shape; original shape not clear; organic impurities; no real distinction between Ros and Rov	Around 50 µm (diameter) to 240 x 430 µm	Light amber yellow to brown with some transparent spots in PPL; green/brown to dark in UV	15	Anisopachous overgrowths with a fibrous or granular fabric	Around 0-25 µm thick	Light to dark brown with some transparent/grey spots in PPL; bright and pale green in UV	5	Anhedral to microcrystalline calcite	-	Transparent/grey in PPL; green and brown in UV	20

Sample	Ros/original structure	Size	Colour (PPL/UV)	%	Overgrowth (Rov/Bot)	Thickness	Overgrowth colour	%	Calcite	Calcite size	Calcite colour	%
FA92-2	Original structure not clear; mostly sub-rounded; organic impurities	Around 40 µm (diameter) to 90 x 120 µm	Light amber yellow to dark brown in PPL; dark in UV	15	Anisopachous overgrowths with a fibrous or granular fabric	Around 0-25 µm thick	Transparent to light amber yellow and brown; pale and bright green in UV	20	Anhedral calcite spar	-	Transparent/grey to light brown	40
FA92-3	Original structure generally not clear; mostly sub-rounded and lath-shaped, but sometimes also rosette-like; organic impurities (very abundant in some cases); no clear internal zonation and distinction between Ros-Rov	Around 20 µm (diameter) to 400 µm (diameter)	Light amber yellow to dark brown with some transparent spots in PPL; brownish/green to mainly dark in UV	20	Anisopachous overgrowths with a fibrous or granular fabric	Around 0-50 µm thick	Transparent/grey to light amber yellow and dark rusty brown	10	Anhedral to microcrystalline calcite	-	Transparent/grey to light amber yellow in PPL; brown and bright green in UV	45
FA92-4	Sub-rounded to oval or lath-like shape; original structure quite messy; lots of organic impurities; sometimes distinction between Ros and Rov?	Around 25 µm (diameter) to 125-150 µm	Amber yellow to brown in PPL; brown to dark in UV	15	Anisopachous overgrowths with a fibrous or granular fabric	Around 0-50 µm thick	Transparent/grey to light amber yellow and dark rusty brown	15	Anhedral to microcrystalline calcite with a granular dirty fabric	-	Transparent/grey to pale amber yellow	30
FA93	Sub-rounded/oval, but most of the time not clear; organic impurities; rarely internally zoned	Around 60 µm (diameter) to 260 µm (diameter)	Transparent/grey to light amber yellow and brown	20	Almost absent anisopachous overgrowths with an acicular/fibrous fabric	Around 0-10 µm thick	Light amber yellow to brown in PPL; bright green in UV	<5	Anhedral calcite spar to microcrystalline calcite	-	Transparent/grey in PPL; brown/green to dark in UV	35
FA93-2	Original structure/shape very hard to see (mostly only clusters of organic impurities remain; sub-rounded and lath-shaped; no internal zonation	Around 25 µm (diameter) to 270 x 350 µm (diameter)	Light yellow amber to grey/brown in PPL; dark/brown in UV	25	Thin anisopachous overgrowths with a granular to fibrous fabric and occasionally with zonations	Around 0-60 µm thick	Light amber yellow to brown in PPL; bright green in UV	15	Anhedral calcite to microcrystalline	-	Transparent/grey in PPL; brown/green to dark in UV	30
FeVH2	Sub-rounded to oval and slightly rosette-like shape; shape less clear and less distinct organic impurities; less internal zonation; tendency to form clusters; surrounded by irregular/spotty overgrowths (Rov?)	Around 25 µm (diameter) to 75 µm (diameter); average 170 µm (diameter)	Transparent/grey to light amber yellow in PPL; dark in UV	5	Botryoidal overgrowths with a fibrous fabric and very distinct zonation; forms around Ros and anhedral yellow calcite	Approximately 5-25 µm thick	Transparent/grey to light amber yellow and dark rusty brown	80	-	-	-	-
FV23	Sub-rounded to lath-shaped and occasionally rosette-like; typically not internally zoned; organic impurities; forms zonations with lots of OM outside of the center or are these the dark brown zonations of Bot?	Around 30 µm (diameter) to 80 x 300 µm; average 80 µm (diameter)	Transparent/grey to mostly dark amber yellow in PPL; dark with some brown tints in UV	15	Zonated overgrowths to irregular and messy botryoids within center well-defined zonations without any clear fabric towards the outside	Around 5-50 µm thickness (zonations); size irregular botryoids unclear	Transparent/grey and light amber yellow to predominately dark amber yellow in PPL; bright green to dark under UV	75	Anhedral; only present within the center and slightly outside the center	Not clear	Transparent/grey in PPL; dark green to dark in Uv	10
FV24A	Sub-rounded to rosette and lath; sometimes internally zoned; organic impurities; Ros cuts into later Bot zonation; botryoidal overgrowth of Rov (difficult to distinguish from Bot), light amber color	Around 30 µm (diameter) to 100 µm (diameter); average 45 x 64 µm	Transparent/grey and pinkish to light amber yellow/brown in PPL; dark and bright green in UV	10	Botryoidal overgrowths with a fibrous/acicular fabric and distinct zonations, including a dark brown rim with abundant organic impurities; followed by a more anhedral botryoidal fabric	Zonations: around 5-25 µm thick	Transparent/light amber yellow to predominately dark amber yellow/brown	85	Anhedral	Minimal occurrence (only within the center)	Transparent/grey	<5
FV24B	Sub-rounded to rosette; internally zoned; organic impurities; forms start of new macrozonation on top of Bot?	Around 25 µm (diameter) to 115 x 140 µm; average 50 µm (diameter)	Light amber yellow with transparent spots in PPL; brown to mostly black in UV	5-10	Botryoidal overgrowths with an acicular to fibrous fabric and distinct zonation; outer zones in each macrozonation are least defined/more anhedral; interspaced by anhedral yellow calcite; dark brown zonations contain organic impurities	Approximately 5-20 µm thick	Light to dark amber yellow and dark brown in certain zonations	80	Anhedral	Minimal occurrence (only within the center)	Transparent/grey	<5
FV25D	Sub-rounded to lath and sometimes rosette-like; organic impurities less abundant; Rov clearly defined around Ros (transparent)	Around 25 µm (diameter) to 60 x 130 µm	Transparent/grey to light amber yellow	5	Botryoidal overgrowths with an anhedral to acicular/spotty fabric and zonations; interspaced by anhedral yellow calcite	Approximately 10-100 µm thick	Transparent and light amber yellow to mostly dark amber yellow/brown and brown in PPL; bright green to dark in UV	85	Anhedral	Minimal occurrence (only within the center)	Transparent/grey in PPL; dark with brown spots in UV	<5
FV25E	Sub-rounded to lath-shaped; organic impurities difficult to recognize	Around 50 µm (diameter) to 70 x 200µm	Transparent/grey to light amber yellow/brown in PPL; dark to amber brown in UV	5	Botryoidal overgrowths initially thin zonations, later phases more anhedral/spotty; dark amber brown phases with clear fibrous fabric	Initially 5-20 µm thick	Transparent/grey and light amber yellow to dark amber brown	80	Anhedral with some slightly larger than microcrystalline crystals	Small crystals: around 5 µm	Transparent/grey in PPL; dark with brown spots in UV	10

Sample	Description	Size	Color (PPL/UV)	%	Overgrowth	Thickness	Overgrowth color	%	Crystal	Occurrence	Color	%
FV26	Sub-rounded to lath and rosette shaped; organic impurities; weak internal zonation; present both in the center as well as close to rim	Around 40 µm (diameter) to 120 x 240 µm	Transparent/grey to light amber yellow in PPL; dark in UV with some light spots	10	Botryoidal overgrowths with both very distinct and less well-defined zonations	Approximately 10-100 µm thick	Mostly transparent and light amber yellow to amber brown	80	Anhedral	Mainly found in the center and zonations	Transparent/grey in PPL; dark in UV	1 0
FV26A	Sub-rounded to lath-shaped; typically internally zoned or spotty; contains some organic impurities, but not much; mostly an isopachous Rov	Around 25 µm (diameter) to 65 x 150µm	Mostly transparent/grey to light amber yellow in PPL; dark and spotty/greenish in UV	5	Botryoidal overgrowths with some clear zonations and a fibrous to acicular fabric around Ros and within the macrozonations, overall much more anhedral than other samples	Around 3-25 µm thick (clear zonations)	Transparent/grey and light amber yellow to mostly amber yellow/brown	75	Anhedral and microcrystalline (next to each other)	Minimal occurrence (only within the center)	Transparent/grey in PPL; brown/green to dark in UV	5
FV47B	Only well-defined in the center; mostly sub-rounded to lath-shaped, occasionally rosette-like; some organic impurities	Around 20 µm (diameter) to 95 x 100 µm	Mostly light amber yellow to transparent	5?	Botryoidal overgrowths that are either messy/spotty or show clear zonations with a fibrous fabric	Around 5-70 µm thick (clear zonations) > individual zonations typically isopachous	Transparent/light amber yellow to amber brown in PPL; bright green to brown and dark in UV	80	Anhedral	Minimal occurrence (only within the center)	Transparent/grey in PPL; green in UV	-
GRUT16	Sub-rounded/lath-shaped to rosette-like; internal zonation	Around 50 µm (diameter) to 190 x 350 µm; average 170 µm (diameter)	Mostly transparent/grey with pinkish tint and light amber brown	10	Irregular/spotty overgrowths that could also be Rov	Approximately 0-60 µm thick	Transparent in PPL; dark amber brown in UV	<5	Anhedral dirty calcite	-	Transparent/grey and pinkish in PPL; gold to brown in UV	10
GRUT16-1	Sub-rounded/rosette to lath shaped; internal zonation (only visible in UV); organic impurities; distinction Ros and Rov not clear	Around 15 µm (diameter) to 165 x 250 µm; average 75 µm (diameter)	Transparent/grey and light brown to amber yellow	35	Signs of fibrous spotty fabric, but overall not clear; anisopachous	Around 0-25 µm thick	Transparent and light brown	15	-	-	-	-
GRUT18	Sub-rounded to rosette; internally zoned: organic impurities; distinction Ros and Rov with Bot not always clear, intertwined	Around 35 µm (diameter) to 125 µm (diameter); average 65 µm (diameter)	Light amber yellow to light brown in PPL; dark with brownish spots in UV	50	Signs of a fibrous fabric in the rim of 1st layer and botryoidal in 2nd layer (only clearly visible in UV)	Around 25-55 µm thick	Light brown and amber to transparent/grey color in PPL; bright green to pale greenish yellow in UV	45	Anhedral?	Not clear; in PPL not distinction between Bot and III	Transparent/grey and pinkish in PPL; dark green to dark in UV	5
GRUT20B	Sub-rounded/oval to sometimes lath and rosette-like; internally zoned; organic impurities; no distinction between Ros and Rov	Around 20 µm (diameter) to 230 x 400 µm; average 120 x 190 µm	Transparent/grey to light amber yellow in PPL; dark with brown greenish clots/spots in UV	25	Thin and generally isopachous overgrowths with signs of a fibrous or acicular fabric	Around 10-40 µm thick	Yellowish amber and transparent/grey in PPL; bright green in UV; no dark brown rim	10	Very fine equant spar/microcrystalline; no distinct structure	Not clear	Transparent/grey	15
GRUT21	Sub-rounded to lathy and rosette-like; internally zoned; organic impurities	Around 30 µm (diameter) to 120 µm (diameter); average 75 µm (diameter)	Transparent/grey to light brown in Ros and rusty border at the end of Rov; amber brown and dark green to mostly black in UV	40	No clear shape at the start to fibrous/acicular at the rim; overall shape botryoidal (radial structure missing)	Around 10-75 µm thick	Transparent to light brown in PPL (rim = dark brown); bright to dark green and brown in UV	50	Equant spar	Not clear	Transparent/grey in PPL; yellow to light green and dark in UV	10
GRUT27	Mostly sub-rounded and lath-shaped; sometimes internally zoned; Ros and Rov difficult to distinguish; organic impurities	Around 15 µm (diameter) 150 x 200 µm; average 100 µm (diameter)	Transparent/grey to mostly light amber brown	40	No distinct/clear shape, fibrous/acicular rim is missing	Approximately 25-35 µm thick	Transparent /grey (no brown) in PPL; bright green in UV	50	Sparite	Not clear; no distinction between Bot-III	Transparent/grey in PPL; dark to bluish green in UV	5

2. Additional observations

Sample ID	Border	Recrystallization	Dissolution	Pyrite	Dolomite/clay	Comments	Sediment
FeAA1-1	-	No phase, only late diagenetic twinning overprinting Ros, Bot, and Cc	At Rim 3	Abundant within BotI (10 %)	-	-	
FeAA1-2	-	Rim zonation around 385-538 μm thick and golden mustardy color	-	Abundant within BotI (10 %); patchier/less euhedral than FeAA1-1	-	Rim 1 (zonation); rim 2 broken up into small pieces	-
FeAA1-3	-	Late diagenetic overprint Ros, Bot, and Cc (center 3)	-	Present, but not abundant	-	-	-
FeAA1-4	-	Rim zonation around 147-441 μm thick and golden mustardy color	-	Occasionally within BotI (10%); not euhedral	-	Border zonation	-
FeAA2	-	-	-	Abundant within BotI (20%); subhedral to euhedral	-	Veins through thin section	-
FeAA2-2	Pretty well-defined borders with some minor signs of dissolution	Abundant late diagenetic overprint with twinning spanning over different phases; deposition anhedral calcite at rim	Signs of small dissolution events in sediment and around rim	Euhedral and very abundant in BotI (15%)	-	Border zonation (light amber yellow to dark brown) > anhedral calcite	Fine micritic mud with OM and some quartz grains (average 20 μm in diameter)
FeAA5	Rough borders consisting mostly of anhedral brown calcite	Some late diagenetic overprint with twinning	Fluid veins throughout sample (Center 2 - 10x)	Predominately within sediment, but also some in Ros-Bot (center 3)	-		Dark micritic mud with OM, pyrite and some quartz grains (average 20 μm in diameter)
FeAA9	Both well-defined and rough borders with signs of dissolution	Deposition of anhedral calcite within center and especially around rim (20%); late diagenetic overprint with twinning (rim 1)	-	Small traces in BotI and in sediment?	-	Contains lots of cracks	Dark micritic mud with OM, pyrite and subrounded/spherical quartz grains (average 25 μm in diameter)
FA91-1	Pretty well-defined borders (anhedral calcite) with some indication of dissolution events)	Deposition of anhedral enclosing calcite that occupies former margin ikaite crystal (70%); late diagenetic overprint with twinning	Some signs of dissolution in sediment and around rim (rim 2)	Only within sediment	-	Contains lots of cracks	Fine micritic mud with OM, pyrite and fine quartz grains (average 10 μm in diameter)
FA91-2	Rough well-defined borders with signs of dissolution	Deposition of anhedral calcite (60%) in center and former margin ikaite; late diagenetic overprint with twinning	Dissolution at rim	Within sediment and potentially BotI	Quartz grains within glendonite	Contains lots of cracks	Fine micritic mud with OM, pyrite and fine quartz grains (average 20 μm in diameter)
FA91A	No rim, but areas within the glendonite with sediment and a rough/messy border that seems to have been dissolved	Deposition of anhedral calcite (10%) with a distinct brown amber color that lacks growth relationships with Ros, Bot, and Cc	-	Negligible traces of pyrite within sample	-	No border zonation; contains lots of cracks	Very fine micritic mud with lots of OM and no sign of quarts grains
FA91A-2	Well-defined border at the original ikaite borders and rough broken up and dissolved border within the glendonite	Deposition of anhedral calcite (45%) with yellow to brown amber color, does not follow growth structures Ros, Bot, and Cc	Dissolution in the form of inclusions?	Within sediment and as traces within glendonite?	-	Contains lots of cracks	Fine micritic mud with OM and quartz grains (average 20 μm in diameter)
FA91B	Typically more defined borders at the rim and rough ones towards to center of the glendonite	Deposition of anhedral calcite (30%) occupying ikaite rims, but also present in center; strong late diagenetic overprint with twinning	Dissolution event at rim	Within sediment and in small amounts within sample; anhedral	-	Contains lots of cracks	Muddy quartz sand (average grain-size: 40 μm) and micritic mud in between pyramid points
FA92-1	Well-defined rims	Deposition of anhedral calcite (60%) throughout sample; late diagenetic overprint with twinning	Dissolution event and fluid inclusion at rim	Present within sediment and BotI	-	Contains lots of cracks	Fine muddy sand (average grain-size: 10 μm) with OM/pyrite and micritic mud in between pyramid points; draping around pyramid points
FA92-2	Well-defined rough rims	Deposition of anhedral calcite (25%) mainly at original ikaite rims; late diagenetic overprint with twinning	Small and large dissolution events	Within sediment and BotI in glendonite	-	Contains lots of cracks	Muddy quartz sand (average grain-size: 40 μm) with OM
FA92-3	Generally well-defined rims with some dissolution	Deposition of anhedral yellow calcite (25%) at ikaite rims and within center; clear late diagenetic overprint with twinning	Dissolution events at rim and pore space within sample	Within sediment as well as Type I/BotI	-	Contains lots of cracks	Draping around glendonite; fine muddy sand (average grain-size: 10 μm) with OM/pyrite and micritic mud in between pyramid points
FA92-4	Both well-defined and rough dissolved rims	Deposition of anhedral yellow calcite (40%) at ikaite rims and within center; late diagenetic overprint with twinning	Dissolution event at rim	Within sediment as well as Ros, Bot, and Cc	-	Contains lots of cracks	Draping around glendonite; dark micritic mud with OM, pyrite and subrounded/spherical quartz grains (average 10 μm in diameter)
FA93	Well-defined and rough dissolved border	Deposition of anhedral calcite (35%) occupying mainly ikaite rims, but also occur internally; late diagenetic overprint with twinning	-	Euhedral pyrite within center (large and small)	-	-	-
FA93-2	Both distinct rough borders and dissolved border	Deposition of anhedral calcite (30%) occupying ikaite rims, but also present in center; strong late diagenetic overprint with twinning	At rims/borders?	Loose pyrite and patches within sediment and within center of sample (BotI)	-	Contains lots of cracks	Muddy quartz sand (average grain-size: 30 μm) and micritic mud in between pyramid points

FeVH2	Rough borders that seems to be dissolved with some distinct planes	Anhedral amber and light-yellow calcite (15%) around Ros-Bot (most pronounced as anisopachous and irregular zonations around Bot	At rims/borders?; dissolution events/fluid veins	-	-	Contains lots of cracks	Very fine micritc mud with some pyrite and quartz grains (20 μm (diameter) to 100 x 200 μm; average: 40 μm (diameter))
FV23	Both clear plane and rough with broken pieces within sediment	Small occurrence of yellow anhedral calcite at transition center and outer zonations	Fluid veins throughout sample	Small amounts within zonations	-	Contains lots of cracks	Sandy micritic mud with abundant quartz grains (average: 40 μm (diameter))
FV24A	Rough border with signs of dissolution	Late diagenetic overprint, but no clear structures	Dissolution events around rim	Small anhedral pyrite in Bot (center 1)	-	Contains lots of cracks	Dark micritic mud with OM and quartz grains (average 50 μm in diameter) and pyrite
FV24B	Clear planes and rough borders with signs of dissolution	Deposition of anhedral yellow calcite (5%) in between Bot; Late diagenetic overprint	Dissolution events around rim?	Small anhedral pyrite in Bot (center)	-	Contains lots of cracks	Micritic mud with pyrite and ample OM with quartz grains (average 50 μm in diameter)
FV25D	Rough but with distinct lines and signs of dissolution	Deposition of anhedral yellow calcite (10%) in between Bot	-	Euhedral pyrite within center	Mud/sediment within center glendonite	Contains lots of cracks	Micritic mud with pyrite and ample OM, large amounts of quartz grains (average 50 μm in diameter)
FV25E	Rough, but with mostly clear planes that show signs of dissolution	Deposition of anhedral brown calcite (5%) in between Bot at the macrozonations and the rim	-	Abundant within sediment and to a very small degree in Bot (small anhedral crystals)	Mud/sediment within parts of the sample	Contains lots of cracks	Brown micritic sand (sub-rounded to rounded quartz grains: average 80-90 μm) with OM and abundant pyrite
FV26	Overall quite distinct borders with some indication of dissolution	Deposition of anhedral yellow calcite only around rims	-	Small anhedral crystals abundant within Bot	-	Contains lots of cracks	Brown micritic sand (sub-rounded and medium sphericity quartz grains: average 50 μm) with OM and abundant pyrite
FV26A	Ragged/rough and broken up with some clear rims; signs of dissolution	Depositional of anhedral yellow calcite (20%) at the end of each macrozonation	-	Not abundant, but present within Bot-III	Mud/sediment within center and incorporated at rims	Contains lots of cracks	Brown micritic sand (sub-rounded/spherical with quartz grains: 50 μm), abudant pyrite and OM
FV47B	Rough edges with lots of dissolution	Lots of microcrystalline calcite crystals; anhedral messy dark brown phase (similar to GRUT20B/GRUT16) in between zonations	-	Small amounts within Bot in center (anhedral)	Microcrystalline calcite or mud/sediment within center?	Contains lots of cracks	Not Clear
GRUT16	Both rough distinct planes and broken areas	Deposition of anhedral amber and light-yellow calcite (75%) with lots of dark brown ragged areas; late diagenetic overprint with twinning	-	Small amounts within Ros-Bot and anhedral calcite	-	Contains lots of cracks	Dark micritic mud with OM and quartz grains (average 50 μm in diameter)
GRUT16-1	Mostly rough and broken up; some distinct planes	Deposition of anhedral amber calcite (50%)	-	Small amounts within Ros-Bot	Mud/sediment within glendonite?	Contains lots of cracks	Mostly micritic mud with OM, pyrite and some quartz grains (40 μm)
GRUT18	Mostly rough and broken up; loose pieces of glendonite within sediment	Signs of late diagenetic overprint and twinning that crosses different phases	-	Within sediment and around broken borders glendonite; occasionally within glendonite	Mud/sediment within small holes of glendonite	Contains cracks	Mostly micritic mud with OM, pyrite and some quartz grains (40 μm)
GRUT20B	Both distinct/rough	Deposition of anhedral light yellow mustardy calcite (50%)	-	Within sediment?	Mud/sediment within sample	Contains lots of cracks	Mostly micritic mud with OM, pyrite and some quartz grains (30 μm)
GRUT21	Both distinct/flat and ragged/irregular	Late diagenetic overprint (all phases)	Dissolution events around glendonite (rim 1)	No	-	Contains cracks	Mostly micritic mud with OM, pyrite and some quartz grains (30 μm)
GRUT27	Mostly broken up with fragments within sediment	No clear distinction between Ros-Bot (equant spar recrystallization?); twinning through different phases	-	Only within sediment?	Mud/sediment within sample	Contains medium cracks	Mostly micritic mud with OM and maybe some pyrite